

NUMERICAL MODELING OF FLUID FLOW AND SOLIDIFICATION PHENOMENA
DURING ULTRASONIC PROCESSING OF METAL-MATRIX-NANOCOMPOSITES

by

DAOJIE ZHANG

LAURENTIU NASTAC, COMMITTEE CHAIR

MARK L. WEAVER
LAYACHI HADJI
PAUL G. ALLISON
CHARLES A. MONROE

A DISSERTATION

Submitted in partial fulfillment of the requirements
for the degree of Doctor of Philosophy in the
Department of Metallurgical and Materials Engineering
in the Graduate School of
The University of Alabama

TUSCALOOSA, ALABAMA

2016

Copyright Daojie Zhang 2016
ALL RIGHTS RESERVED

ABSTRACT

In present study, 6061 and A356 based nano-composites are fabricated by using the ultrasonic stirring technology (UST) in a coreless induction furnace. SiC nanoparticles are used as the reinforcement. Nanoparticles are added into the molten metal and then dispersed by ultrasonic cavitation and acoustic streaming assisted by electromagnetic stirring.

The applied UST parameters in the current experiments are used to validate a recently developed magneto-hydro-dynamics (MHD) model, which is capable to model the cavitation and nanoparticle dispersion during UST processing. The MHD model accounts for turbulent fluid flow, heat transfer and solidification, and electromagnetic field, as well as the complex interaction between the nanoparticles and both the molten and solidified alloys by using ANSYS Maxwell and ANSYS Fluent. Molecular dynamics (MD) simulations are conducted to analyze the complex interactions between the nanoparticle and the liquid/solid interface.

The current modeling results demonstrate that a strong flow can disperse the nanoparticles relatively well during molten metal and solidification processes. Molecular dynamics simulation results prove that ultrafine particles ($\ll 1 \mu\text{m}$) will be engulfed by the solidification front instead of being pushed, which is beneficial for nano-dispersion.

Experimental results confirm that the nanoparticles are dispersed reasonably well in the metal matrix, but some insignificant agglomeration still occurs. Besides, SEM/EDS results show that C element tends to gather around the grain boundary area where the Si eutectic phase is located.

DEDICATION

This thesis is dedicated to everyone who helped me and guided me through the trials and tribulations of creating this manuscript. In particular, my family and close friends who stood by me throughout the time taken to complete this masterpiece.

LIST OF ABBREVIATIONS AND SYMBOLS

d_m	Grain size of the matrix
d_p	Particle size
v_p	Volume fraction of the particles
α	Constant value in Zener formula
$\Delta\sigma_l$	Increment in yield strength due to load transfer
σ_m	Yield strength of the unreinforced matrix
F_{Lor}	Lorentz force
μ	Magnetic permeability
σ	Ohmic conductivity
H	Magnetic field intensity
J	Current density
B	Magnetic flux density
t	Time
a_q	Volume fraction of phase q
ρ_q	Density of phase q
\mathbf{u}_q	Velocity of phase q
μ_q	Molecular viscosity of phase q
\dot{m}_{pq}	Mass transfer from phase p to q
\dot{m}_{qp}	Mass transfer from phase q to p

\mathbf{f}_{DPM}	Momentum exchange
\mathbf{f}_{other}	Other forces including virtual mass force, lift force, etc.
h	Sensitive enthalpy
h_{ref}	Reference enthalpy at reference temperature
T_{ref}	Reference temperature
c_p	Specific heat
ρ	Density of the melting aluminum
k	Thermal conductivity of the melting aluminum
\mathbf{u}	Velocity of the fluid
Q_L	Momentum source term
L	Latent heat
f_s	Solid fraction
f_l	Liquid fraction
\mathbf{S}	Momentum sink due to reduced porosity in the mushy zone
ε	Small number to prevent division by zero
A_{mush}	Mushy zone constant
\mathbf{u}_p	Particle velocity
\mathbf{F}_D	Drag force
ρ_p	Density of the particle
Re	Relative Reynolds number
C_D	Drag coefficient
\mathbf{F}_B	Buoyancy force
\mathbf{F}_G	Gravitational force

\mathbf{g}	Gravitational acceleration
\mathbf{F}_{lift}	Saffman's lift force
$\bar{\bar{\tau}}_s$	Stress-strain tensor of the granular phase
$\bar{\mathbf{u}}$	Mean fluid velocity
ζ	Normally distributed random number
k_e	Turbulent kinetic energy
\mathbf{a}	Accelerations due to other forces except drag force
\mathbf{x}_p	Particle position
r_c	Cut-off distance
E_{tot}	EAM potential
r_{ij}	Atomic separation distance between atoms i and j
$V(r_{ij})$	Pair potential
F	Embedding energy
$\bar{\rho}_i$	Density induced on atom i by all other atoms in the system
$\rho(r_{ij})$	Atomic density function
V_{ij}	Tersoff potential
r_{ij}	Length of the ij bond
f_R	Repulsive component of the Tersoff potential
f_A	Attractive component of the Tersoff potential
f_C	Potential associated with the cut-off function
V	Morse interatomic potential
r_0	Equilibrium bond distance
D_0	Well depth of the Morse potential

α_m	Width of the Morse potential
<i>CSP</i>	Centro-symmetry parameter
<i>N</i>	Number of nearest neighbors
Φ	Diameter of the nanoparticle
MMCs	Metal matrix composites
UST	Ultrasonic stirring technology
PEP	Particle engulfment and pushing
MD	Molecular dynamics
CFD	Computational fluid dynamics
MHD	Magneto-hydro-dynamics
DDPM	Dense discrete phase model
EAM	Embedded atom model
EM	Elastic modulus
GNDs	Geometrically necessary dislocations
EMS	Electromagnetic stirring
UDF	User defined function
SEM	Scanning electron microscope
EDS	Energy-dispersive X-ray spectroscopy

ACKNOWLEDGMENTS

First and foremost, I would like to express my sincere gratitude to all those people who have made this dissertation possible and because of whom my graduate experience has been one that I will cherish forever.

I am most indebted to my advisor Dr. Laurentiu Nastac, committee chair of this dissertation, for his patience, enthusiasm, immense knowledge, and excellent guidance and caring, making my Ph.D. experience productive and stimulating.

I would also like to thank all my committee members, Dr. Mark Weaver, Dr. Layachi Hadji, Dr. Paul Allison and Dr. Charles Monroe for their continuous encouragement and insightful comments. I am deeply grateful to them for holding me to a high research standard and walking me through various difficulties.

In addition, I would like to thank my colleagues Shian Jia and Yang Xuan for their assistance with the experimental work. I am also thankful to my colleague Qing Cao for her help and support during the modeling and simulation work. I am especially grateful for this group which has been a source of friendships as well as good advice and collaboration.

Most importantly, I would like to thank my family for their love, patience, and encouraging and supporting me in all my pursuits.

CONTENTS

ABSTRACT.....	ii
DEDICATION.....	iii
LIST OF ABBREVIATIONS AND SYMBOLS.....	iv
ACKNOWLEDGMENTS.....	viii
LIST OF TABLES.....	xii
LIST OF FIGURES.....	xiii
CHAPTER 1 – INTRODUCTION.....	1
CHAPTER 2 – LITERATURE REVIEW.....	6
2.1 Aluminum Alloys 6061 and A356.....	6
2.2 Ultrasonic Stirring Technology.....	6
2.3 Metal-Matrix-Nano-Composites.....	7
2.3.1 Hall-Petch Strengthening Mechanism.....	8
2.3.2 Orowan Strengthening Mechanism.....	8
2.3.3 Load-bearing Effect.....	9
2.3.4 Enhanced Dislocation Density Strengthening.....	9
2.4 Induction Stirring.....	9
2.5 Particle Engulfment and Pushing Models.....	11

2.6 Molecular Dynamics Simulation	12
2.6.1 Pairwise Potentials	12
2.6.2 Molecular Dynamics Simulation of Solidification	14
CHAPTER 3 – MATHEMATICAL MODELS	16
3.1 Ultrasonic Cavitation	16
3.2 Electromagnetic Field	18
3.3 CFD Model	19
3.3.1 Fluid Flow Model	20
3.3.2 Solidification Model	21
3.3.3 Particle Tracking Model	22
3.4 Molecular Dynamics Model	25
3.4.1 EAM Potential for Aluminum	26
3.4.2 Tersoff Many-body Potential for Silicon Carbide	27
3.4.3 Potential for Describing the Interface	27
3.5 Solution Procedure.....	29
CHAPTER 4 – SIMULATION RESULTS AND DISCUSSION	30
4.1 Results without EMS and PEP.....	30
4.2 Results with PEP Model Only	37
4.3 Results with EMS only	41
4.4 Results with both EMS and PEP Model	45

4.5 Molecular Dynamics Simulation Results.....	53
CHAPTER 5 – EXPERIMENTAL VALIDATION.....	64
5.1 Experimental Approach	64
5.2 Microscopy Analysis of 6061-based with 1.0 wt.% SiC samples	66
5.3 Microscopy Analysis of A356-based Nanocomposites Treated during Solidification.....	68
CHAPTER 6 – CONCLUSIONS AND FUTURE WORK.....	73
6.1 Conclusions.....	73
6.2 Main Contributions of This Study	75
6.3 Recommendations for Future Work.....	76
REFERENCES	78
APPENDIX I – TERSOFF POTENTIAL VALUES FOR SiC.....	88

LIST OF TABLES

Table 2.1 Nominal chemical composition of matrix alloys studied (in wt.%)	6
Table 3.1 Morse potential function parameters parameterized to the ab initio data obtained	28
Table 4.1 Standard deviations of overall particle distribution with strong flow and weak flow ..	53

LIST OF FIGURES

Figure 1.1 Schematic of particle liquid/solid interface interactions	2
Figure 1.2 Schematic of experimental setup.....	3
Figure 2.1 Schematic diagram of crystallization systems.....	15
Figure 3.1 Components of the Mathematical Models.....	16
Figure 3.2 Ultrasonic cavitation simulation results	17
Figure 3.3 Velocity inlet profile.....	18
Figure 3.4 Simplified 2D geometry model of a coreless induction furnace	19
Figure 3.5 CFD geometry model	20
Figure 3.6 MD geometry model.....	26
Figure 3.7 Schematic of the simulation procedure	29
Figure 4.1 Fluid flow and particle distributions after 1.0s and 3.0s	31
Figure 4.2 Particle distributions after 1.0s and 3.0s with a different injection location	32
Figure 4.3 Fluid flow after 1.0s and 3.0s with the ultrasonic probe placed at the bottom of the furnace (gravity direction upward)	33
Figure 4.4 Particle distributions after 1.0s and 3.0s with the ultrasonic probe placed at the bottom of the furnace (gravity direction upward)	34
Figure 4.5 Fluid flow after 1.0s and 20.0s with a weaker flow	35
Figure 4.6 Particle distributions after 20.0s with two different injection positions and a weaker flow (gravity direction downward)	36
Figure 4.7 Fluid flow after 10.0s and 30.0s (gravity direction downward).....	37
Figure 4.8 Particle distributions after 10.0s and 30.0s (gravity direction downward).....	38
Figure 4.9 Fluid flow after 10.0s and 20.0s (gravity direction upward).....	39

Figure 4.10 Particle distributions after 10.0s and 20.0s (gravity direction downward).....	39
Figure 4.11 Fluid flow after 30.0s and 50.0s with a weaker flow (gravaty direction downward)	40
Figure 4.12 Particle distributions after 30.0s and 50.0s with a weaker flow	41
Figure 4.13 Electromagnetic force distribution and fluid flow field without ultrasonic stirring..	42
Figure 4.14 Fluid flow and particle distributions after 1.0s and 3.0s with EMS	43
Figure 4.15 Fluid flow after 1.0s and 20.0s with a weaker flow and EMS	44
Figure 4.16 Particle distributions after 1.0s and 20.0s with a weaker flow and EMS (gravity direction downward)	45
Figure 4.17 Fluid flow and particle distributions after 10.0s and 30.0s with EMS	46
Figure 4.18 Particle distribution along vertical direction after 3s, 10s, and 30s.....	48
Figure 4.19 Particle distribution along radial direction after 3s, 10s, and 30s	48
Figure 4.20 Overall particle distribution after 30s.....	49
Figure 4.21 Fluid flow after 30.0s and 50.0s with EMS (gravity direction downward).....	50
Figure 4.22 Particle distributions after 30.0s and 50.0s with EMS (gravity direction downward)	51
Figure 4.23 Particle distribution along vertical direction after 20s, 30s, and 50s.....	52
Figure 4.24 Particle distribution along radial direction after 20s, 30s, and 50s	52
Figure 4.25 Overall particle distribution after 50s with a weaker flow	53
Figure 4.26 Centro-symmetry parameters for Al in the system.....	55
Figure 4.27 Calculation of equilibrium melting temperature	55
Figure 4.28 Evolution of potential energies of the system at different temperatures	57
Figure 4.29 Evolution of potential energies of the system without SiC particle at different temperatures	57
Figure 4.30 Solid/liquid status of the system after 10 ps and 40 ps.....	58
Figure 4.31 Solid/liquid status of the system after 100 ps, 200 ps, 300 ps, 400 ps, 500 ps, and 600 ps.....	60

Figure 4.32 Position of SiC nanoparticle during solidification	61
Figure 4.33 Solid/liquid status of the system with a $\Phi 20$ nm SiC nanoparticle.....	63
Figure 4.34 Position of a $\Phi 20$ nm SiC nanoparticle during solidification	63
Figure 5.1 UST equipments	65
Figure 5.2 SEM and EDS analysis of the 6061-based 1.0 wt.% SiC nanocomposites.....	68
Figure 5.3 Microstructures of non-UST and UST+SiC treated A356 samples	69
Figure 5.4 SEM results at X50 magnification for UST+1% SiC treated A356 samples	70
Figure 5.5 EDS mapping results at different magnifications for UST+1% SiC treated samples .	72

CHAPTER 1 – INTRODUCTION

Aluminum-based metal matrix composites (MMCs) have been extensively studied and widely used in the aerospace, automotive and military industries due to their high strength-to-weight ratios and enhanced mechanical and thermal properties including specific modulus, superior strength, stiffness, good wear resistance, fatigue resistance and improved thermal stability [1-4]. However, the particles commonly used are micron-sized which has a counterpart that the ductility of the MMCs deteriorates with high ceramic particle concentration [5]. Consequently, more attention has been drawn to metal matrix nanocomposites (MMNCs), since the properties of metallic alloys reinforced by ceramic nanoparticles (with dimensions less than 100 nm) would be enhanced considerably while the ductility of the matrix is retained [6-12]. However, it is extremely difficult to obtain uniform dispersion of nano-sized ceramic particles in liquid metals due to high viscosity, poor wettability in the metal matrix, and a large surface-to-volume ratio, which results in agglomeration and clustering [5]. Currently, several fabrication technologies including high-energy ball milling [9, 12], in-situ synthesis [8], electroplating [13], and ultrasonic technology (UST) [4-6, 14-16] are most commonly used, among which UST is supposed to be more reliable and cost effective.

Induction heating, which is a clean, energy-efficient and well-controllable melting process, is widely applied in metallurgical industry. During the process, the dominant electromagnetic field will produce temperature field and fluid flow. Meanwhile, all these fields may strongly influence one another, which significantly complicates the situation [17]. An improved understanding of the heat and electromagnetically driven flow mainly requires

mathematical modeling, as experimental research is very limited due to the physical and chemical properties of the melts [18].

During the solidification process, the particles will either be pushed or engulfed by the solidification front, among which particle pushing will always lead to segregation even clustering of the particulate reinforcement, which is undesirable as it results in non-homogeneous response and lower macroscopic mechanical properties [19]. It is clear that particle pushing and engulfment (PEP) is a complicated phenomenon and is affected by many factors [20], e.g., particle size and shape, interfacial energy between particle, liquid and solid, temperature gradient in the melt ahead of the solidification interface etc. Figure 1.1 shows the schematic of particle liquid/solid interface interactions [21].

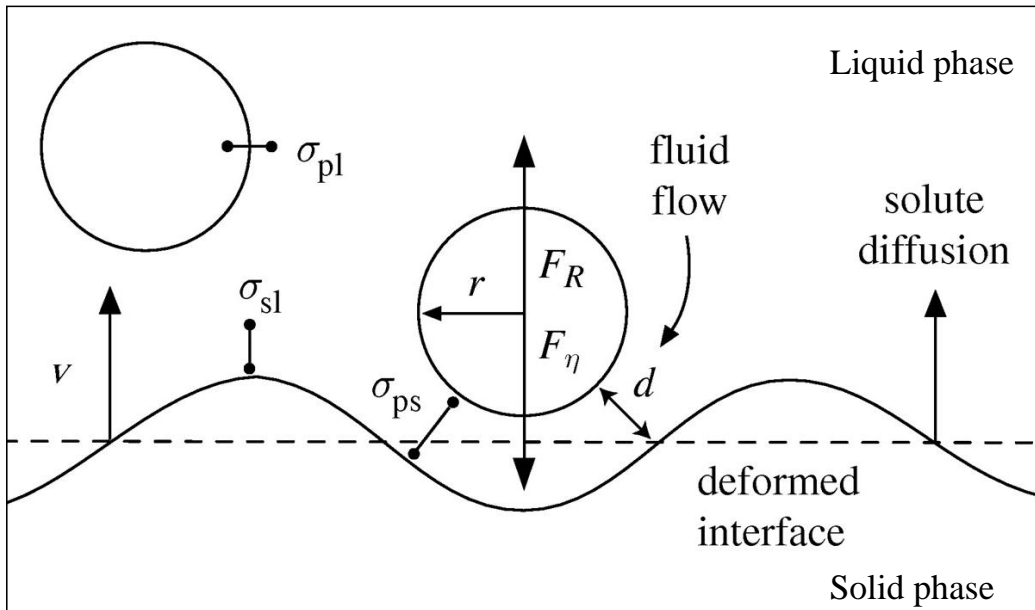


Figure 1.1 Schematic of particle liquid/solid interface interactions [21]

However, it is extremely expensive and difficult, perhaps impossible, to investigate the interfacial properties experimentally at the atomic level. Thus, molecular dynamics (MD)

simulations (atomistic simulations) conducted at the atomic level offer a good alternative in studying the interface mechanics. The open source MD program LAMMPS (Large-scale Atomic/Molecular Massively Parallel Simulator) [22] is used to conduct MD simulations to analyze the complex interactions between the nanoparticle and the liquid/solid interface.

In present study, 6061 and A356 nano-composites are fabricated by using the ultrasonic stirring technology (UST) in a coreless induction furnace. SiC nanoparticles are used as the reinforcement. Nanoparticles are added into the molten metal and then dispersed by ultrasonic cavitation and acoustic streaming assisted by electromagnetic stirring. Schematic of experimental setup is shown in Figure 1.2.

The applied UST parameters in the current experiments are used to validate a recently developed multiphase computational fluid dynamics (CFD) model [23], which is capable to model the cavitation and nanoparticle dispersion during UST processing. The CFD model accounts for turbulent fluid flow, heat transfer and solidification, and electromagnetic field, as well as the complex interaction between the nanoparticles and both the molten and solidified alloys by using ANSYS Maxwell and ANSYS Fluent.

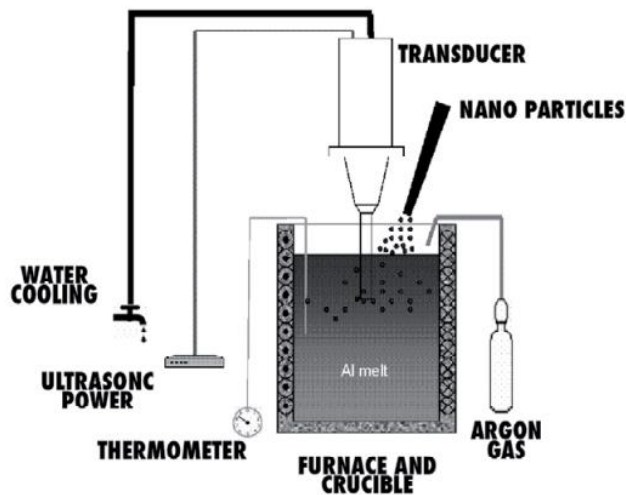


Figure 1.2 Schematic of experimental setup [24]

Experimental results of microstructure, mechanical behavior and mechanical properties of the cast nano-composites have been investigated. The current experimental results show that the nanoparticles are dispersed reasonably well in the metal matrix, but some insignificant agglomeration still occurs. Besides, SEM/EDS results show that C element tends to gather around the grain boundary area where the Si eutectic phase is located.

The current modeling results demonstrate that a strong flow can disperse the nanoparticles relatively well. Also, it is proved that the injection position will not affect the final distribution of the SiC nanoparticles as long as the flow is strong enough to disperse the particles, otherwise, the injection position will have a significant effect on the distribution of the particles. Besides, it is determined that the gravity direction can play a major role on the nano-dispersion during the solidification process. When the gravity direction is upward with respect with the location of the ultrasonic probe, the solidification time is decreased and thus well dispersed nano-composites can be produced faster than in the case when the gravity direction is reversed. In addition, it is demonstrated that induction stirring can help improve the fluid flow characteristics, making the nanoparticle distribution even more uniform. Moreover, molecular dynamics simulation results validate the theory of Ferguson [25, 26] that ultrafine particles ($\ll 1 \mu\text{m}$) will be engulfed by the solidification front instead of being pushed, which is beneficial for nano-dispersion.

The purpose of this study is to research the main five topics shown below:

- 1) One of the main objectives is to build a comprehensive mathematical model to obtain an understanding and insight of the ultrasonic stirring technology and induction stirring processing applied to the fabrication of metal-matrix-nanocomposites (MMNCs). Turbulent fluid flow enhanced by the ultrasonic stirring and electromagnetic force field

along with the dispersion of nanoparticles during ultrasonic cavitation, induction stirring, and solidification processes is investigated.

- 2) A magneto-hydro-dynamics (MHD) model available in ANSYS Maxwell and ANSYS Fluent is adapted to develop a more sophisticated analysis of fluid flow phenomena in an induction furnace in the presence of ultrasonic cavitation and acoustic streaming.
- 3) Dense Discrete Phase multiphase Model (DDPM), which accounts for the viscous drag force, buoyancy force, gravitational force, virtual mass force, Saffman's lift force and interfacial force, is adapted to predict the trajectories of the nanoparticles. A PEP model is developed to deal with nanoparticles approaching the liquid/solid interface.
- 4) A 3D molecular dynamics model using hybrid potentials (EAM, Tersoff, and Morse potentials) is applied to describe the complex interactions between a SiC nanoparticle and the liquid/solid interface.
- 5) The effects of UST on dispersion of reinforcement nanoparticles and improving of the wettability of nanoparticles during molten metal processing and solidification are investigated experimentally to validate the numerical model.

CHAPTER 2 – LITERATURE REVIEW

2.1 Aluminum Alloys 6061 and A356

Aluminum alloys 6061 and A356 are selected as the metal matrix because they are readily castable and widely studied. 6061 alloy is commonly used in following components: aircraft fittings, marine fittings and hardware, electrical fittings and connectors, automotive parts, such as wheel spacers etc. Typically A356 alloy is used in castings for aircraft parts, pump housings, impellers, high velocity blowers and structural castings where high strength is required.

The chemical compositions of the 6061 and A356 alloys are shown in Table 2.1.

Table 2.1 Nominal chemical composition of matrix alloys studied (in wt.%)

Alloy	Si	Fe	Cu	Mn	Mg	Zn	Ti	Balance
6061	0.4-0.8	0.70	0.15-0.4	0.15	0.8-1.2	0.25	0.20	Al
A356	6.5-7.5	0.20	0.20	0.10	0.25-0.45	0.10	0.20	Al

2.2 Ultrasonic Stirring Technology

Mechanical stirring [27] has become an established method of incorporating larger solid ceramic particles into metal melts because it is simple, flexible and applicable to large-quantity production. However, it is extremely difficult for this method to distribute and disperse fine particles (considered to be $<20 \mu\text{m}$) uniformly in metal melts due to their large surface-to-volume ratio and low wettability, which induces agglomeration and clustering [28]. Besides,

when the stirring stops, the particles tend to return to the surface and most of them still stuck to each other as clusters/agglomerates. This could be caused by the nanoparticles being surrounded by surface gas layers.

Meanwhile, ultrasonic stirring technology has been extensively used in purifying, degassing, and refinement of metallic melt [29-34], mainly because introducing the ultrasonic energy into a liquid will induce nonlinear effects such as cavitation and acoustic streaming [33, 35-53]. Ultrasonic cavitation can create small-size transient domains that could reach very high temperatures (5000 K) and pressures (1000 atm) as well as extremely high heating and cooling rates above 10^{10} K/s [54]. The strong impact coupling with local high temperatures can potentially break the nanoparticle clusters and clean the particle surface [24]. These pressure and temperature fluctuations are also likely to induce heterogeneous nucleation in the melt [29]. Besides, they will promote dendrite fragmentation by enhancing solute diffusion through acoustic streaming as well [55-59]. Compared to mechanical stirring, the transient cavitation induced by ultrasonic stirring could remove the gas layer from the surface of the nanoparticles, thus improving the wettability between the nanoparticles and matrix significantly [28].

2.3 Metal-Matrix-Nano-Composites

To overcome the limitations of low ultimate tensile strength and ductility due to particle fracture and particle/matrix interfacial failure [60, 61], nano-sized reinforcements are studied. The outstanding mechanical performance of MMNCs is the result of several strengthening mechanism contributions, namely: Hall-Petch strengthening, Orowan strengthening, load-bearing effect, and enhanced dislocation density strengthening (Taylor relationship) [62-65].

2.3.1 Hall-Petch Strengthening Mechanism

Hall-Petch strengthening, which is a well-known strengthening mechanism, explains the relationship between the strength of the material and the grain size: as the grain size decreases, the strength increases. For nanocomposites, the grain size of the matrix depends on the particle size and volume fraction of the particles since the particles can interact with grain boundaries acting as pinning points, retarding or stopping the grain growth. The relationship between the grain size of the matrix d_m , particle size d_p , and volume fraction of the particles v_p can be represented by the Zener formula [63]:

$$d_m = \frac{4\alpha d_p}{3v_p} \quad (2-1)$$

where α is a proportional constant.

2.3.2 Orowan Strengthening Mechanism

The Orowan mechanism consists in the interaction of nanoparticles with dislocations. It is widely acknowledged, however, that Orowan strengthening is not significant in the MMCs, because the reinforcement particles are coarse and the interparticle spacing is large. In contrast, due to the presence of highly-dispersed nanosized reinforcement particles (smaller than ~100 nm) in a metal matrix, Orowan strengthening becomes more favorable in MMNCs [62]. For composites containing fine particles, strengthening is often explained by the Orowan mechanism.

2.3.3 Load-bearing Effect

The load transfer from the soft and compliant matrix to the stiff and hard particles under an applied external load contributes to the strengthening of the base material. For the equiaxed particulates, an increment in yield strength due to load transfer is expressed by [63]:

$$\Delta\sigma_l = 0.5v_p \sigma_m \quad (2-2)$$

where σ_m is the yield strength of the unreinforced matrix.

2.3.4 Enhanced Dislocation Density Strengthening

The Taylor relationship describes the relationship between the contribution of dislocation density and the strength of the material. Because of the thermal (the difference in the coefficient of thermal expansion) and the elastic modulus (EM) mismatch between the matrix and the reinforcement, which are in thermal equilibrium only at the temperature at which they are brought into contact during the process, plastic deformation are generated in the matrix, especially in the interface region, which will result in geometrically necessary dislocations (GNDs) during material cooling and straining [62, 63].

2.4 Induction Stirring

A lot of effort has been put into developing and improving the mathematical models of electromagnetic agitated turbulent flow in induction furnaces.

In 1975, Szekely and Nakanishi [66] presented a mathematical formulation describing fluid flow and tracer dispersion in an ASEA-SKF furnace. They were able to solve the turbulent Navier-Stokes equations together with a simplified form of Maxwell's equations. The computed results were reported to be in reasonable agreement with tracer dispersion measurements.

El-Kaddah *et al.* [67] compared the experimental measurements with theoretical predictions, which is based on the numerical solution of Maxwell's equations and the turbulent Navier-Stokes equations, in a 4-ton induction furnace. Good agreement was obtained both regarding the absolute values of the velocities and the mass transfer coefficients and the trends predicted by the theoretical analysis.

Kim and Yoon [68] were first to present a 3-dimensional model for induction stirring of an ASEA-SKF ladle equipped with a straight stirrer. The electromagnetic forces were solved by solving the partial differential equations for the magnetic flux [69]. Since then, Alexis *et al.* [70, 71] managed to improve this 3-dimensional model to account for more real stirring conditions e.g., heat transfer, slag and surface deformation etc.

More recently, Baake [72] and Jakovics [73] presented LES (Large-eddy simulation) modelling results of turbulent flow in an induction furnace. It was stated that traditional fluid flow models based on RANS (Reynolds Averaged Navier-Stokes) approach cannot predict the large scale periodic flow instabilities obtained from the experimental data. But LES requires much more resources for the generation and interpretation of the flow data than a RANS simulation, so Schwarze and Obermeier [18] proposed that unsteady RANS (URANS) models could yield a better resolution of the dynamics of the large flow structures and only need moderately more computer resources than a steady RANS simulation.

Poole and El-Kaddah [74, 75] presented a mathematical model for simulating electromagnetic, fluid flow, and heat transfer phenomena during solidification in an induction furnace. It demonstrated that for melt stirring using a stationary magnetic field, the flow consisted of two axisymmetric, recirculating loops, and was highly turbulent. Besides,

solidification would cause significant decay of the velocity by one order of magnitude in the suspended particle region.

2.5 Particle Engulfment and Pushing Models

A large number of PEP models were developed over the years. The first kinetic steady-state model was proposed by Uhlmann *et al.* [76]. In this model, the controlling transport mechanism in the particle-interface gap was assumed to be mass diffusion.

Chernov [77, 78] introduced the idea of a positive disjoining pressure in the liquid film separating the particle from the solidification interface which results in a repulsive interfacial force, while the viscous drag force is still the force responsible for particle engulfment. The presence of a positive disjoining pressure leads to particle repulsion while a negative pressure would lead to entrapment. The model considered smooth spherical particles and was further refined by considering the effect of the difference in the thermal conductivity between the particle and the melt to account for a non-planar interface [79].

Omenyi and Neumann [80] postulated that if the change in the interfacial energy for the system associated with particle engulfment is negative, engulfment is to be expected, otherwise pushing should result. This is valid for low growth velocities and when body forces are neglected.

Kinetic models developed by Stefanescu *et al.* [20, 81-83] considered the interfacial energy repulsive force responsible for pushing the particles away from the interface, and used the force balance on the particle to determine the status of the particle.

Hadji [84, 85] demonstrated that the presence of the particles modifies the solutal distribution coefficient, and the interaction of a particle with a directionally solidified interface

induces the onset of morphological instability provided that the particle-interface distance falls below a critical value.

In general, it is considered that whether particles are pushed or engulfed during solidification depends on the velocity of the particle relative to the solidification front according to previous models describing such particle engulfment and pushing phenomena. However, these models only predict the behavior in the coarse ($\gg 1 \mu\text{m}$) and fine particle ($\sim 1 \mu\text{m}$) systems, and they don't accurately describe the ultrafine particle ($\ll 1 \mu\text{m}$) system, presumably because the models rely on continuum mechanics. But these models cannot explain the evidence in MMNCs that nanoparticles can indeed be engulfed and distributed throughout the material and are not necessarily concentrated in grain boundary or interdendritic regions. As proposed by Ferguson [25, 26], for sufficiently small particles, Brownian Motion can partially or completely counteract forces such as viscous drag, gravity and thermal/concentration gradients, thus leading to engulfment rather than pushing.

2.6 Molecular Dynamics Simulation

Molecular dynamics was originally conceived within theoretical physics in the late 1950s [86], but is applied today mostly in materials science, chemical physics and the modeling of biomolecules.

2.6.1 Pairwise Potentials

In 1984, Daw and Baskes [87] developed the embedded atom method (EAM) based on density-functional theory, which describes interatomic potential as a function of a sum of functions of the separation between an atom and its neighbors. This model is particularly

appropriate for metallic systems and has been extensively used in the study of bulk properties of metals and alloys, surface relaxation and reconstruction features. Oluwajobi [88] employed three popular potentials (Lennar-Jones (LJ), Morse, and EAM) to model copper workpiece and diamond tool in nanometric machining, and concluded that the EAM potential was the most suitable of these three potentials, because it best describes the metallic bonding of the copper atoms. Yang [89] used the EAM potential for highly undercooled Ni₃Al alloy to get the melting point by means of the “sandwich” method and the NVE ensemble method, and get the specific heat by NPT ensemble method.

For the simulation of covalent solids, e.g., SiC or Si₃N₄, many-body potentials such as the Tersoff potential [90, 91] are available. Tersoff potential is based on the concept of bond order where the strength of a bond between two atoms is not constant, but depends on the local environment, i.e., to use the coordination of a bond as a variable for controlling the energy in a covalent bond. Simulation of brittle fracture of cubic SiC under hydrostatic pressure [92], surface reconstruction and thermal stability in cubic SiC [93], and rapid solidification of liquid SiC [94] has been reported.

Different potentials are used to deal with the Al/SiC interface. Zhao [95] employed the Chen-Mobius inversion method to get an analytical formula in which the potentials are expressed in terms of adhesive energies. Luo [96] used the Ito-Kohr-Das Sarma potential to calculate the atomic configuration and cohesive energy of various Al/SiC interfaces formed between low-index planes of Al and SiC surfaces. Dandekar [97] conducted MD simulations for describing Al-SiC interface mechanics, compared the results obtained by using LJ and Morse potentials [98] with ab initio data from Zhao [95], and drew the conclusion that Morse potential values parameterized from ab initio data were able to best represent the Al/SiC system.

2.6.2 Molecular Dynamics Simulation of Solidification

Various techniques have been developed attempting to obtain the thermodynamic properties of metal/alloy solidification, e.g., melting temperature, specific heat, latent heat, and solid-liquid interfacial free energy. These techniques could be grouped as: forced velocity simulations, free solidification simulations, and fluctuation analyses [99].

Broughton et al. [100, 101] were the first to employ free velocity atomistic simulations to the study of crystal growth rates. The system consists of three regions (see Figure 2.1 (a)): central dynamic zone, bottom quenched liquid, and top static crystal. Two heat baths are controlled at the same temperature below the melting point. The entire system moves at constant velocity along the z direction, and atoms which move beyond the top solid region are annihilated from the system and are replaced by liquid atoms in the lower region. Celestini and Debierre [102] also performed forced velocity MD simulations capable of extracting the velocity vs. undercooling behavior.

Hyot [99, 103], Daw [87, 104, 105], Briels [106] and Tymczak [107] used the free solidification method to study the crystallization kinetics in alloys, thermodynamic and structural properties of solid/liquid late transition metals, and velocity vs. undercooling behavior. The schematic diagram used by Hyot is shown in Figure 2.1. The technique will be explained in detail in section 3.4.

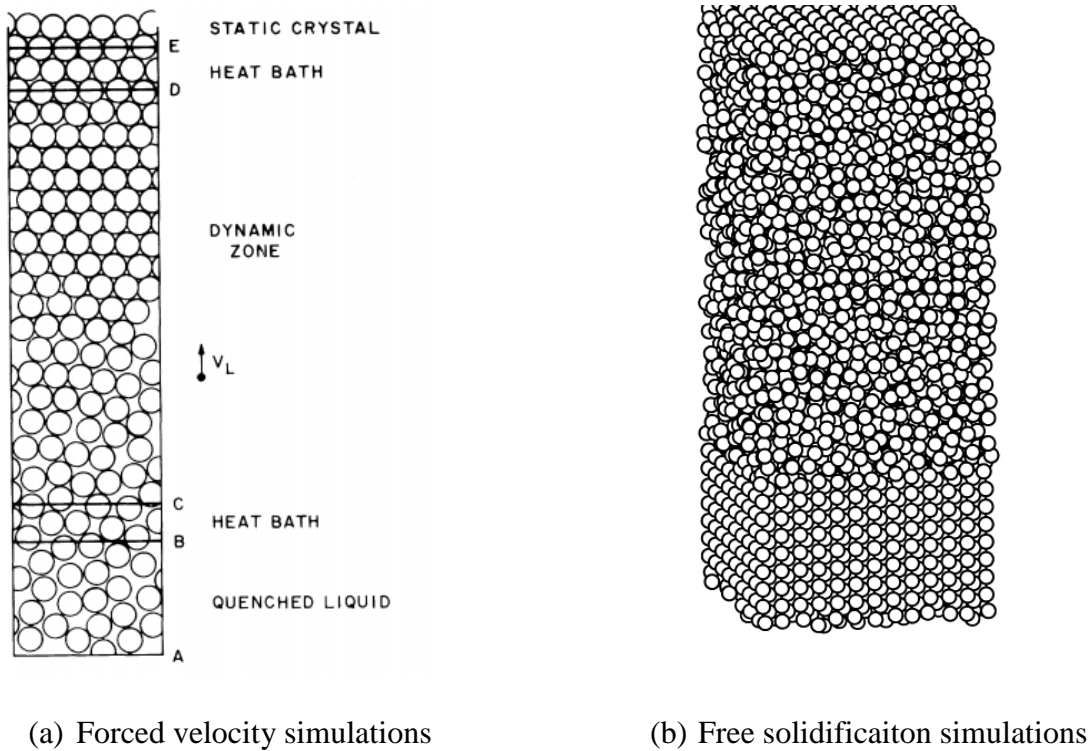


Figure 2.1 Schematic diagram of crystallization systems

In 1997, Briels and Tepper [106] developed an MD technique to calculate growth rate constants of various crystal faces from the fluctuations of interfaces during NVT simulations. For a solid-liquid LJ system maintained at the melting temperature, any fluctuation which moves the position of the solid-liquid interface, or equivalently changes the number of solid atoms, will lead to a change in pressure of the solid-liquid system due to the fixed-volume constraint and the density difference between the solid and liquid phases. Based on this theory and some relevant derivations, the solidification velocity vs. undercooling behavior can be established. However, this technique is conducted precisely at the melting temperature. It doesn't model the solidification process.

CHAPTER 3 – MATHEMATICAL MODELS

In present study, the mathematical models consist of 3 main parts: electromagnetic field, CFD model and molecular dynamics model. And the CFD model has 3 components: fluid flow model, solidification model, and particle tracking model as shown in Figure 3.1.

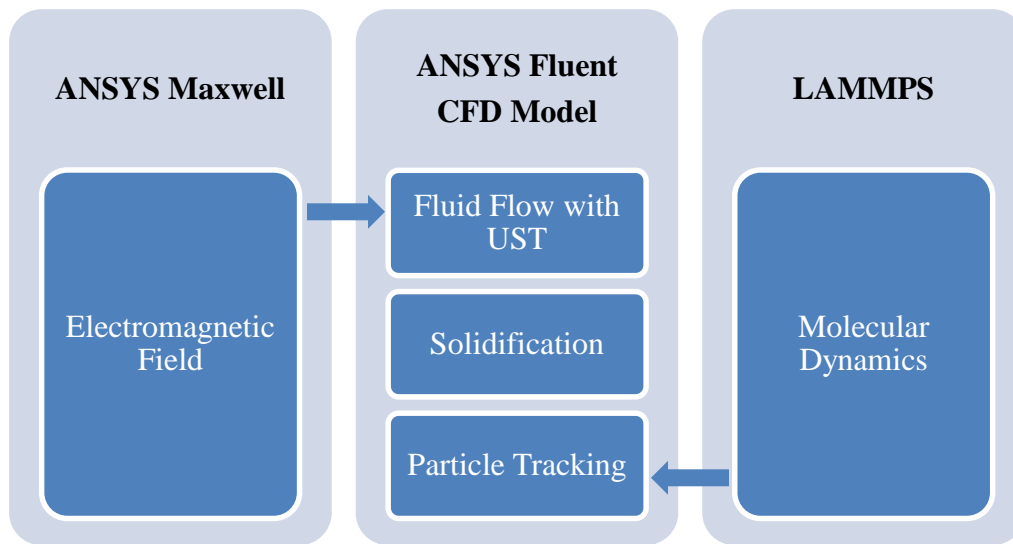


Figure 3.1 Components of the Mathematical Models

3.1 Ultrasonic Cavitation [23, 108]

The predictions of the ultrasonic cavitation and velocity vectors are presented in Figure 3.2 for an A356 liquid alloy at time $t = 2.0e-04$ s, which is after the onset of cavitation. Note that the onset of cavitation for this alloy system is around $8.8e-06$ s. The predicted ultrasonic cavitation region is presented in Figure 3.2(a), where the cavitation phase is hydrogen. The cavitation region is relatively small at time $t = 2e-04$ s, the acoustic streaming is relatively strong, especially in the ultrasonic probe region (see Figure 3.2(a) and (b)) and thus the newly

created/survived bubbles/nuclei can be transported into the bulk liquid quickly. Note that the legend in Figure 3.2(a) shows the volume cavitation region (volume fraction of cavities/bubbles/potential nuclei).

Figure 3.2(b) shows the profile for the velocity vectors. It can be seen that the velocity magnitude is significantly high beneath the ultrasonic probe.

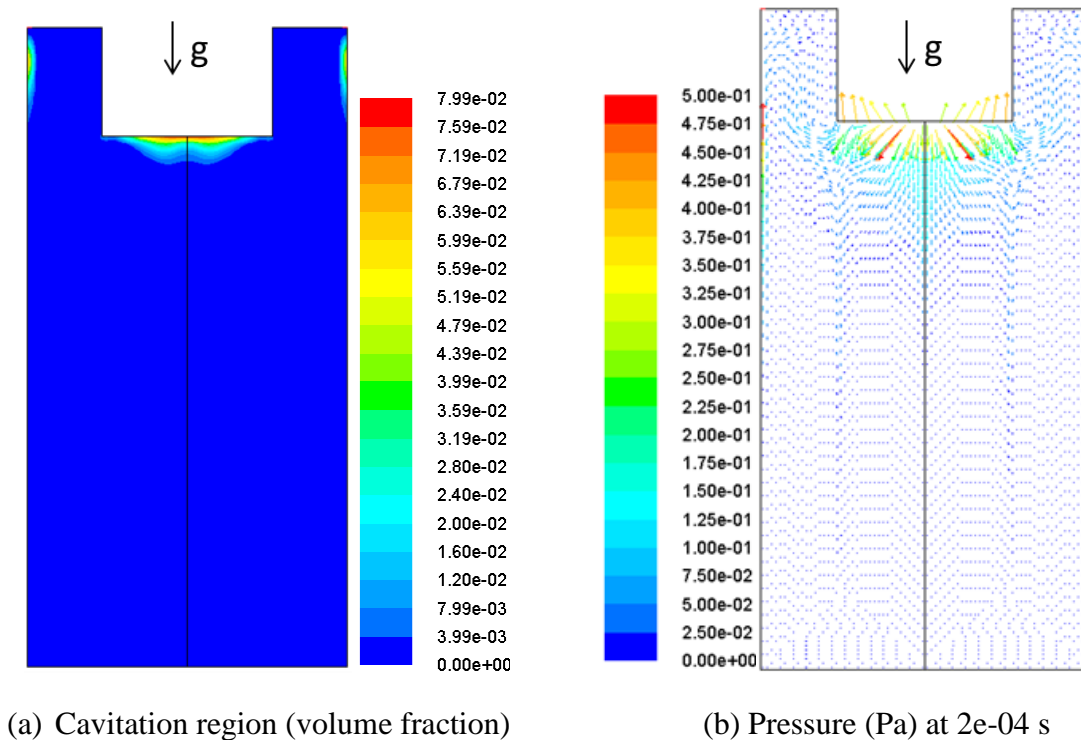


Figure 3.2 Ultrasonic cavitation simulation results [108]

Because modeling of ultrasonic cavitation takes place at a very small time scale (of the order of 10^{-5} to 10^{-7} s) and the fluid flow time scale is of the order of 10^{-2} to 10^{-3} s, the UST model is uncoupled from the CFD nano-dispersion model. In order to account for the effects of ultrasonic cavitation and acoustic streaming, the ultrasonic probe surface is set as velocity inlet,

and the velocity profile is defined in a user defined function (UDF), which is dependent on time as shown in Figure 3.3.

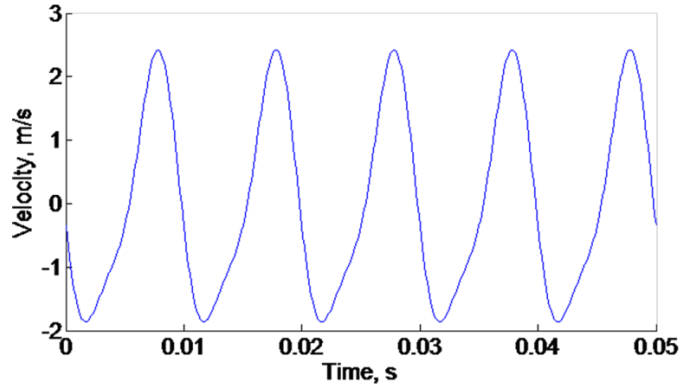


Figure 3.3 Velocity inlet profile

3.2 Electromagnetic Field

The geometry under investigation is simplified as 2-dimensional axisymmetric as shown in Figure 3.4. Due to harmonic nature of EM field and induced eddy currents, the Lorentz force \mathbf{F}_{Lor} can be decomposed into a steady and harmonic part that oscillates with double frequency. Because of much greater inertia times of melt in comparison to alternate EM field timescale, only the steady part of the Lorentz force is taken into account [109]. Assuming the fluid flow does not affect the electromagnetic field, the governing magneto-quasi-static equations for a material with constant magnetic permeability μ and constant Ohmic conductivity σ can be written as [110]

$$\nabla \times \mathbf{H} = \mathbf{J} \quad (3-1)$$

$$\nabla \times \mathbf{E} = -\frac{\partial \mathbf{B}}{\partial t} \quad (3-2)$$

$$\nabla \cdot \mathbf{B} = 0 \quad (3-3)$$

and the constitutive relations are

$$\mathbf{B}=\mu\mathbf{H} \quad (3-4)$$

$$\mathbf{J}=\sigma\mathbf{E} \quad (3-5)$$

Thus the Lorentz force is calculated as

$$\mathbf{F}_{Lor} = \mathbf{J} \times \mathbf{B} \quad (3-6)$$

where \mathbf{J} is current density, \mathbf{B} is magnetic flux density, \mathbf{E} is electric intensity, and \mathbf{H} is magnetic field intensity.

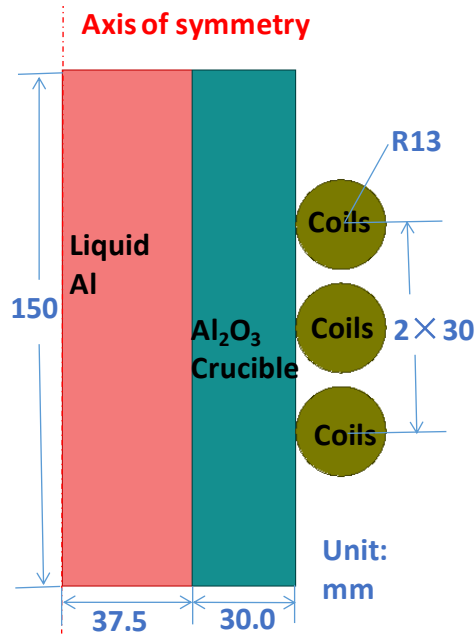


Figure 3.4 Simplified 2D geometry model of a coreless induction furnace

3.3 CFD Model

The schematic of CFD model is shown in Figure 3.5. The ultrasonic probe has a diameter of 40 mm. The liquid aluminium alloy is 6061. It has a density of 2685 kg/m³. The SiC nanoparticles with an average particle size of 55 nm and density of 3216 kg/m³ are treated as inert-particles. The mass flow rate of the SiC nanoparticles is 0.014 kg/s. Thus, 1.0 wt.% of SiC

nanoparticles can be injected at about 15 mm beneath the ultrasonic probe for 1.0 sec. The multiphase model accounts for turbulent fluid flow, heat transfer, and the complex interaction between the molten alloy and nanoparticles by using the ANSYS Fluent DDPM and $k-\omega$ turbulence model [111]. The CFD model is described in detail below.

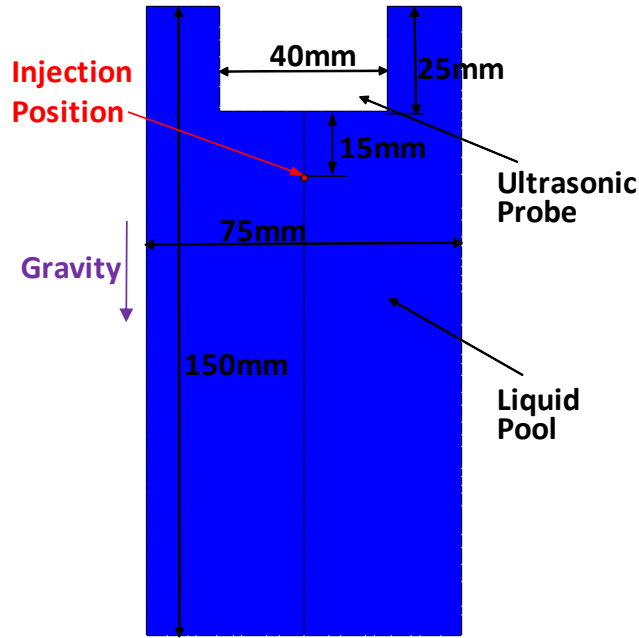


Figure 3.5 CFD geometry model

3.3.1 Fluid Flow Model

In the Eulerian DDPM multiphase model an Eulerian treatment is used for each phase, and the discrete phase (nanoparticles) is designated as a granular phase. The volume fraction of the particulate phase is accounted for in the conservation equations.

The continuity equation for the phase q is

$$\frac{\partial}{\partial t}(a_q \rho_q) + \nabla \cdot (a_q \rho_q \mathbf{u}_q) = \dot{m}_{pq} - \dot{m}_{qp} \quad (3-7)$$

The momentum balance for the phase q yields

$$\frac{\partial}{\partial t} (a_q \rho_q \mathbf{u}_q) + \nabla \cdot (a_q \rho_q \mathbf{u}_q \mathbf{u}_q) = -a_q \nabla P + \nabla \cdot [a_q \mu_q (\nabla \mathbf{u}_q + \nabla \mathbf{u}_q^T)] + a_q \rho_q \mathbf{g} + \mathbf{f}_{DPM} + \mathbf{f}_{other} \quad (3-8)$$

where a_q is the phasic volume fraction, ρ_q is the density, \mathbf{u}_q is the velocity, μ_q is the molecular viscosity, and P is the pressure shared by all phases. \dot{m}_{pq} characterizes the mass transfer from the p^{th} to q^{th} phase, and \dot{m}_{qp} characterizes the mass transfer from phase q to phase p . The momentum exchange term, \mathbf{f}_{DPM} , is considered only in the primary phase equations. The source term, \mathbf{f}_{other} , includes the virtual mass force, lift force, and turbulent dispersion force etc.

Equations (3-7) and (3-8) do not solve for the velocity field and volume fraction of the discrete phase. Their values are obtained from the Lagrangian tracking solution.

3.3.2 Solidification Model

The enthalpy method is used in the solidification model. The energy conservation equation of the enthalpy-formulation is [112]

$$\rho \frac{\partial h}{\partial T} + \rho \nabla \cdot (\mathbf{u}h) = \nabla \cdot (k \nabla T) + Q_L \quad \text{with} \quad h = h_{ref} + \int_{T_{ref}}^T c_p dT \quad (3-9)$$

where h is the sensitive enthalpy, h_{ref} is the reference enthalpy at the reference temperature T_{ref} ; c_p is specific heat; ρ and k are the density and thermal conductivity of the melting aluminium alloy, respectively, and \mathbf{u} is velocity of the fluid.

The source term Q_L concerning the latent heat in a single phase solidification model can be written as

$$Q_L = \rho L \frac{\partial f_s}{\partial T} \quad (3-10)$$

where L is the latent heat and f_s is the solid fraction, which is assumed to vary linearly with the temperature in the mushy zone.

The mushy region is treated as a porous medium, and the porosity in each cell is set equal to the liquid fraction f_l in that cell. The momentum sink due to the reduced porosity in the mushy zone is:

$$\mathbf{S} = \frac{f_s^2}{(f_l^3 + \varepsilon)} A_{mush} \mathbf{u} \quad (3-11)$$

where ε is a small number (0.001) to prevent division by zero; A_{mush} is the mushy zone constant, which measures the amplitude of the damping. The dynamic viscosity of the fluid also depends on the solid fraction which is related to temperature. It varies from 0.009 kg/(m·s) at the liquidus temperature to 1.0 kg/(m·s) below the coherency solid fraction (0.5).

3.3.3 Particle Tracking Model

The trajectory of a discrete phase particle is predicted by integrating the force balance on the particle. The force balance equates the particle inertia with the forces acting on the particle, and it is written as

$$\frac{d\mathbf{u}_p}{dt} = \mathbf{F}_D + \mathbf{F}_G + \mathbf{F}_B + \mathbf{F}_{virtual-mass} + \mathbf{F}_{pressure-gradient} + \mathbf{F}_{lift} + \mathbf{F}_{interaction} \quad (3-12)$$

where \mathbf{u}_p is the particle velocity, and all the terms at the right-hand are with a unit of force/unit particle mass.

The drag force, \mathbf{F}_D , exerted on the particle by the viscous liquid tends to make it follow the fluid flow, and is calculated by

$$\mathbf{F}_D = \frac{18\mu}{\rho_p d_p^2} \frac{C_D \text{Re}}{24} (\mathbf{u} - \mathbf{u}_p) \quad (3-13)$$

where \mathbf{u} is the fluid phase velocity, ρ_p is the density of the particle, and d_p is the particle diameter. Re is the relative Reynolds number, which is defined as

$$\text{Re} = \frac{\rho d_p |\mathbf{u} - \mathbf{u}_p|}{\mu} \quad (3-14)$$

where ρ is the fluid density.

C_D is the drag coefficient which is calculated by the model of Wen and Yu [113]:

$$C_D = \frac{24}{\text{Re}} (1 + 0.15 \text{Re}^{0.687}) \quad (3-15)$$

The net effect of the buoyancy force, \mathbf{F}_B , and the gravitational force, \mathbf{F}_G , is

$$\mathbf{F}_G + \mathbf{F}_B = \frac{\mathbf{g}(\rho_p - \rho)}{\rho_p} \quad (3-16)$$

The virtual mass force, $\mathbf{F}_{\text{virtual-mass}}$, is an unsteady force due to a change of the relative velocity of the particle submerged in the fluid, and can be calculated as

$$\mathbf{F}_{\text{virtual-mass}} = \frac{1}{2} \frac{\rho}{\rho_p} \frac{d}{dt} (\mathbf{u} - \mathbf{u}_p) \quad (3-17)$$

An additional force arises due to the pressure gradient in the fluid:

$$\mathbf{F}_{\text{pressure-gradient}} = \left(\frac{\rho}{\rho_p} \right) \mathbf{u}_p \nabla \mathbf{u} \quad (3-18)$$

The Saffman's lift force [114] due to shear is generated by the local velocity gradients across the particle, and is calculated as

$$\mathbf{F}_{lift} = \frac{2Kv^{1/2} \rho d_{ij}}{\rho_p d_p (d_{lk} d_{kl})^{1/4}} (\mathbf{u} - \mathbf{u}_p) \quad (3-19)$$

Where $K = 2.594$ and d_{ij} is the deformation tensor.

The term, $\mathbf{F}_{interaction}$, models the additional acceleration acting on a particle, resulting from interparticle interaction. It is computed from the stress tensor given by the Kinetic Theory of Granular Flows as

$$\mathbf{F}_{interaction} = -\frac{1}{\rho_p} \nabla \cdot \overline{\overline{\tau}_s} \quad (3-20)$$

where $\overline{\overline{\tau}_s}$ is the stress-strain tensor of the granular phase.

The chaotic effect of turbulence on the particle trajectories is accounted for using the stochastic tracking approach, i.e., the discrete random walk (DRW) model:

$$\mathbf{u} = \overline{\mathbf{u}} + \zeta \sqrt{2k_e / 3} \quad (3-21)$$

where $\overline{\mathbf{u}}$ is the mean fluid velocity in the trajectory equation (12), ζ is a normally distributed random number, and k_e is the local turbulent kinetic energy.

Equation (3-12) can be cast into the following general form:

$$\frac{d\mathbf{u}_p}{dt} = \frac{1}{\tau_p} (\mathbf{u} - \mathbf{u}_p) + \mathbf{a} \quad (3-22)$$

where the term \mathbf{a} includes accelerations due to other forces except drag force. Integrating the transport equation (23) for the path of each particle yields

$$\frac{d\mathbf{x}_p}{dt} = \mathbf{u} \quad (3-23)$$

where \mathbf{x}_p is the particle position.

3.4 Molecular Dynamics Model

A quarter of the MD geometry model is shown in Figure 3.6. The dimensions in the x, y, and z-direction are 40 nm \times 40 nm \times 40 nm. The diameter of the SiC nanoparticle is 10 nm. The simulated structure of pure aluminum is a face centered cubic (FCC) structure with a lattice parameter of 4.05 Å and with the $\langle 100 \rangle$ directions coincident with the Cartesian coordinates, since planes of looser packing, such as $\{100\}$, are better able to accommodate an atom that leaves the liquid to join the solid than a closer packed plane, such as $\{111\}$ [115]. The nanoparticle consists of a cubic crystalline polytype of silicon carbide (3C-SiC) with a lattice parameter of 4.36 Å [97]. In total, 3,900,208 atoms are generated.

In the study, free solidification technique is utilized to simulate the solidification process. Periodic boundary conditions are applied in three coordinate directions. The simulation starts with a solid SiC region, a solid Al region (thickness 5 nm in z direction) and a liquid Al region separated by a nominally flat liquid-solid boundary. The two phase Al system is established by holding fixed the atoms in solid Al region of the original crystalline lattice and melting the liquid Al region by raising the temperature to some temperature above the melting point. Upon solidification, both the solid Al atoms at the bottom and the liquid Al atoms at the top can move freely into each other because of the periodic boundary conditions. The velocity of the atoms is then rescaled to some temperature below the melting point. Due to the density difference between solid and liquid, constant volume simulations will lead to a gradual build up of pressure during crystallization which eventually halts solidification [99]. Instead, constant pressure conditions are required with the pressure maintained at zero throughout the run with a time step

of 1 fs. During solidification the solid atoms at the bottom which were initially fixed in position are allowed to move. The simulation is terminated when complete solidification is achieved (about 600 ps).

Interatomic potentials for aluminum, silicon carbide and the interface are discussed in the following sections.

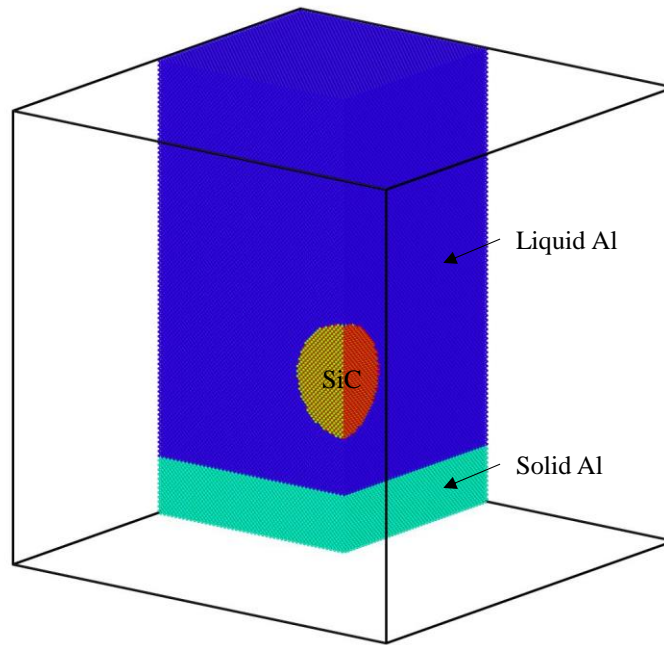


Figure 3.6 MD geometry model

3.4.1 EAM Potential for Aluminum

In this study the EAM model developed by Mishin *et al.* [116] as shown in equation (3-25) is used to simulate bulk aluminum. A cut-off distance $r_c = 6.365 \text{ \AA}$ is used [117].

$$E_{tot} = \frac{1}{2} \sum_{ij} V(r_{ij}) + \sum F(\bar{\rho}_i) \quad (3-25)$$

$$\bar{\rho}_i = \sum_{j \neq i} \rho(r_{ij}) \quad (3-26)$$

where $V(r_{ij})$ is the pair potential as a function of the atomic separation distance r_{ij} between two atoms i and j , F is the embedding energy as a function of the density $\bar{\rho}_i$, which is induced on atom i by all other atoms in the system, and $\rho(r_{ij})$ is the atomic density function. The interatomic potentials for Al are available from [117].

3.4.2 Tersoff Many-body Potential for Silicon Carbide

The Tersoff potential V_{ij} in the simplest sense is composed of the attractive and repulsive interactions present in a bond as shown in equation (3-27).

$$V_{ij} = f_C(r_{ij})[f_R(r_{ij}) + b_{ij}f_A(r_{ij})] \quad (3-27)$$

where the subscript R and A correspond to the repulsive and attractive component of the potential. The potential is a function of b_{ij} , two energy constants and $f_R(r_{ij})$, $f_A(r_{ij})$ and $f_C(r_{ij})$, which are functions representing the potential associated with the repulsive, attractive and cut-off functions. These functions are dependent on the length of the bond. In the aforementioned equations the subscripts i and j label the atoms of the system, and r_{ij} is the length of the ij bond. The necessary equations along with the energy constants and corresponding cut-off distances for silicon carbide are summarized in Tersoff [90, 91]. See Appendix I for detailed values for SiC Tersoff potential.

3.4.3 Potential for Describing the Interface

Ideally any interatomic potential model employed for representing the interface should include two-body and three-body interactions. Two-body interactions are the interaction between

Al-Si and Al-C while three-body interactions involve Al-Si-C, Al-C-Si, Al-Si-Al and Al-C-Al. In this study, in order to simplify the simulation procedure and in turn reduce the computational time a two-body pair-wise potential is used.

Two popular potentials, Lennard-Jones (LJ) potential and Morse potential, are usually used to model the Al-SiC interface. But according to Dandekar [97], The Morse potential values parameterized from ab initio data are able to best represent the current system and is therefore used in this study to represent the interface.

$$V = D_0[e^{-2\alpha_m(r-r_0)} - 2e^{-\alpha_m(r-r_0)}] \quad (3-28)$$

Where r is the distance between the atoms, r_0 is the equilibrium bond distance, D_0 is the well depth of the potential, α_m is the width of the potential, and V is the interatomic potential. The parameters are summarized in Table 3.1 [118].

Table 3.1 Morse potential function parameters parameterized to the ab initio data obtained

System	Parameters	Morse potential
Al-Si	D_0 (eV)	0.4824
	α (1/Å)	1.322
	r_0 (Å)	2.92
Al-C	D_0 (eV)	0.4691
	α (1/Å)	1.738
	r_0 (Å)	2.246

3.5 Solution Procedure

A MHD model is developed in ANSYS Maxwell and ANSYS Fluent. The Lorentz force density is obtained in Maxwell and then interpolated on the Fluent finite volume mesh and used as momentum source in solving the fluid flow. The procedure is shown in Figure 3.7 in detail.

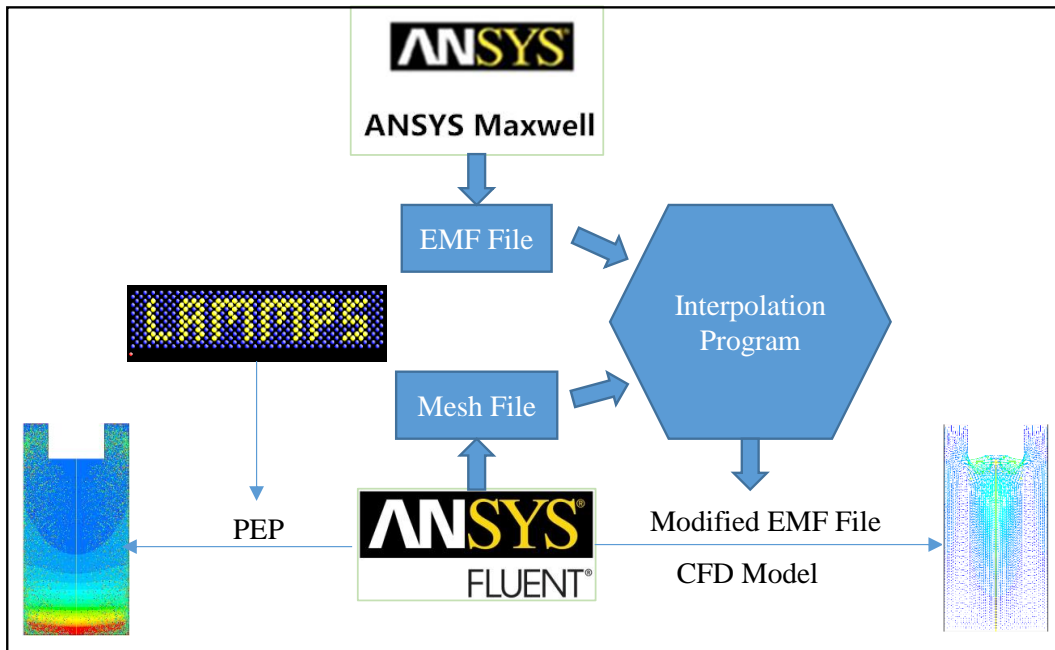


Figure 3.7 Schematic of the simulation procedure

In the CFD model, the SiC nanoparticles are injected at every fluid flow time step with a mass flow rate of 0.014 kg/s in the first second. The distribution of the particle diameters varying from 45 nm to 65 nm follows the Rosin-Rammler expression. Particles are tracked at every time step after the fluid velocity field is solved. Because of the low volume fraction of the discrete phase, one-way coupling is employed, which neglects the effect of the discrete phase on the fluid turbulence.

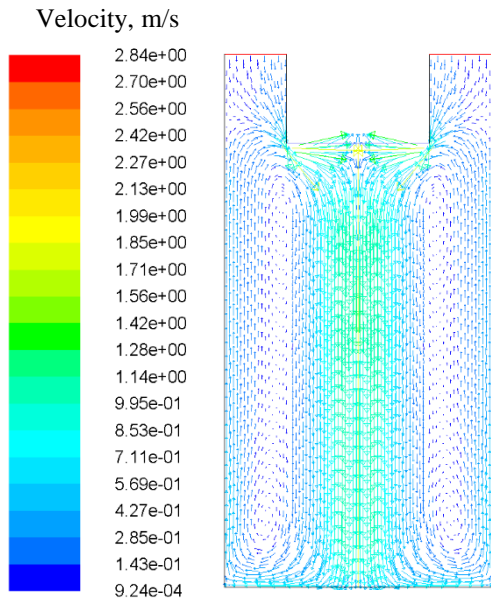
CHAPTER 4 – SIMULATION RESULTS AND DISCUSSION

Firstly, a CFD model without induction (electromagnetic) stirring (EMS) and solidification particle engulfment and pushing model (PEP) is built in ANSYS Fluent to observe the basic characteristics of fluid flow and nanodispersion, and investigate the effects of injection position, gravity and intensity of ultrasonic stirring on the dispersion of nanoparticles. Then, solidification (PEP) is incorporated into the CFD model to study the behavior of nanoparticles during solidification process. Finally, the CFD model is coupled with electromagnetic field during molten metal process, and the effects of electromagnetic stirring and intensity of the ultrasonic stirring are analyzed.

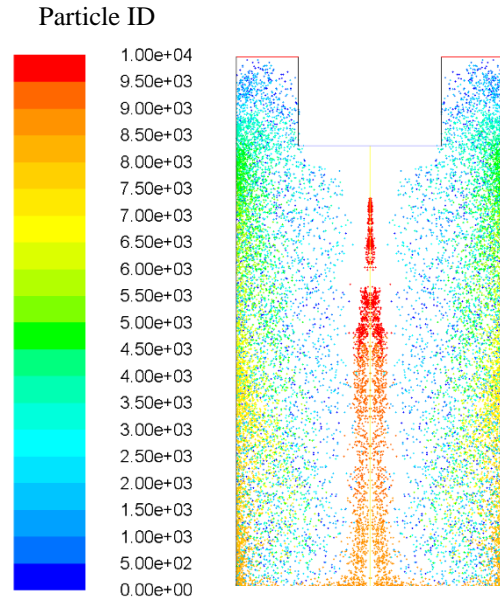
4.1 Results without EMS and PEP

Figure 4.1 shows the fluid flow (colored by velocity magnitude, similarly hereinafter unless otherwise stated) and particle distribution (colored by particle ID, similarly hereinafter unless otherwise stated) after 1.0s and 3.0s, respectively.

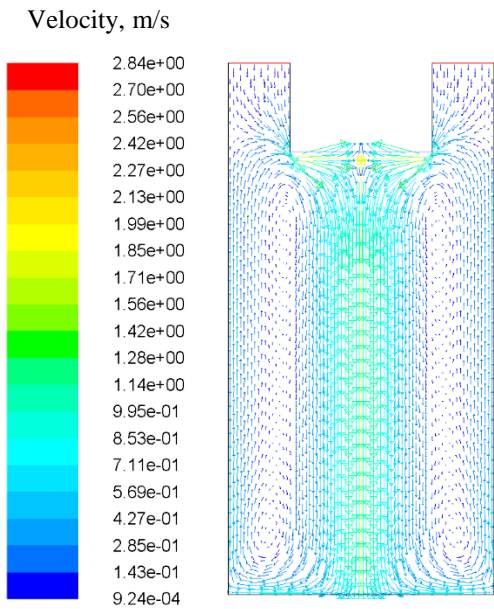
It can be seen from Figure 4.1 (a) and (c) that the flow is much stronger at the center of the furnace. It demonstrates that the particles have little effect on the fluid flow because of the one-way coupling, and the gravity direction is the same as the direction of the stronger flow in the center, so it will help to develop the fluid flow. Therefore the fluid flow after 3.0s is almost the same as that after 1.0s because both of them are fully developed.



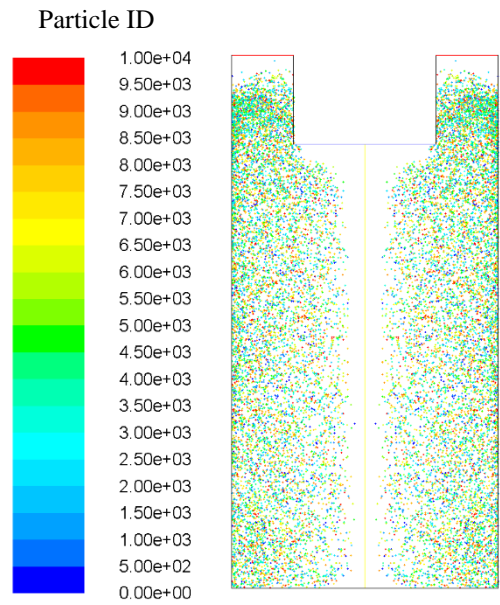
(a) After 1.0s



(b) After 1.0s



(c) After 3.0s



(d) After 3.0s

Figure 4.1 Fluid flow and particle distributions after 1.0s and 3.0s

At 1.0s when the injection is stopped, newly injected particles are still at the center of the furnace where they are injected, since more time is needed for all of them to be dispersed into the liquid. It is obviously observed that the particles are following the fluid flow. In the beginning, they are carried by the flow in the center to the bottom, and then back to the top near the wall. Then 2.0s later, the particles have been dispersed pretty well from the bottom to the top, but a few more particles tend to stay near the wall, and fewer nanoparticles at the center where the flow is stronger, which indicates the nanoparticles are taken away by strong flows. Additionally, the particle distribution stays almost the same henceforth which means the distribution becomes stable.

When the particles are injected from a different position which is about 20mm above the bottom of the furnace, the distributions of the particles after 1.0s and 3.0s are shown in Figure 4.2, respectively.

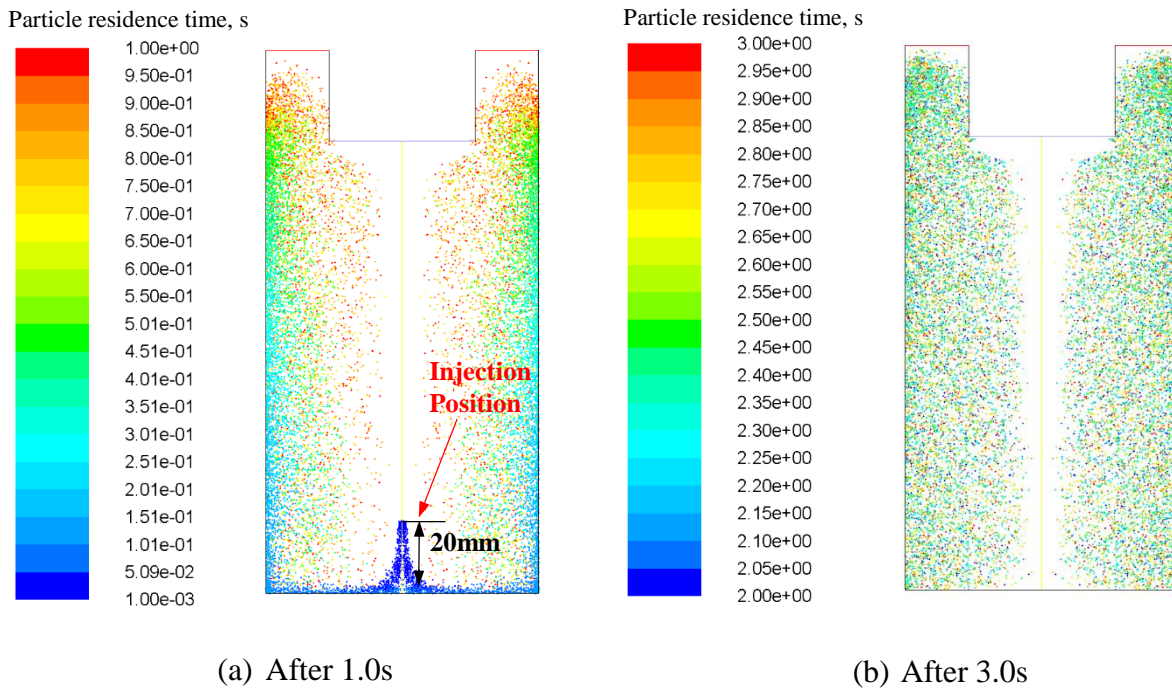


Figure 4.2 Particle distributions after 1.0s and 3.0s with a different injection location

It can be seen, the particle distribution after 1.0s is not the same as before. But, after 3.0s when the distribution becomes stable, it has little difference with that when the particles are injected at the top, which demonstrates that the injection position will not affect the final distribution of the SiC nanoparticles, as long as the fully developed fluid flow is strong enough to disperse the nanoparticles throughout the furnace.

Figure 4.3 presents the fluid flow after 1.0s and 3.0s when the ultrasonic probe is placed at the bottom of the furnace. In order to compare with previous results more conveniently, the whole system is turned upside down, which is equivalent to reverse the gravity direction.

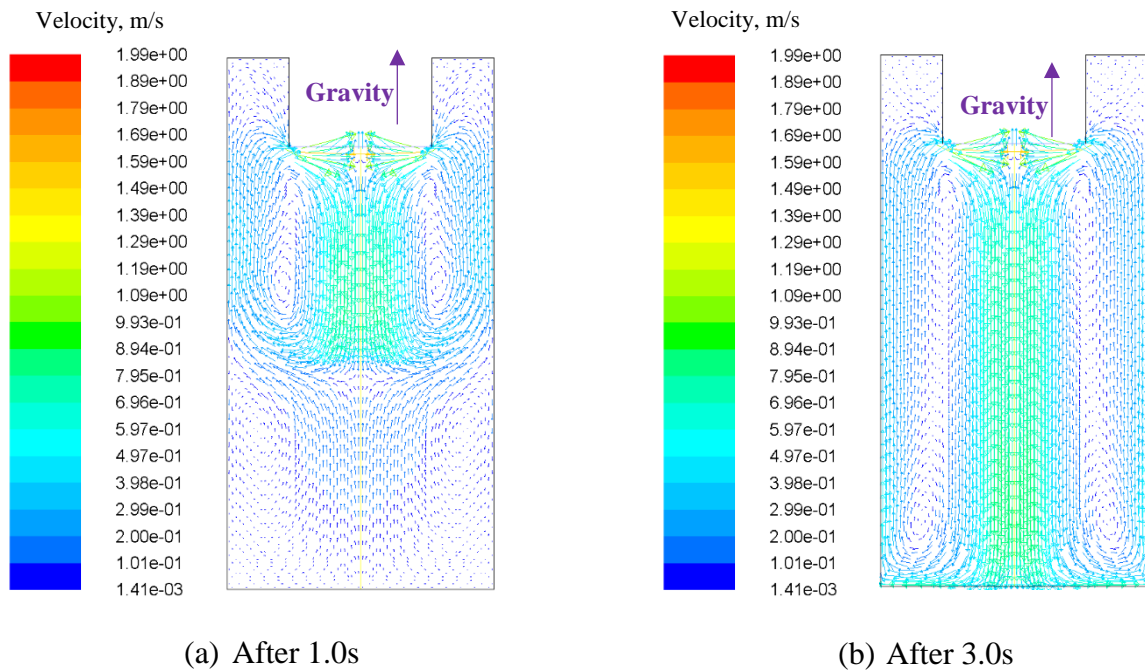


Figure 4.3 Fluid flow after 1.0s and 3.0s with the ultrasonic probe placed at the bottom of the furnace (gravity direction upward)

It can be seen that the flow fields after 1.0s and 3.0s are not the same though a one-way coupling is used. This is because the gravity direction is opposite to the direction of the stronger

flow in the center of the furnace, thus retarding the development of the fluid flow and resulting in a different flow pattern at 1.0s. But after 3.0s, the fluid flow is fully developed and becomes almost the same as that of the case with a different gravity direction, because the gravitational force is relatively weak compared to the drag force, if the flow is very strong.

Figure 4.4 shows the particle distributions after 1.0s and 3.0s with the ultrasonic probe placed at the bottom of the furnace.

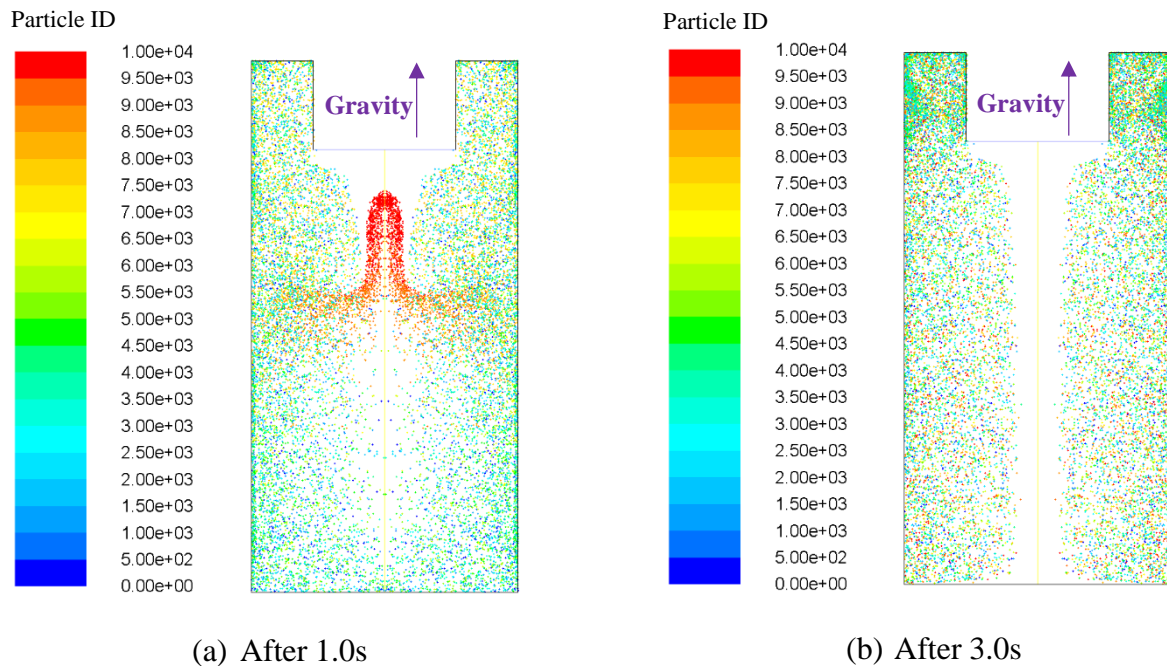


Figure 4.4 Particle distributions after 1.0s and 3.0s with the ultrasonic probe placed at the bottom of the furnace (gravity direction upward)

As it can be seen that the distribution at 1.0s is not the same as before due to a new flow pattern. But after 3.0s, when the fluid flow is fully developed, the distribution of nanoparticles becomes uniform and looks similar as before. The general trend is basically the same, i.e., where the flow is stronger, there are fewer particles, and vice versa. It indicates that the effect of gravity

on the nanodispersion during molten metal process is negligible compared with the other forces, such as the drag force. Besides, a few more nanoparticles can be observed around the ultrasonic probe compared with previous cases.

To investigate the effect of intensity of ultrasonic stirring, the inlet velocity magnitude is changed to be 1/10th of the origin one (Figure 3.3). The fluid flow after 1.0s and 20.0s are shown in Figure 4.5. As it can be seen, the flow is much weaker at 1.0s, and it takes longer for it to fully develop. But the fully developed flow pattern is almost the same as before.

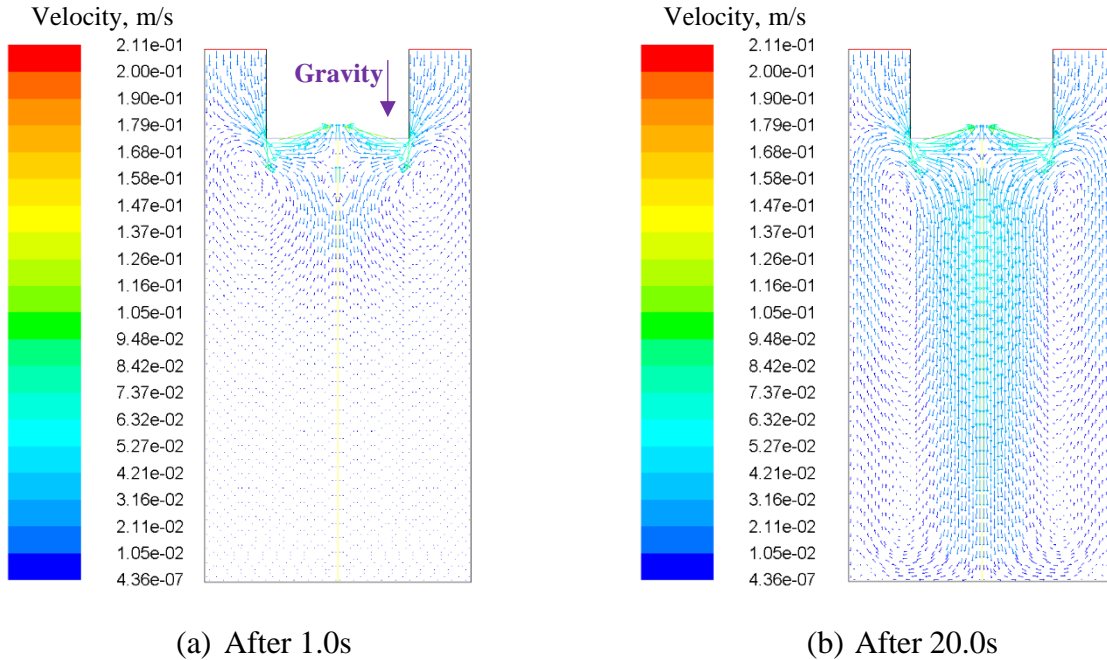


Figure 4.5 Fluid flow after 1.0s and 20.0s with a weaker flow

(gravity direction downward)

As the fluid flow is much weaker, the dispersion of the particles is much slower. After 20.0s, the distributions of the nanoparticles with different injection positions, which are shown in Figure 4.6, become almost stable.

Compared with previous results with a stronger flow (Figure 4.1(d) and Figure 4.2(b)), nanoparticle distributions at stable state are different. When the particles are injected at the bottom of the furnace, plenty of them aggregate at the bottom because the fluid flow near the wall is too weak to take them to the top. On the contrary, when they are injected at the top, they can be taken to the bottom by the relatively stronger flow at the middle of the furnace, which results in a much more uniform distribution of the particles.

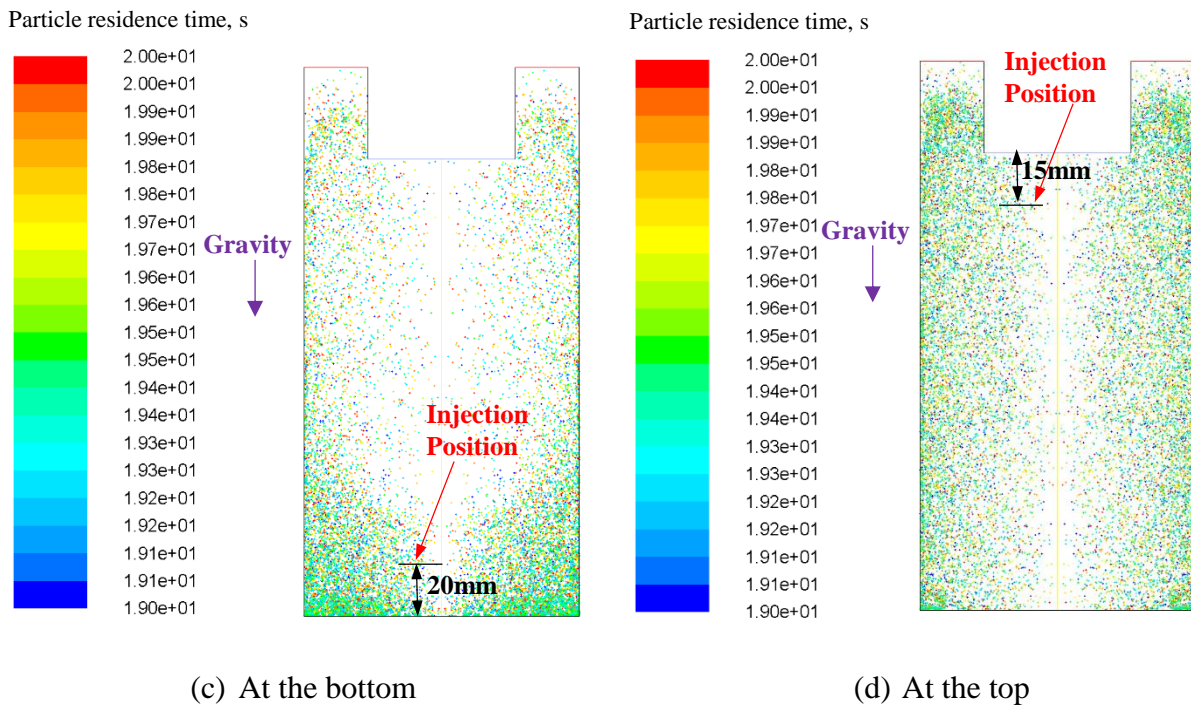


Figure 4.6 Particle distributions after 20.0s with two different injection positions and a weaker flow (gravity direction downward)

4.2 Results with PEP Model Only

When the nanoparticles are well dispersed and the distribution becomes stable after 3.0s, the solidification process starts, and in order to model the unidirectional solidification process, all the other walls except the bottom one are treated as adiabatic (no heat flow).

Figure 4.7 shows the fluid flow after 10.0s and 30.0s, respectively. It can be seen, when solidification starts, the fluid flow is damped in the mushy zone, where the particles will move relatively slow and eventually stop moving in the solid, which agrees well with theoretical expectation.

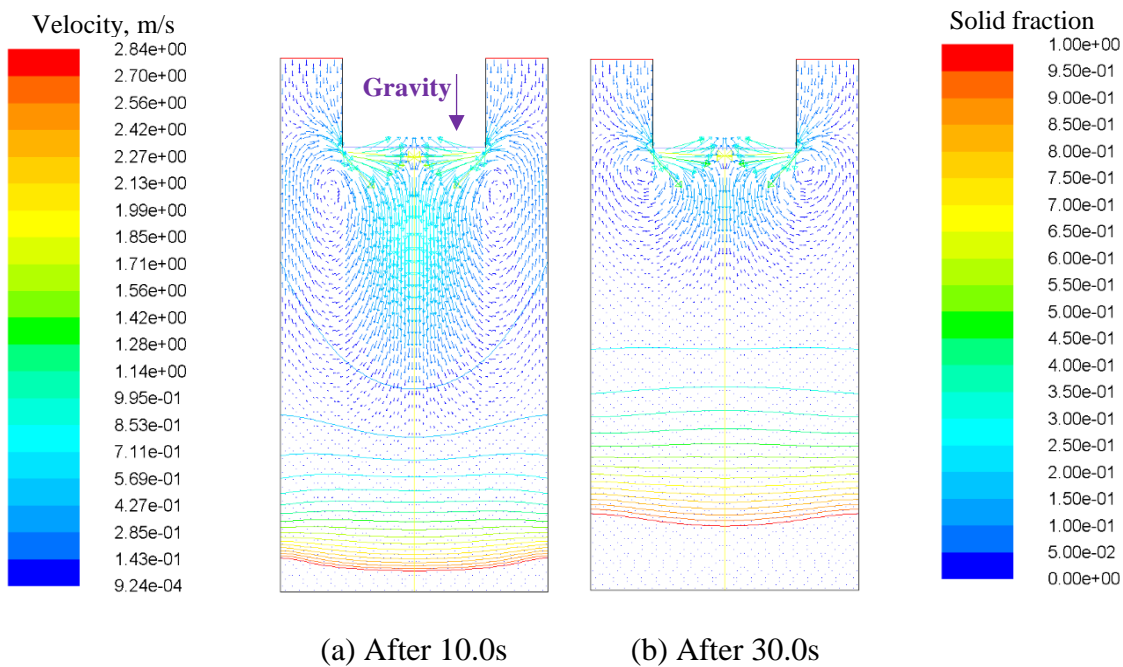


Figure 4.7 Fluid flow after 10.0s and 30.0s (gravity direction downward)

Figure 4.8 shows the particle distributions after 10.0s and 30.0s, respectively. After 10s, we can see that there are some agglomerations in the solid because the nanoparticles approaching

the solid/liquid interface will be engulfed based on the assumption that the Brownian motion will dominate during the particle engulfment/pushing process.

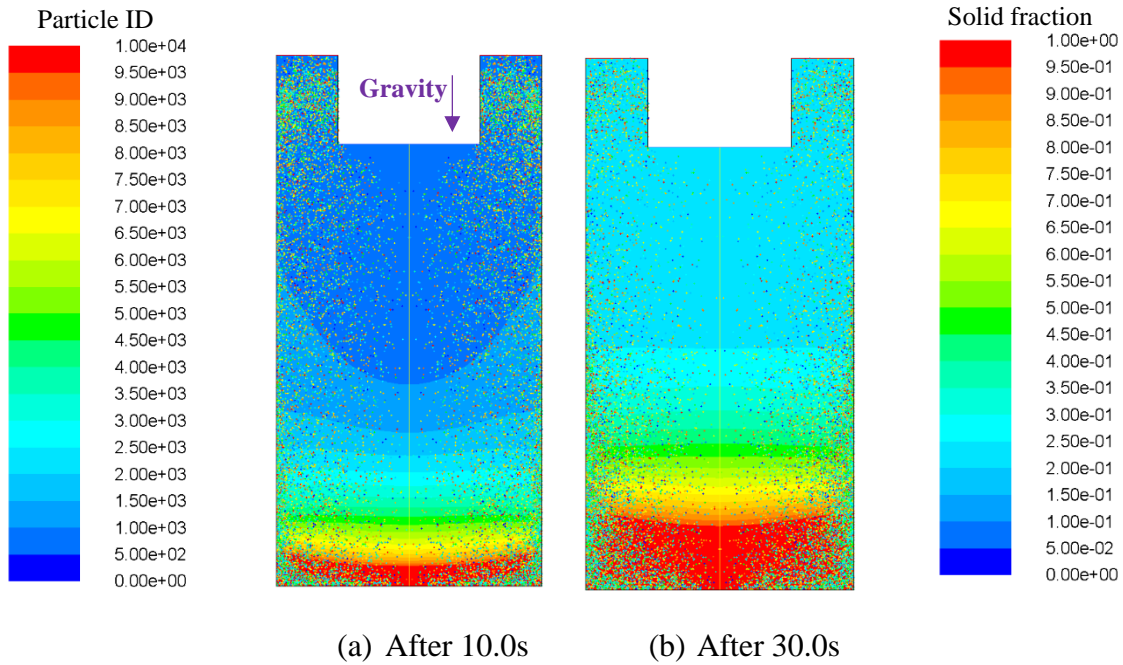


Figure 4.8 Particle distributions after 10.0s and 30.0s (gravity direction downward)

Figure 4.9 and Figure 4.10 present the fluid flow and particle distributions after 10.0s and 20.0s with the gravity direction upward. It can be seen that during solidification the fluid flow is damped in the mushy zone and becomes weaker as explained before. Then the gravity begins to play an important role in the flow. After 20s, the flow in the center even has an opposite direction as before, which is the same as the gravity direction, and accelerate the solidification process.

As the solidification continues, the entire domain is fully solidified after only around 30s (this result is not shown). The gravity effect on the dispersion of the nanoparticles is not significant in the molten metal. But as explained above, the gravity will make a big difference

during the solidification process, reducing the solidification time and producing well dispersed nano-composites quickly.

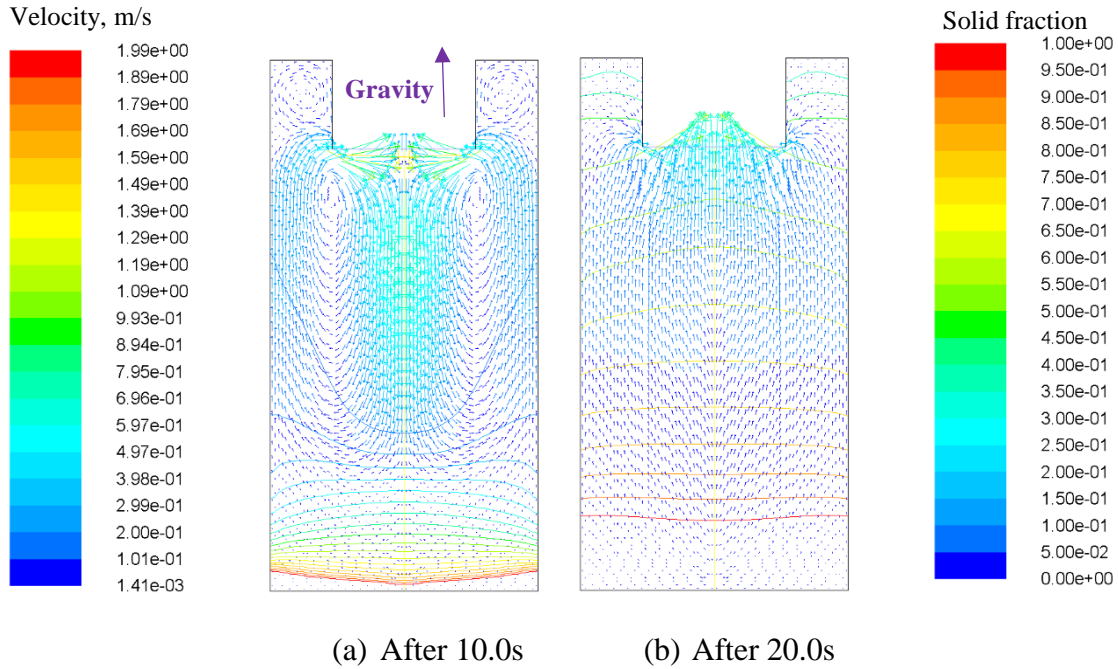


Figure 4.9 Fluid flow after 10.0s and 20.0s (gravity direction upward)

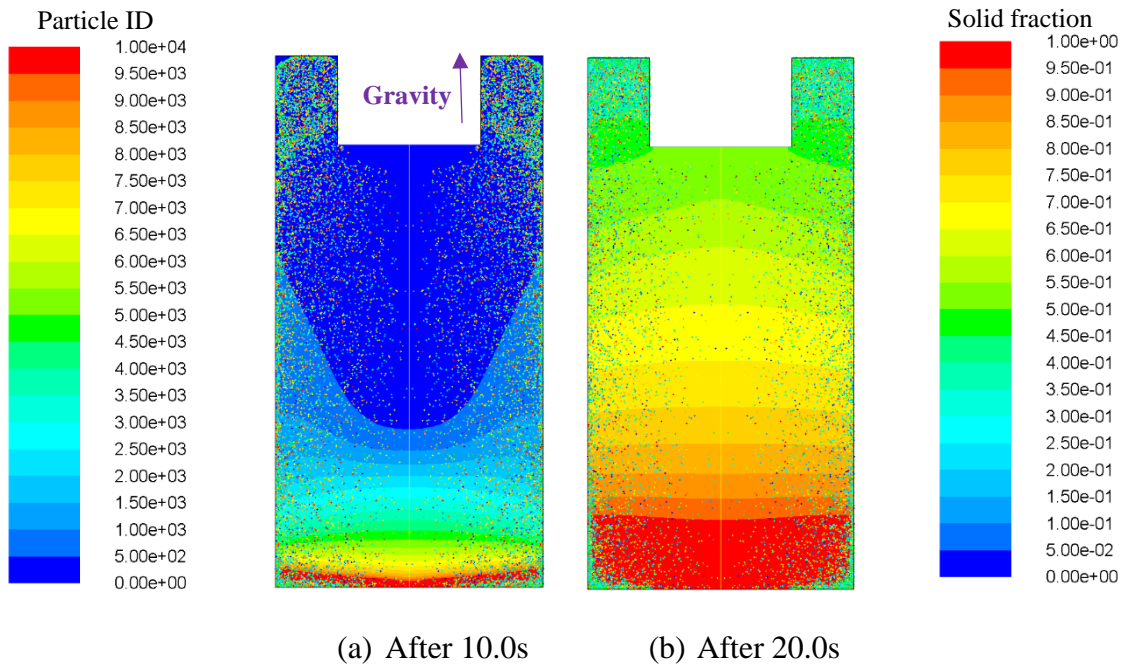


Figure 4.10 Particle distributions after 10.0s and 20.0s (gravity direction downward)

As discussed before, for a weaker flow condition, the distribution of nanoparticles gets stable after 20.0s, at which we start the solidification process. Figure 4.11 and Figure 4.12 show the fluid flow and particle distribution after 30.0s and 50.0s with a weaker flow, respectively. It can be seen that 10.0s later after the solidification starts, the fluid flow around the ultrasonic probe (top) becomes more turbulent than before, and several vortexes turn up (see Figure 4.11(a)), but the overall distribution of the nanoparticles stays almost the same (see Figure 4.12 (a)). After 50.0s, it is obvious that more particles are captured by the mushy zone, and almost no particles are at the top of the furnace, which indicates that the uniformity of the particles deteriorates (see Figure 4.12 (b)).

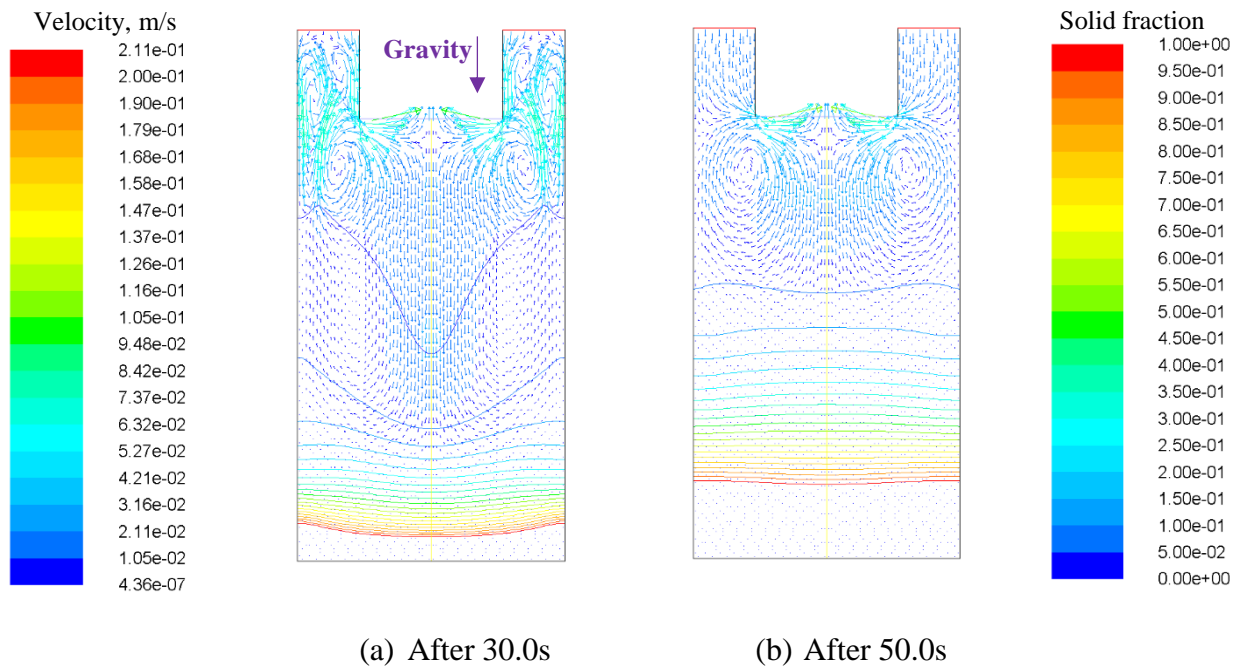


Figure 4.11 Fluid flow after 30.0s and 50.0s with a weaker flow (gravity direction downward)

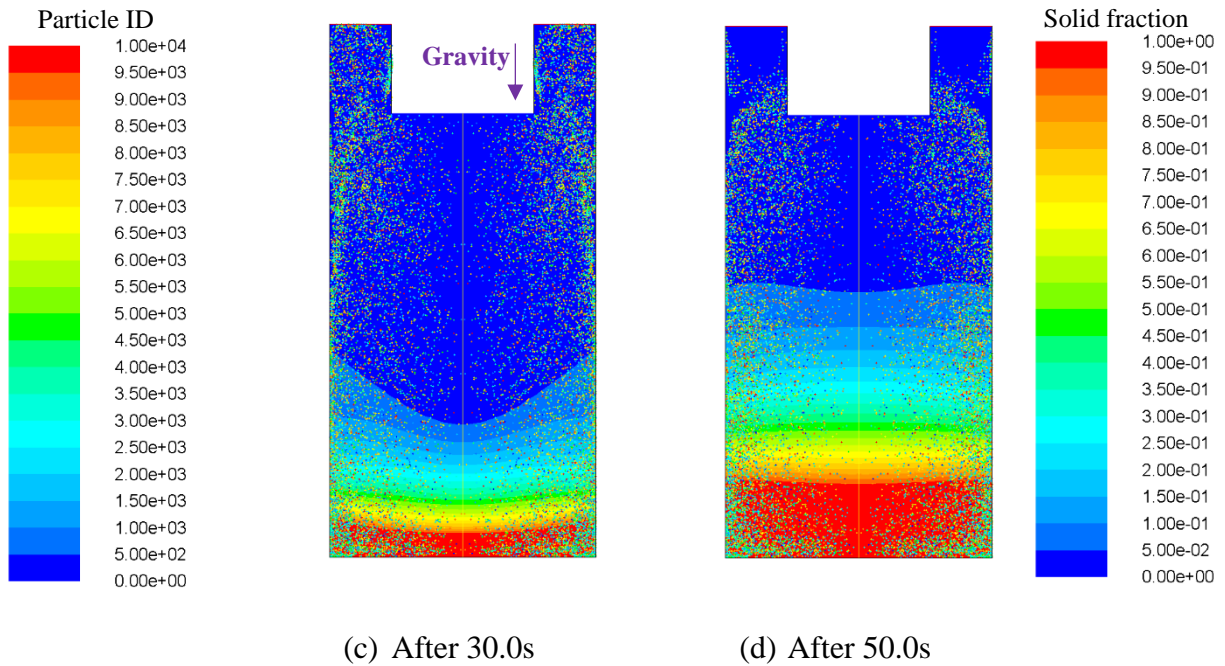
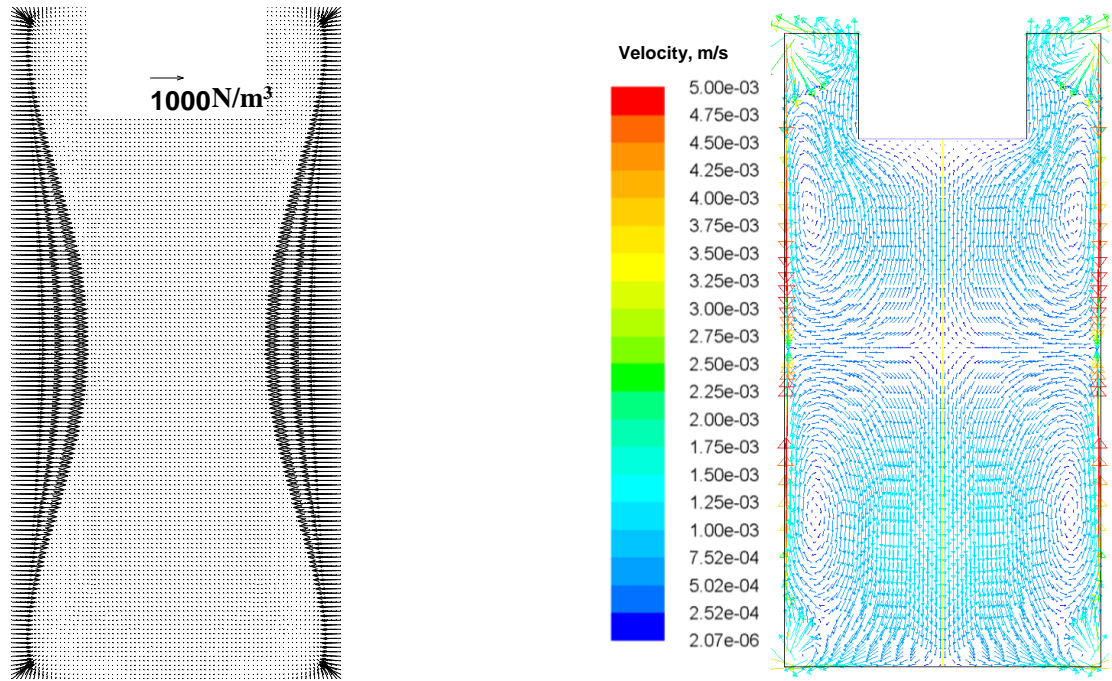


Figure 4.12 Particle distributions after 30.0s and 50.0s with a weaker flow
(gravity direction downward)

4.3 Results with EMS only

Figure 4.13 shows the electromagnetic force distribution interpolated on the Fluent finite volume mesh and fluid flow field in the induction furnace after 1.0s without ultrasonic stirring.

As it can be seen, the electromagnetic forces mainly distribute in the skin layer due to skin effect. Also, the flow consists of two axisymmetric recirculating loops, consistent with the computed curl of the EM force field.

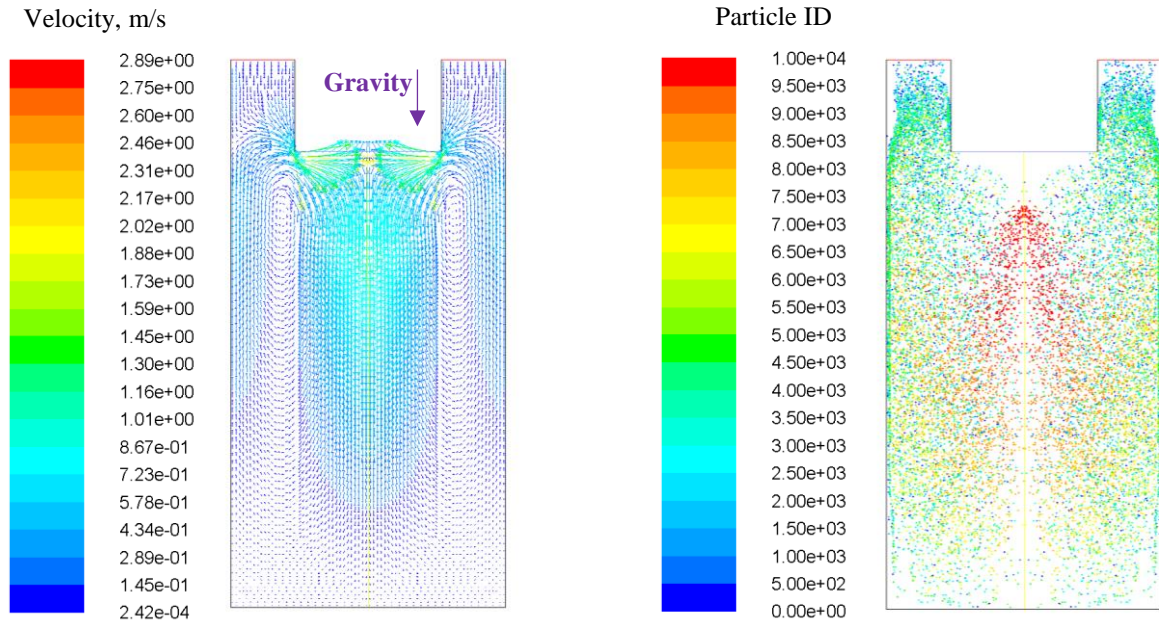


(a) Electromagnetic force distribution

(b) Fluid flow without ultrasonic stirring

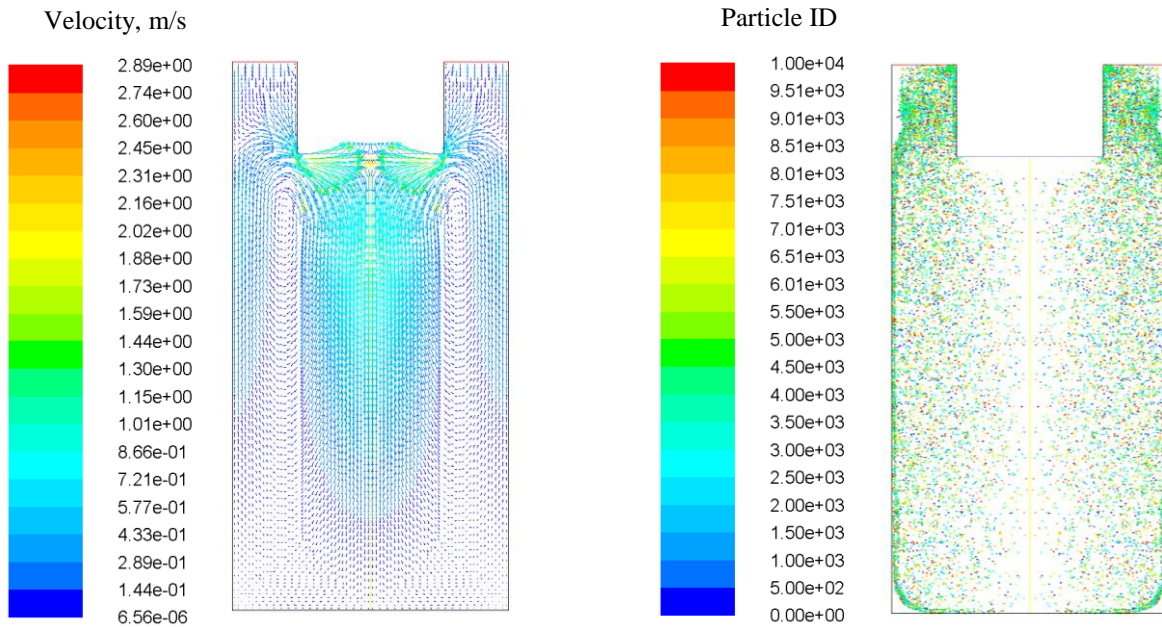
Figure 4.13 Electromagnetic force distribution and fluid flow field without ultrasonic stirring

When the induction stirring is taken into consideration, the fluid flow and particle distributions after 1.0s and 3.0s are shown in Figure 4.14, respectively. Compared to the results without EMS (Figure 4.1), the fluid flow pattern is basically the same, because the induced flow by induction stirring is relatively weak compared to that induced by ultrasonic stirring. But there are still some differences especially at the center of the furnace that the flow at the bottom becomes weaker than that at the top because of the induction stirring. It can also be seen that there are considerable number of particles in the center of the furnace, which indicates that the particle distribution becomes even better than before. It can be explained that induction stirring modifies the fluid flow, making it more uniform.



(a) After 1.0s

(b) After 1.0s



(c) After 3.0s

(d) After 3.0s

Figure 4.14 Fluid flow and particle distributions after 1.0s and 3.0s with EMS

(gravity direction upward)

As it can be seen in Figure 4.14 (d) that, after 20s, the nanoparticles are dispersed quite well throughout the metal matrix, which is also validated by SEM analysis [119, 120].

Figure 4.15 and Figure 4.16 show the fluid flow and particle distributions with a weaker flow and EMS after 1.0s and 20.0s, respectively. As the fluid flow is weaker, the particle dispersion is slower. And the flow fields after 3.0s and 20s are not exactly the same, because the flow after 3.0s is not fully developed yet. Besides, even the fully developed flow pattern is not as regular as before (see Figure 4.5(b)), that there are several recirculating loops, because the induction stirring, which cannot be neglected, is playing a major role on the fluid flow.

After 20s, the distribution of the nanoparticles becomes stable, but it changes a lot compared to Figure 4.6(b), there are much fewer particles at the top (around the probe) where fluid flow is relatively stronger.

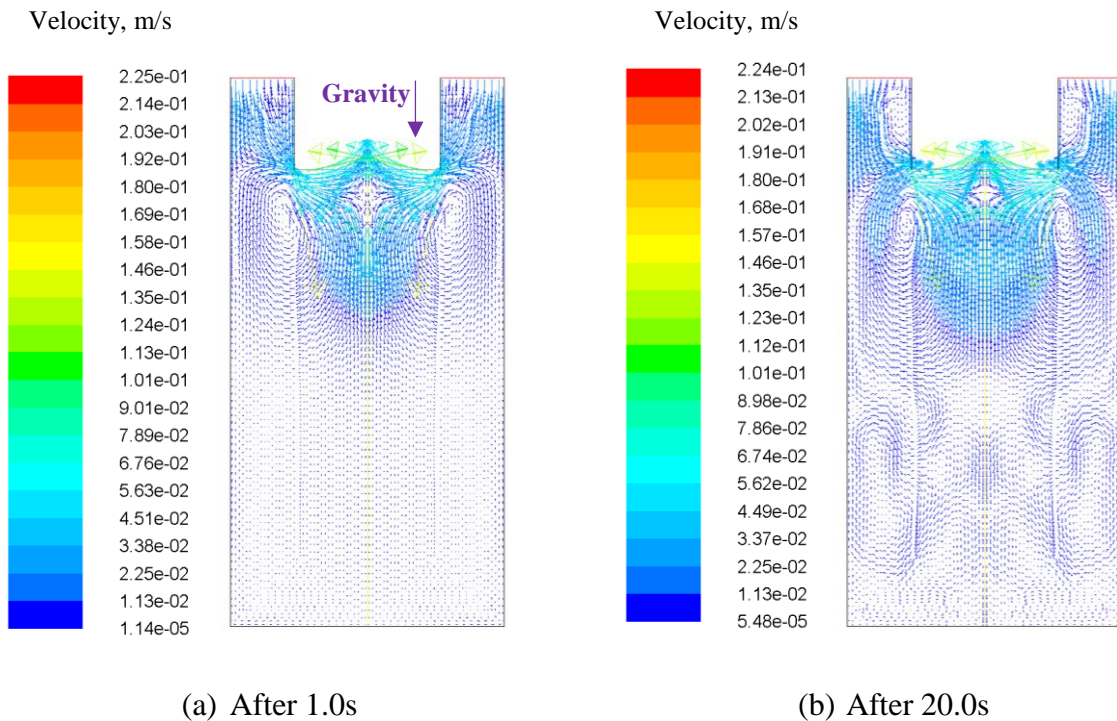


Figure 4.15 Fluid flow after 1.0s and 20.0s with a weaker flow and EMS

(gravity direction downward)

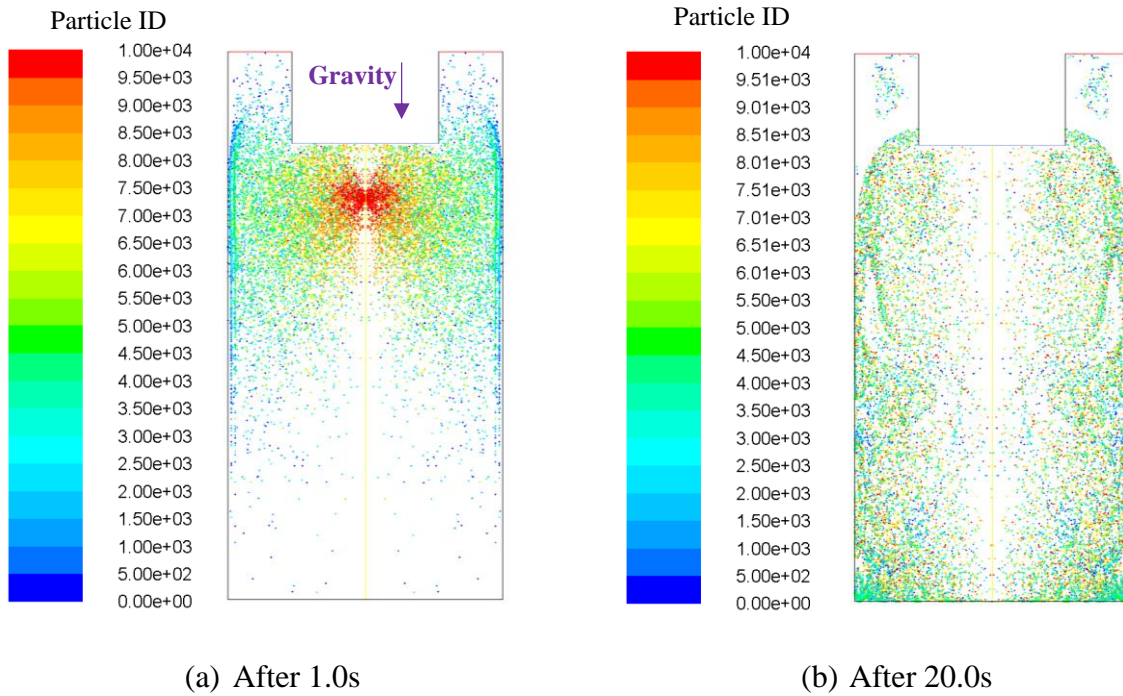


Figure 4.16 Particle distributions after 1.0s and 20.0s with a weaker flow and EMS
(gravity direction downward)

4.4 Results with both EMS and PEP Model

Figure 4.17 shows the fluid flow and particle distributions after 10.0s and 30.0s with EMS during solidification process, respectively. As it can be seen, when solidification starts, the fluid flow is damped in the mushy zone as well, and particles approaching the solidification front are captured. As it can be seen in Figure 4.17(d) that, after 20s, the nanoparticles are dispersed quite well throughout the metal matrix, which is also validated by SEM analysis [119, 120]. Generally speaking, the fluid flow and nanoparticle distributions don't change too much compared with the results without EMS when the fluid flow is strong.

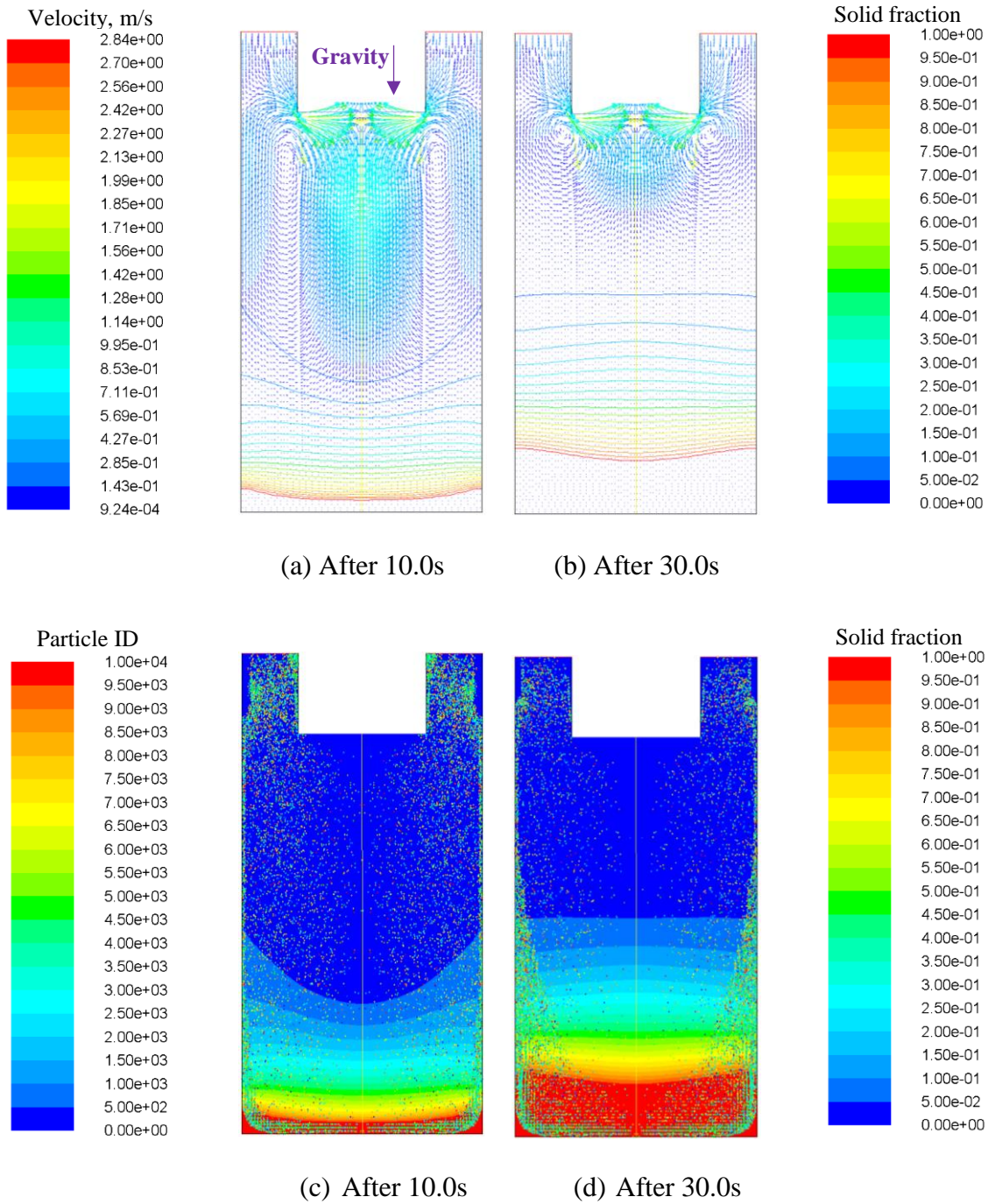


Figure 4.17 Fluid flow and particle distributions after 10.0s and 30.0s with EMS
(gravity direction downward)

In order to perform a more detailed particle distribution analysis, the geometry is divided into 150 slices (1 mm each) along vertical direction and 75 slices (0.5 mm each) along radial direction, thus there are 11250 cells in total (including the probe area). The numbers of particles in each slice and cell are counted. Particle distributions along vertical and radial direction after 3s, 10s and 30s, and overall particle distribution after 30s are shown in Figure 4.18, Figure 4.19, and Figure 4.20, respectively.

It can be seen from Figure 4.18 that, the distribution along vertical direction after 3s is very uniform. As solidification starts, more and more particles are captured by the solidification front, thus there are fewer and fewer particles on the top of the furnace (away from the solidification area). In Figure 4.19, generally along radial direction, further away from the symmetry, more particles present. However, there is a peak at the middle area because of the flow vertex. Moreover, a more intuitive observation of the overall particle distribution can be obtained from Figure 4.20.

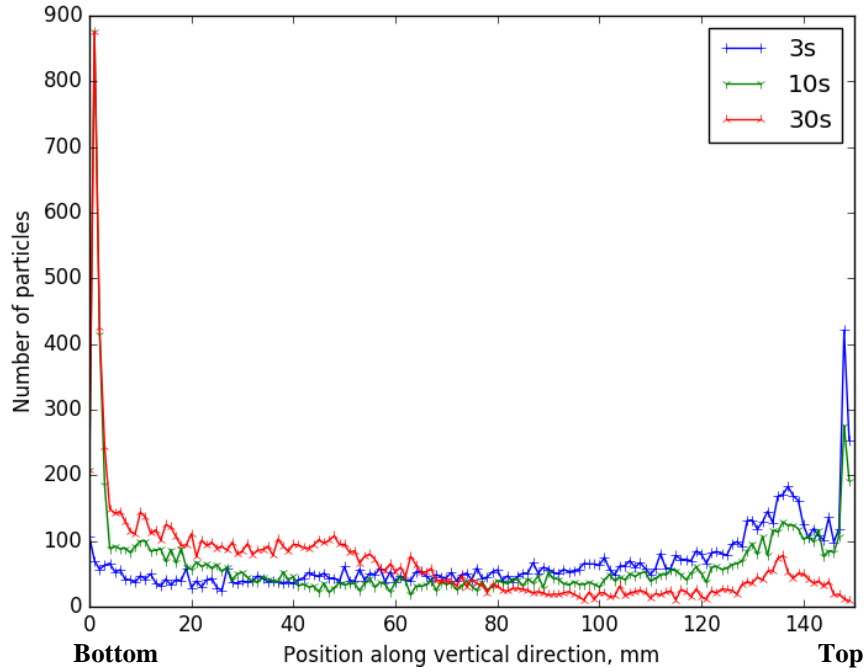


Figure 4.18 Particle distribution along vertical direction after 3s, 10s, and 30s

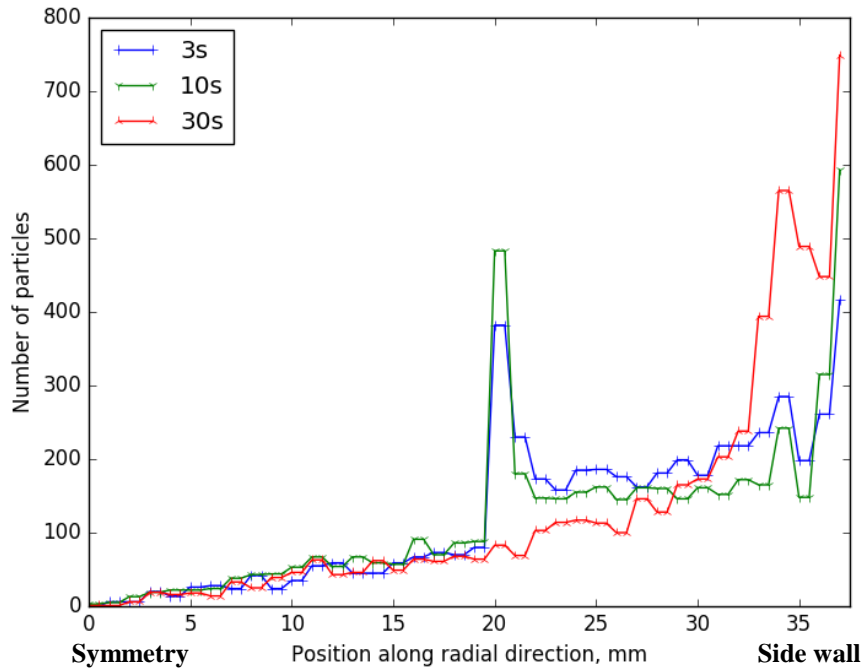


Figure 4.19 Particle distribution along radial direction after 3s, 10s, and 30s

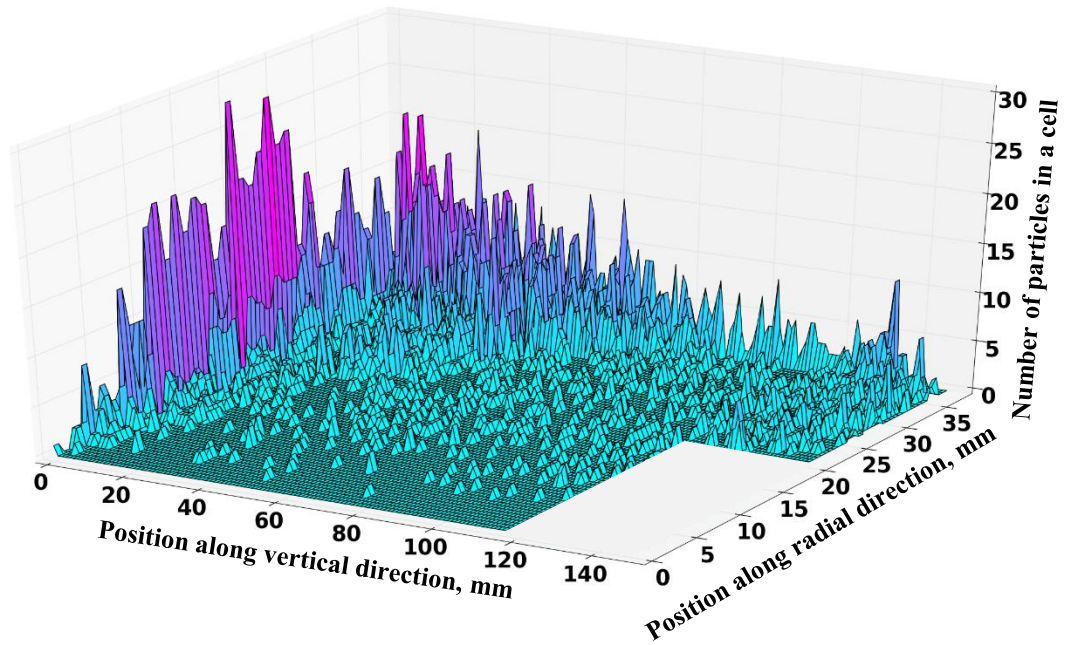


Figure 4.20 Overall particle distribution after 30s

Figure 4.21 shows the fluid flow after 30.0s and 50.0s with a weaker flow and EMS during solidification process, respectively. When solidification starts (after 20.0s), the fluid flow changes significantly because the induction stirring furnace is stopped. In addition, it can be observed that the flow pattern will become almost the same as that with a strong flow.

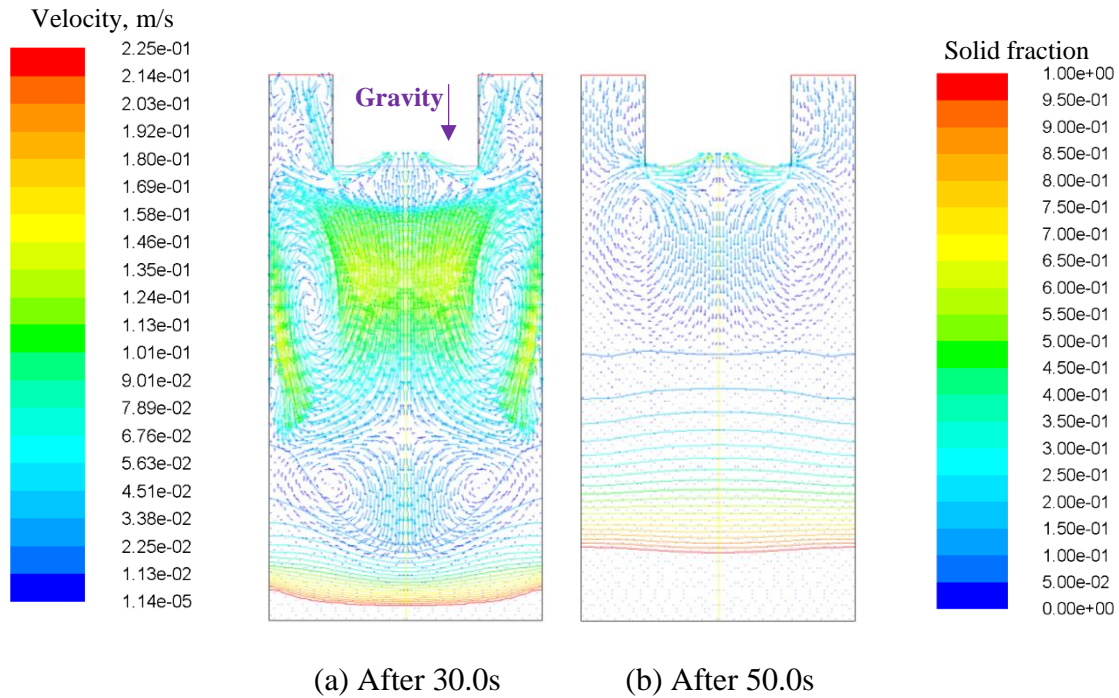


Figure 4.21 Fluid flow after 30.0s and 50.0s with EMS (gravity direction downward)

Figure 4.22 shows the particle distribution after 30.0s and 50.0s with a weaker flow and EMS during solidification process, respectively. As shown in Figure 4.16(b), for a weaker flow, after 20s, the distribution of the nanoparticles becomes stable. Then, 10s later after solidification starts (i.e. after 30.0s), the overall distribution of the nanoparticles becomes even more uniform because more particles can be taken to the top (see Figure 4.22(a)). Finally, 30s later after the start of solidification (i.e. after 50.0s), more particles are captured by the mushy zone, and consequently fewer particles stay at the top (see Figure 4.22(b)), however the overall distribution is still relatively uniform.

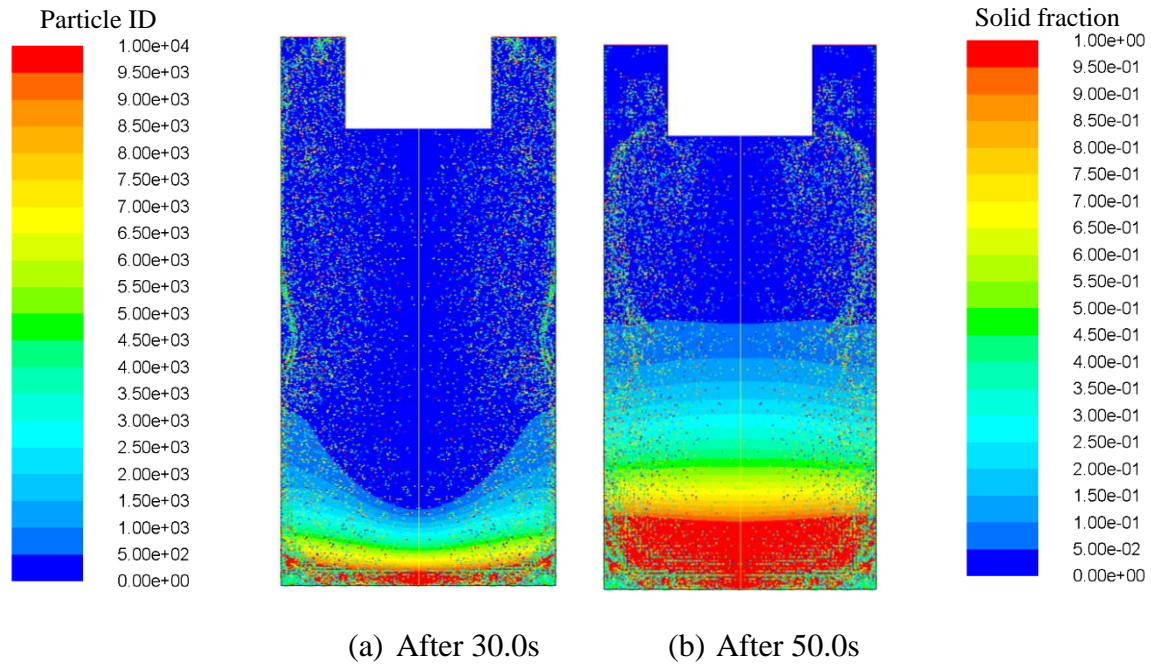


Figure 4.22 Particle distributions after 30.0s and 50.0s with EMS (gravity direction downward)

Particle distributions along vertical and radial direction after 20s, 30s and 50s, and overall particle distribution after 50s are shown in Figure 4.23, Figure 4.24, and Figure 4.25, respectively. It can be seen that the change of particle distribution during solidification is not as obvious as that with a stronger flow, and the peak of the distribution along radial direction is relatively smaller than before. From Figure 4.25, we can see that the distribution is even more uniform than that with a stronger flow (compared to Figure 4.20).

Table 4.1 shows the standard deviations of the overall particle distribution with strong flow (after 3s, 10s and 30s) and weak flow (after 20s, 30s and 50s). It confirms that the particle distributions with a weak flow is more uniform than those with a strong flow.

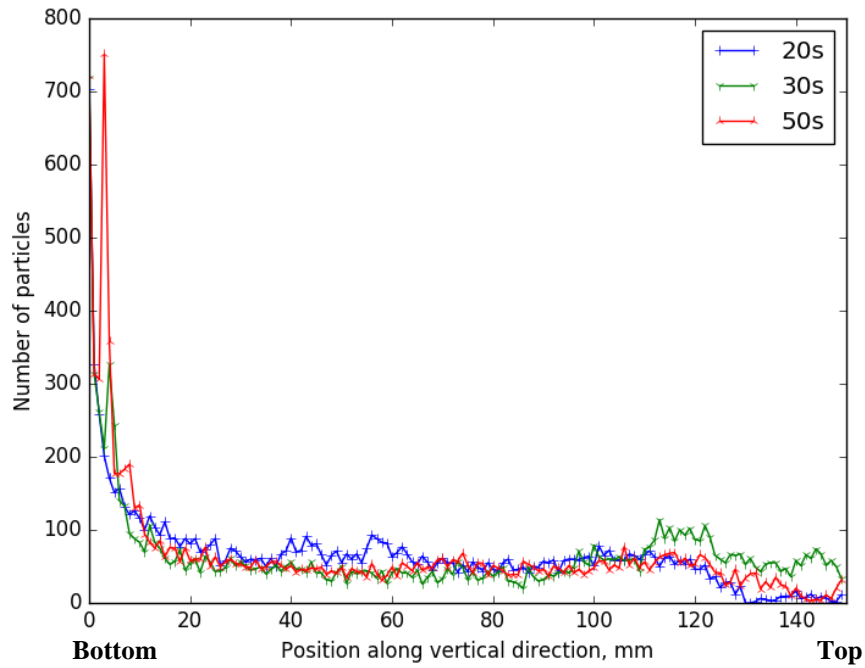


Figure 4.23 Particle distribution along vertical direction after 20s, 30s, and 50s

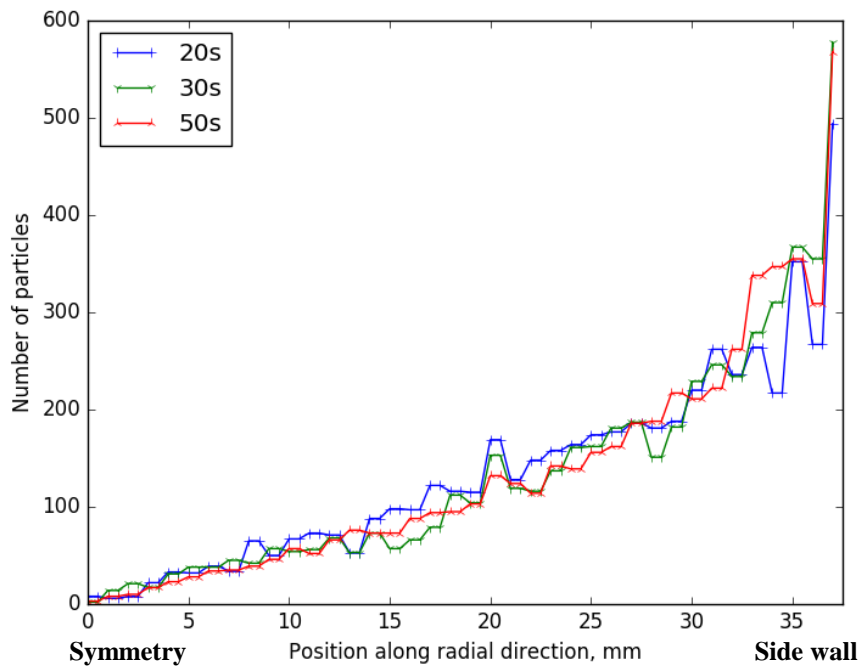


Figure 4.24 Particle distribution along radial direction after 20s, 30s, and 50s

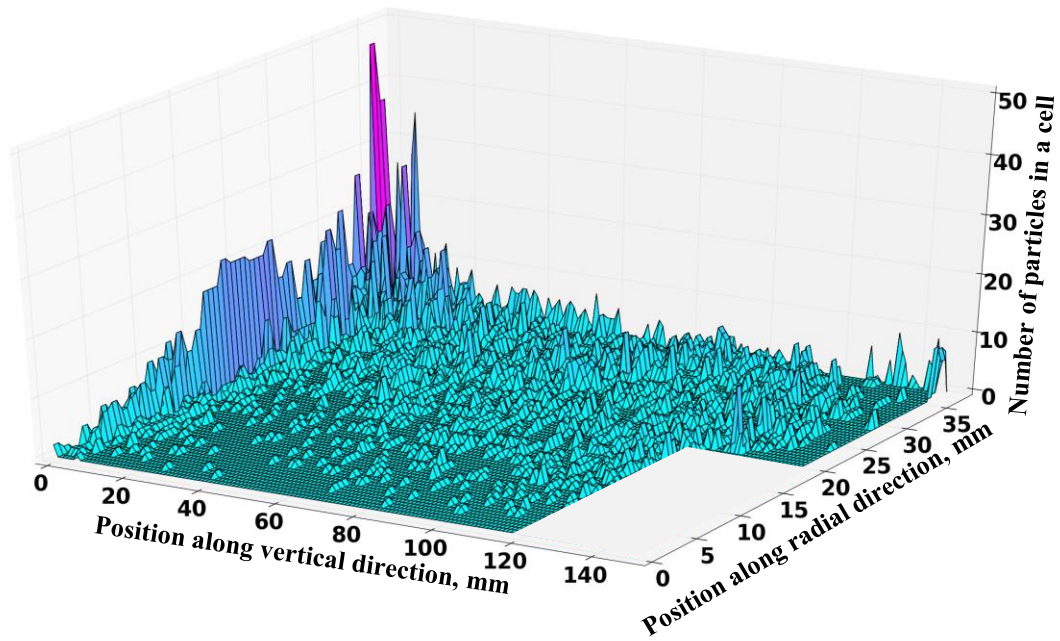


Figure 4.25 Overall particle distribution after 50s with a weaker flow

Table 4.1 Standard deviations of overall particle distribution with strong flow and weak flow

Strong flow		Weak flow	
After 3s	2.19	After 20s	1.80
After 10s	2.81	After 30s	1.87
After 30s	2.28	After 50s	2.15

4.5 Molecular Dynamics Simulation Results

In solid-state systems, the centro-symmetry parameter (CSP) developed by Kelchner et al. [121] is a useful measure of the local lattice disorder around an atom and can be used to characterize whether the atom is part of a perfect lattice, a local defect (e.g. a dislocation or stacking fault), or at a surface [22]. The CSP of an atom having N nearest neighbors is defined as

$$CSP = \sum_{i=1}^{N/2} |\mathbf{r}_i + \mathbf{r}_{i+N/2}|^2 \quad (4-1)$$

Where \mathbf{r}_i and $\mathbf{r}_{i+N/2}$ are vectors from the central atom to a particular pair of nearest neighbors.

The number of nearest neighbors taken into account is $N = 12$ for *fcc* and $N = 8$ for *bcc*. The CSP is close to zero for regular sites of a centrosymmetric crystal and becomes non-zero for defect atoms. If the atom does not have N neighbors (within the potential cutoff), then its centrosymmetry parameter is set to 0. For example, the SiC nanoparticle is constructed of diamond lattice structure which has 4 nearest neighbors. If N is set to be 12 for *fcc* (Al), then the CSP for Si and C atoms will always be 0. However, the method can only be applied to the class of centrosymmetric lattices (which does not include hcp, for example), and it provides no means of distinguishing multiple centrosymmetric crystal phases [122].

In the study, we use the centro-symmetry parameter (CSP) to discriminate between “liquid” and “solid” atoms in the cell. A color map from blue (0-solid) to red (18-liquid) is used as shown in Figure 4.26. However, the CSP of Al atoms at the surface and the interface of SiC and Al will always be treated as “liquid” atoms as can be seen in Figure 4.26.

In order to study the solidification process, we need to know the equilibrium melting temperature, which is a crucial reference point. A smaller system with dimensions of 6 nm×6 nm×20 nm and a $\Phi 2$ nm SiC particle is used to save computational time. Initially the top 1/4 and bottom 1/4 atoms are fixed, and the others are melted at high temperature of 2000K employing a Nose-Hoover thermostat as shown in Figure 4.27(a). Keeping the solid atoms fixed, the liquid atoms are subsequently quenched to an estimated melting temperature and equilibrated over 50 ps. Then, the whole system is allowed to relax up to 500 ps with the temperature maintained at the estimated value of T_m .

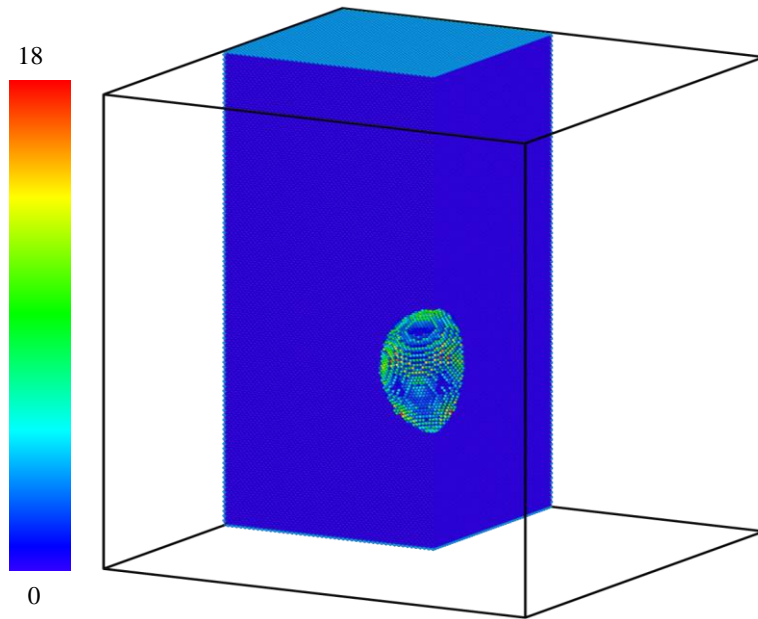


Figure 4.26 Centro-symmetry parameters for Al in the system

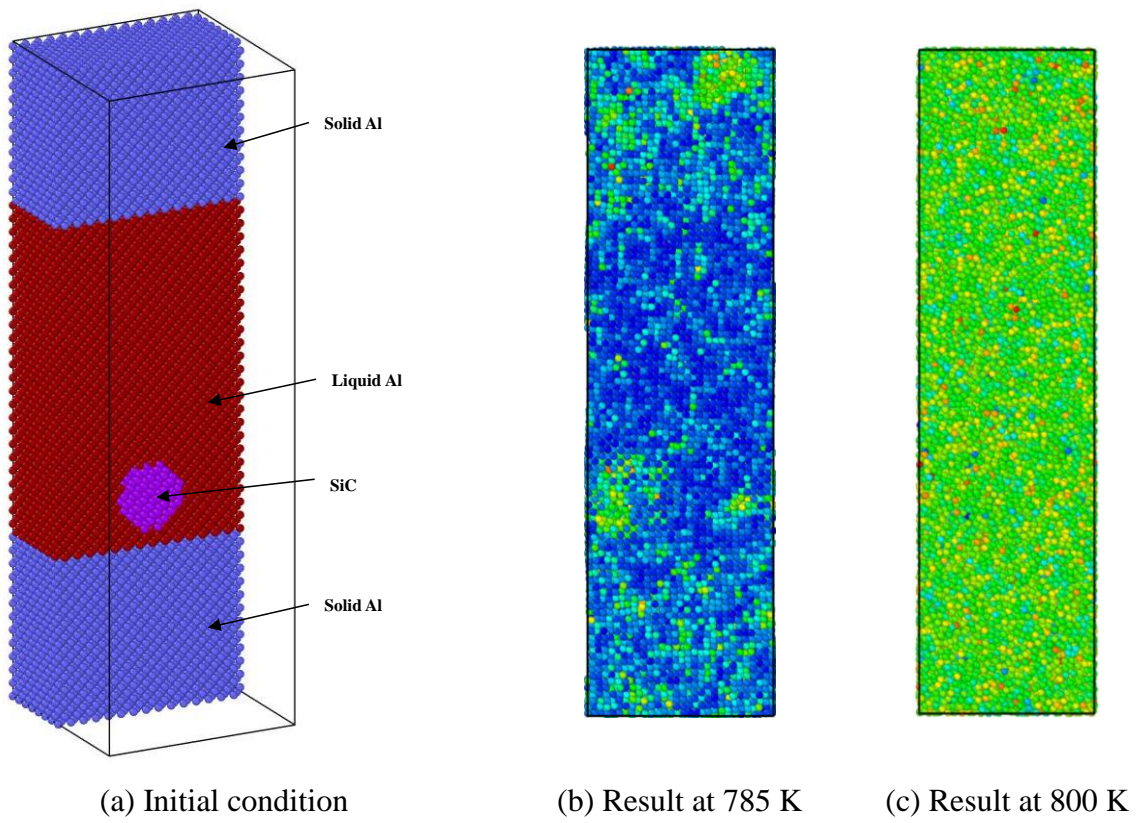


Figure 4.27 Calculation of equilibrium melting temperature

If T_m is larger than the melting temperature, the whole system will become liquid eventually (e.g. Figure 4.27(c)), otherwise, it will become solid (e.g. Figure 4.27(b)). The equilibrium melting can also be determined from the evolution of potential energy of the solid-liquid coexistence system [123].

Figure 4.28 shows evolution of potential energies of the solid-liquid coexistence system at different temperatures. It can be seen that the potential energies increase with time at temperatures above 788K, indicating that the system is melting, while the potential energies decrease with time at temperatures below 787K. Thus, the equilibrium melting temperature is estimated to be 787~788K, which is about 146K below the theoretical melting temperature of pure aluminium.

In order to eliminate the influence of the SiC particle, it is removed from the system, and the evolution of potential energies of the system at different temperatures is shown in Figure 4.29. Melting temperature obtained for pure aluminum with current EAM potential is between 789~790 K, which is about the same as before. So we can conclude that the EAM potential file from Winey [117] cannot accurately calculate the properties of the system. But it should be able to serve our purpose to predict the behaviour of the SiC during solidification.

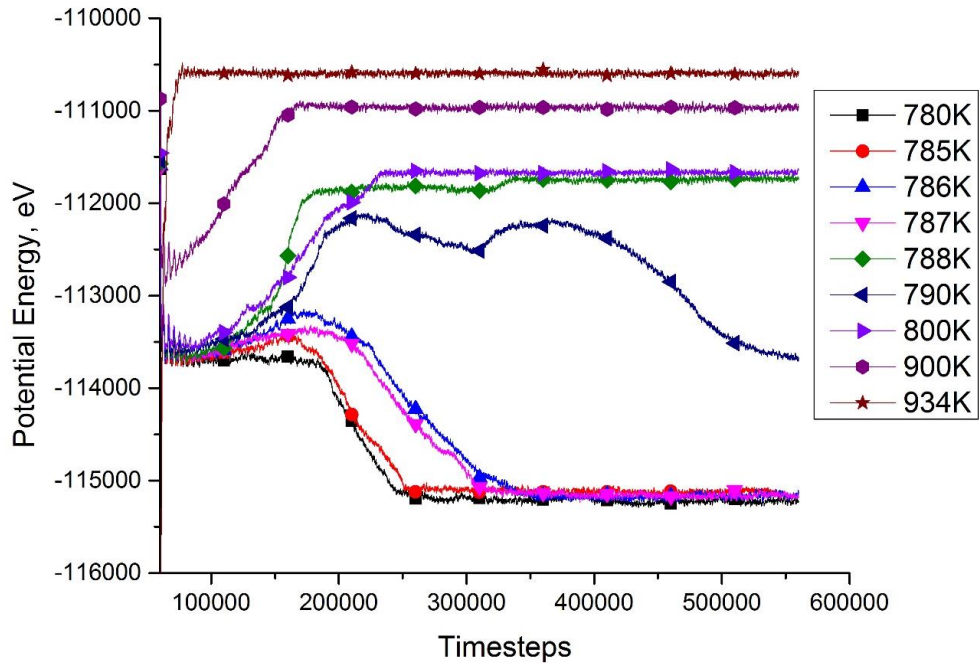


Figure 4.28 Evolution of potential energies of the system at different temperatures

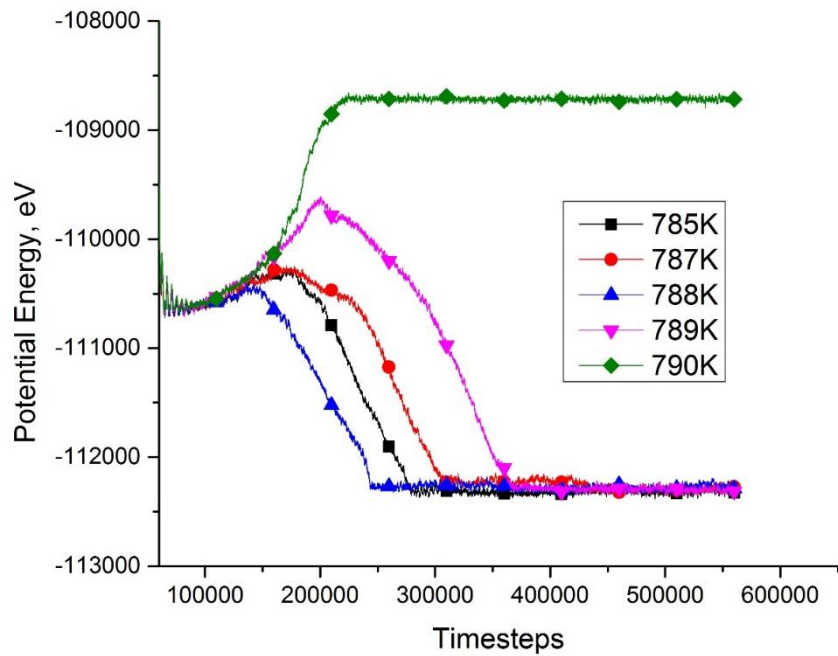


Figure 4.29 Evolution of potential energies of the system without SiC particle at different temperatures

The two phase Al system is established by holding fixed the atoms in solid Al region of the original crystalline lattice and melting the liquid Al region by raising the temperature to some temperature above the melting point. Figure 4.30 shows the solid/liquid status of the system after 10 ps and 40 ps. The whole system is equilibrated after 40ps, then the initial solid Al atoms are fixed at some temperature (500 K) below the melting point, and Si, C, and liquid Al atoms with the micro-canonical ensemble (NVE – constant atom number, volume and energy) will “release heat” through the solid atoms.

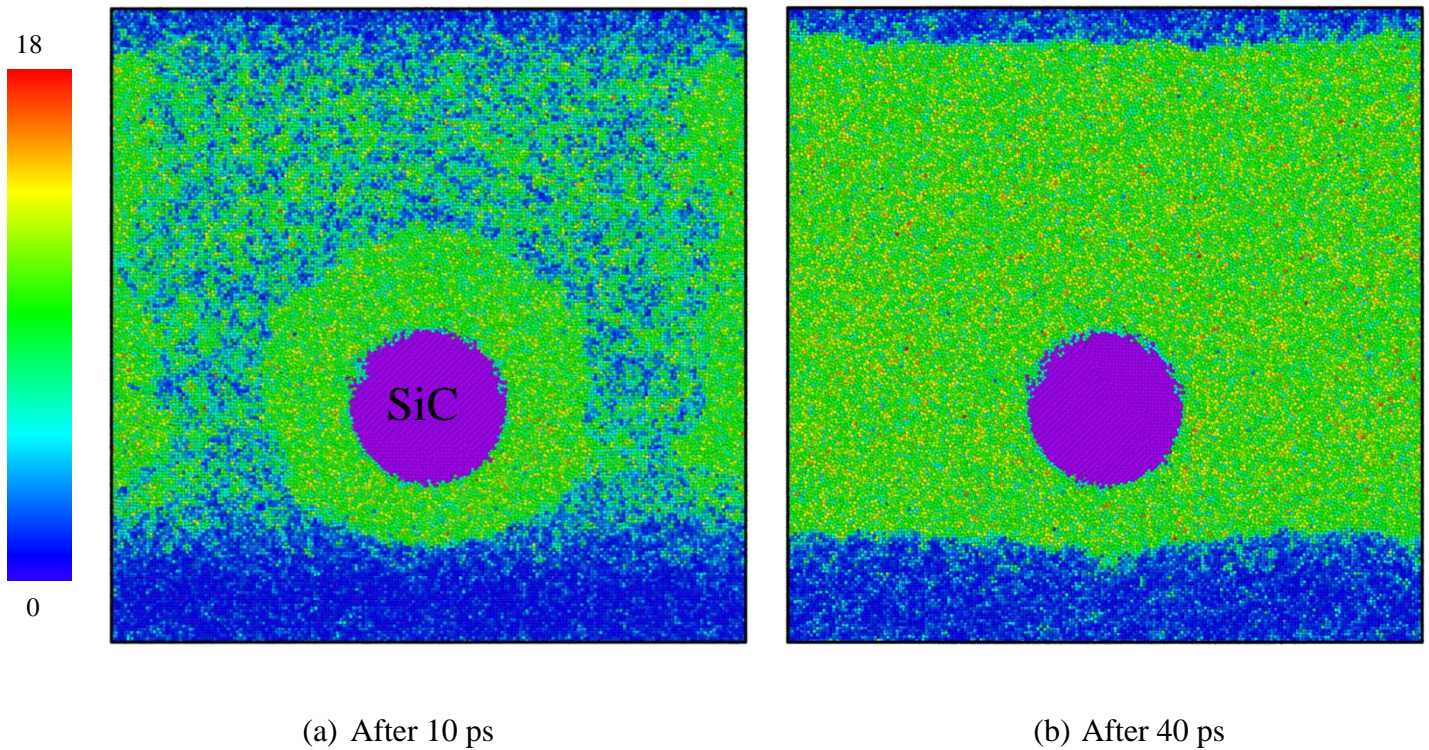
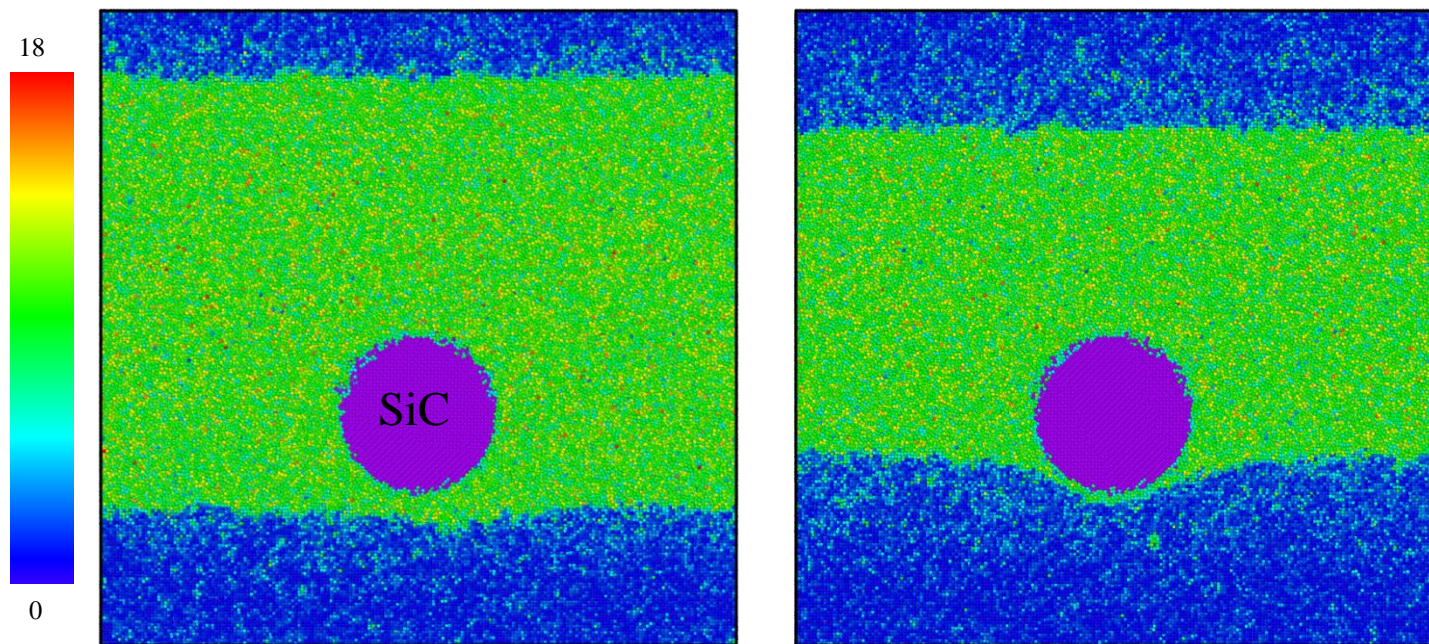


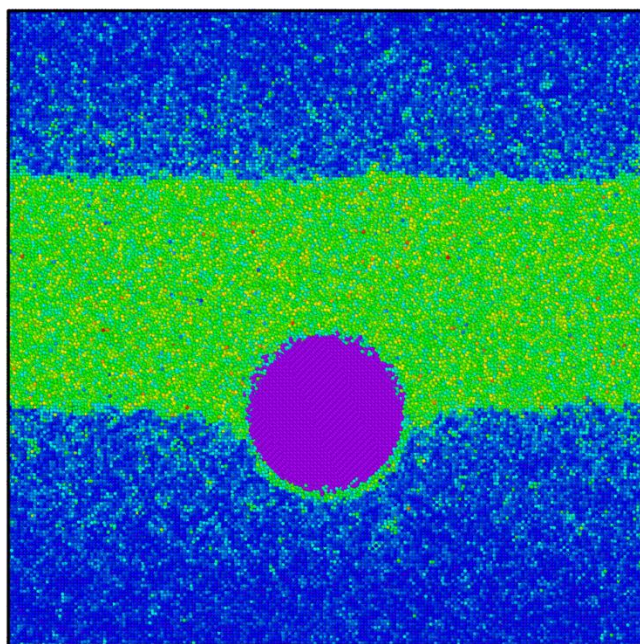
Figure 4.30 Solid/liquid status of the system after 10 ps and 40 ps

Figure 4.31 shows the solid/liquid status of the system after 100 ps, 200 ps, 300 ps, 400 ps, 500 ps, and 600 ps, respectively.

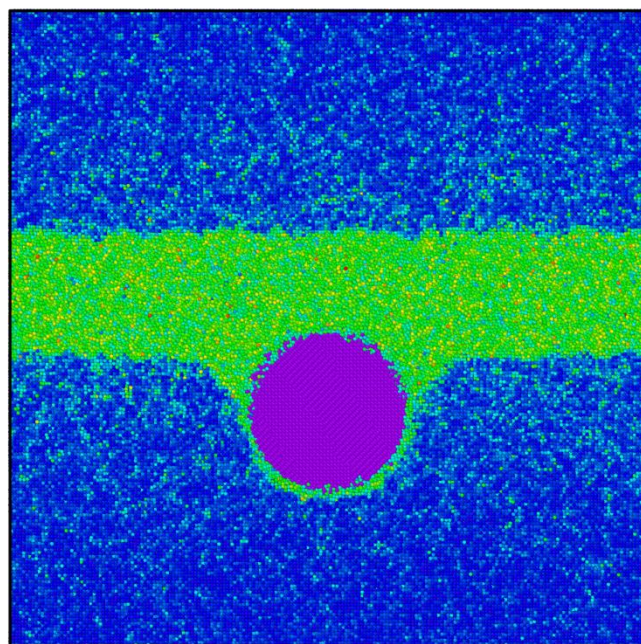


(a) After 100 ps

(b) After 200 ps



(c) After 300 ps



(d) After 400 ps

Figure 4.31 Solid/liquid status of the system after 100 ps, 200 ps, 300 ps, 400 ps, 500 ps, and 600 ps

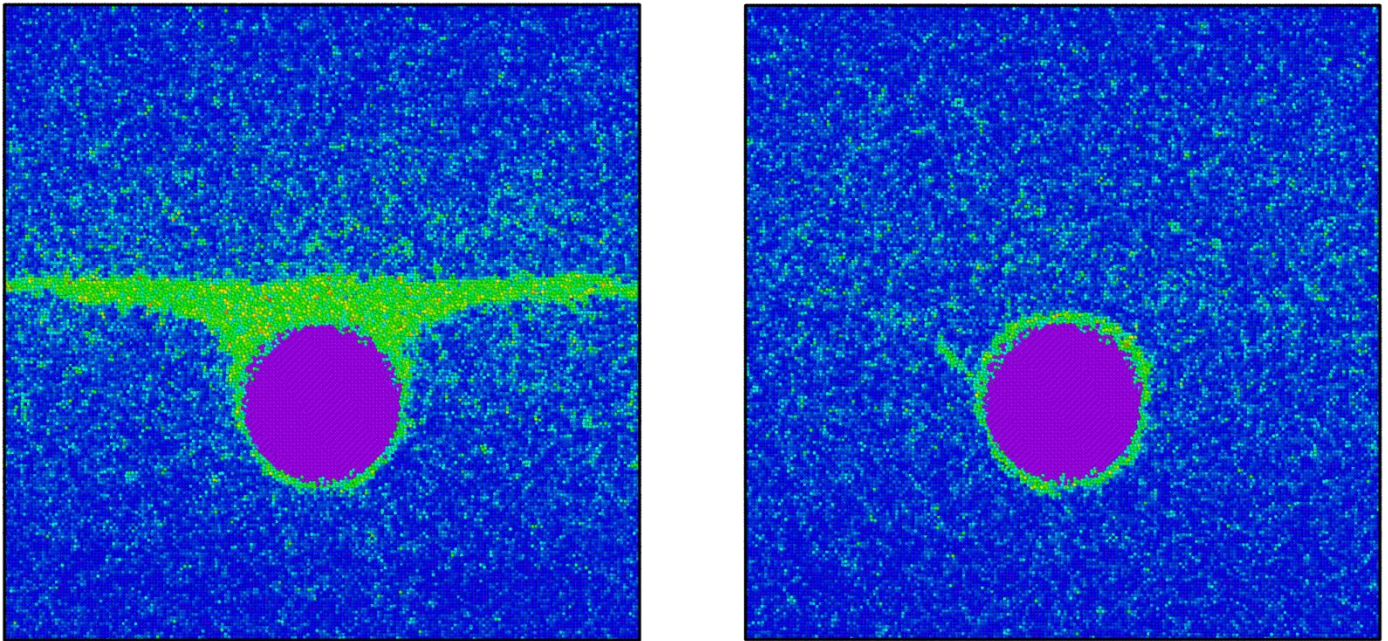


Figure 4.31 Solid/liquid status of the system after 100 ps, 200 ps, 300 ps, 400 ps, 500 ps, and 600 ps (continued)

As it can be seen from Figure 4.31(a), when the liquid/solid interfaces are far away from the SiC nanoparticle, both of the interfaces at the top and bottom are flat. When the interface at the bottom approaches the SiC nanoparticle, a trough is formed below the particle (see Figure 4.31(b)). As time goes on, the interface at the bottom passes through the particle and the interface at the top approaches the particle (See Figure 4.31(c) and Figure 4.31(d)). Finally, these two interfaces meet each other, become one, and disappear (see Figure 4.31(e) and Figure 4.31(f)).

However, we may not notice the movement of the SiC nanoparticle from Figure 4.31, because it is extremely small. Figure 4.32 plots the position of the SiC nanoparticle with time. As it can be seen, the horizontal movement (x and y) of the nanoparticle is negligible. But in z

direction (vertical), the particle moves down towards the liquid/solid interface at the bottom in the beginning, and when the interface from the top approaches it, the particle moves up towards that interface again. So it is confirmed during the solidification process, the SiC nanoparticle will be engulfed by the solidification front instead of being pushed.

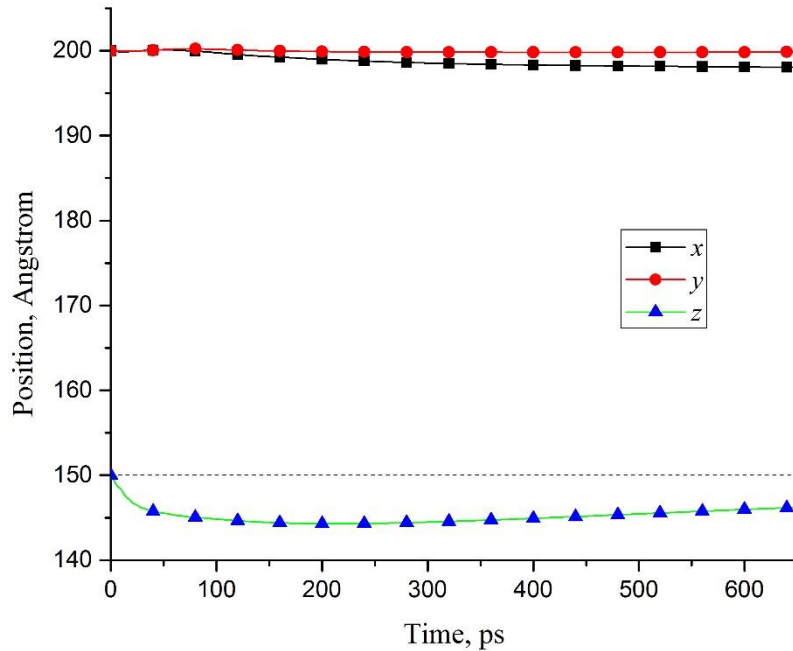


Figure 4.32 Position of SiC nanoparticle during solidification

Figure 4.33 shows the Solid/liquid status of the system with a $\Phi 20$ nm SiC nanoparticle after 100 ps, 200 ps, 300 ps, 400 ps, 500 ps, and 600 ps. When the particle size is larger, the change of the solid/liquid interfaces due to the effect of nanoparticle is even clearer, but the total solidification time stays almost the same. Figure 4.34 plots the position of a $\Phi 20$ nm SiC nanoparticle with time. As it can be seen, the general trend is basically the same as that with a smaller particle, but the maximum displacement is higher because the interaction of the SiC nanoparticle and the solid/liquid interfaces stays longer time.

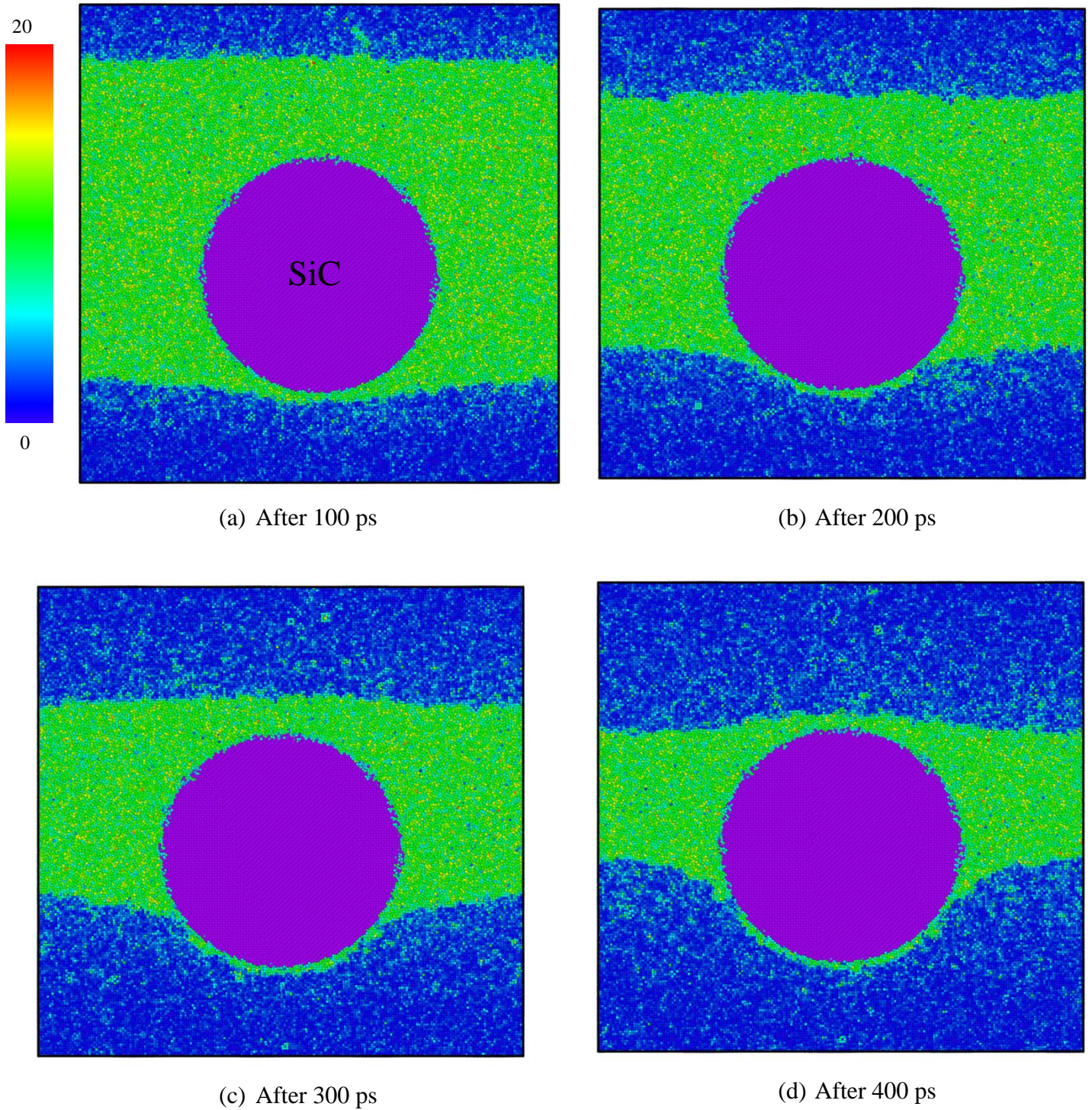


Figure 4.33 Solid/liquid status of the system with a $\Phi 20$ nm SiC nanoparticle after 100 ps, 200 ps, 300 ps, 400 ps, 500 ps, and 600 ps

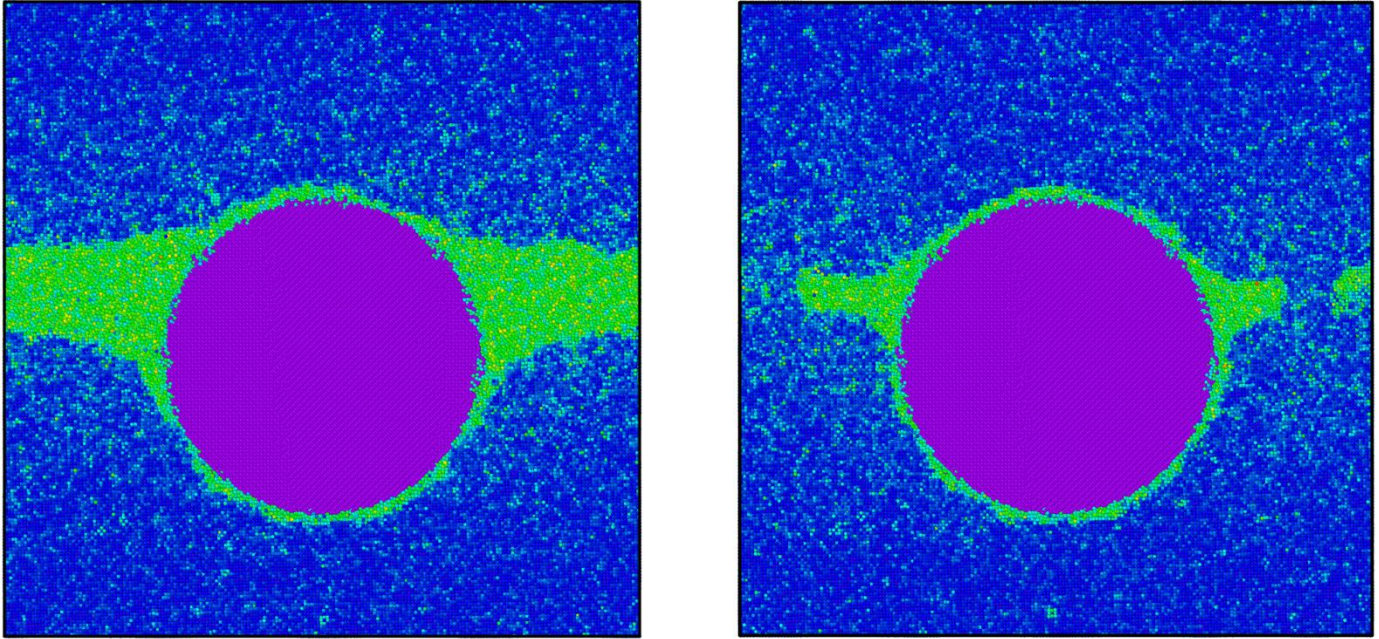


Figure 4.33 Solid/liquid status of the system with a $\Phi 20$ nm SiC nanoparticle after 100 ps, 200 ps, 300 ps, 400 ps, 500 ps, and 600 ps (continued)

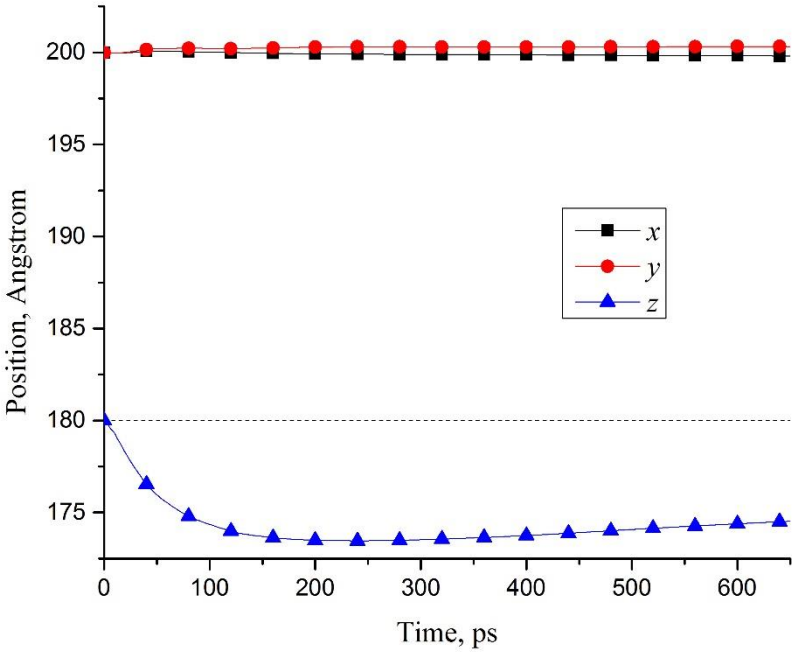


Figure 4.34 Position of a $\Phi 20$ nm SiC nanoparticle during solidification

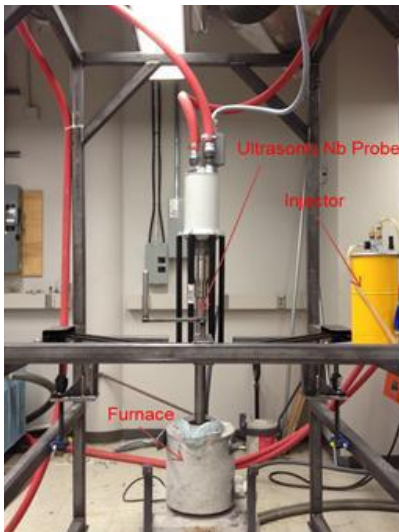
CHAPTER 5 – EXPERIMENTAL VALIDATION

5.1 Experimental Approach

Aluminum alloy A356 and 6061 are selected as the metallic matrix because they are widely used. The ceramic nanoparticles used in this study are β -SiC (spherical shape, average diameter of 55nm). The ultrasonic processing system used in this study is illustrated in Figure 5.1. It includes the generator, Nb ultrasonic probe, injector, induction furnace and ASTM B108-02 standard metal mold. The main parameters of the ultrasonic equipment are: maximum power, $P=2.4\text{kW}$ and frequency, $f=18\text{ kHz}$. An induction furnace with a capacity of 2.7 kg is used to melt the alloy. After the alloy is melted, the Nb ultrasonic probe is inserted to about 50 mm beneath the melt surface to perform ultrasonic stirring at 1.75 kW power and 18 kHz frequency. 1 wt% nanoparticles are added into the cavitation area (just beneath the ultrasonic probe) during a 15 min time-frame. The molten pool is protected by Argon gas atmosphere. A thermocouple is used to monitor the melt temperature to control the superheat. A higher pouring temperature of 750°C is used to minimize the formation of metal-mold filling defects including cold-shuts. The metal mold is preheated to 400°C . The specimen are extracted from the metal mold after 30 min and tested on a tensile test machine. The dimensions of the specimen are 50.8 mm length and 12.7 mm diameter. The experiments are repeated several times for statistical interpretation of the results.

Another set of experiments applying UST treatment during solidification are performed to better understand the effects of UST with and without nanoparticles on the solidification microstructure. The base experiment is done by melting the A356 alloy and turning off the

furnace to let the molten metal solidify. The UST experiment is done by melting the A356 alloy and turning off furnace, and then during solidification, treating the molten alloy with UST for 4 min. The UST with nanoparticles (1% SiC) experiments are performed by melting the A356 alloy, adding the nanoparticles (1% SiC) assisted by UST for 15 min, turning off furnace, and then during solidification, treating the molten alloy with UST for 4 min.



(a) Experimental setup



(b) Ultrasonic generator

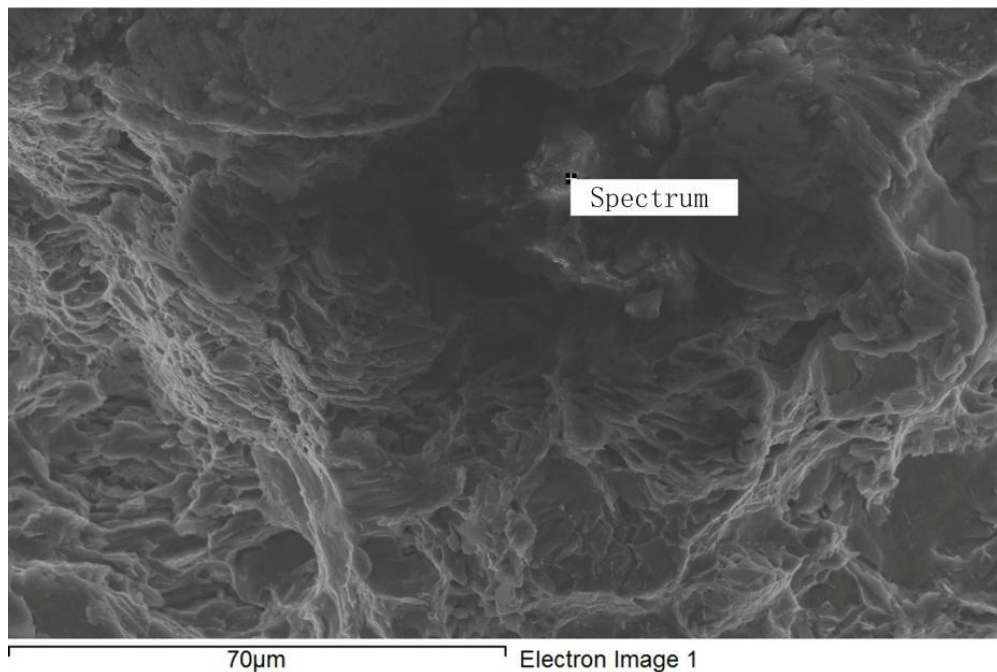


(c) ASTM B108-02 standard metal mold

Figure 5.1 UST equipments

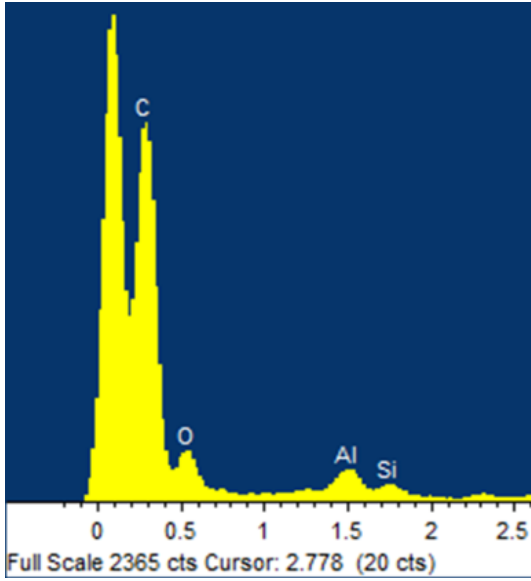
5.2 Microscopy Analysis of 6061-based with 1.0 wt.% SiC samples

Figure 5.2 shows SEM and EDS analysis of the 6061-based 1.0 wt.% SiC nanocomposites samples. Tensile fracture surface (Figure 5.2(a)) is used to find nanoparticles. Figure 5.2(b) and (c) show the EDS spectrum of elements in the 6061 nanocomposites, in which Si and C are both detected in the nanocomposite sample. The only possible source of the C showing in the EDS spectrum is from SiC nanoparticle addition.

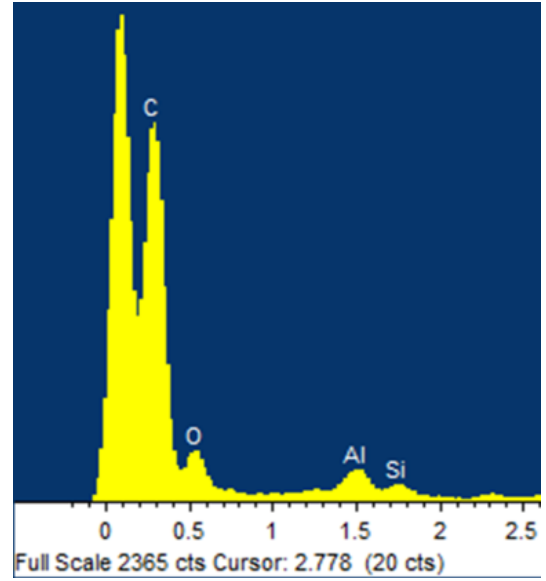


(a) SEM tensile fracture surface

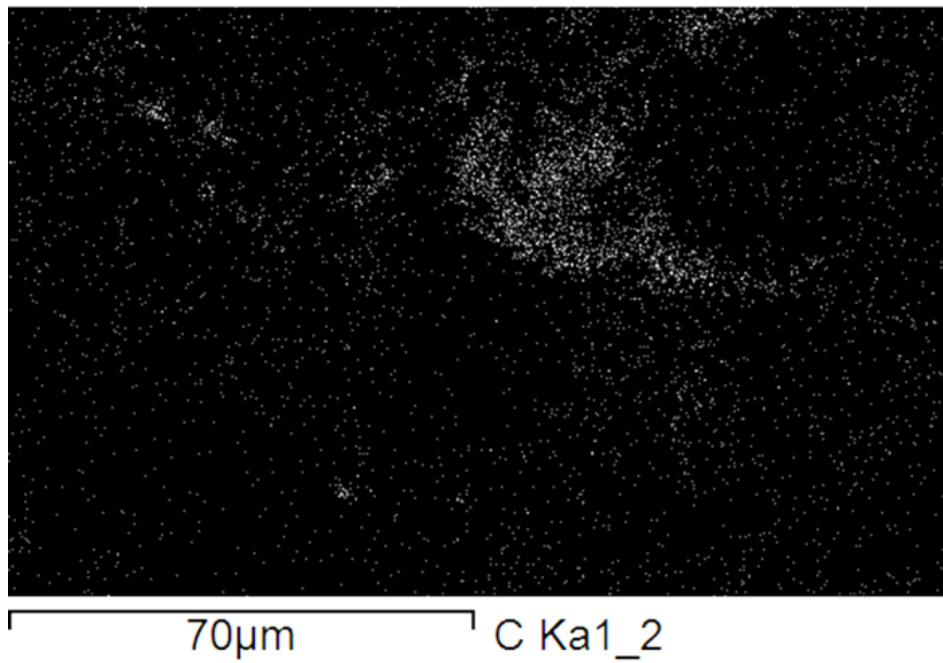
Figure 5.2 SEM and EDS analysis of the 6061-based 1.0 wt.% SiC nanocomposites [120]



(b) EDS for the spectrum position on the tensile fracture surface

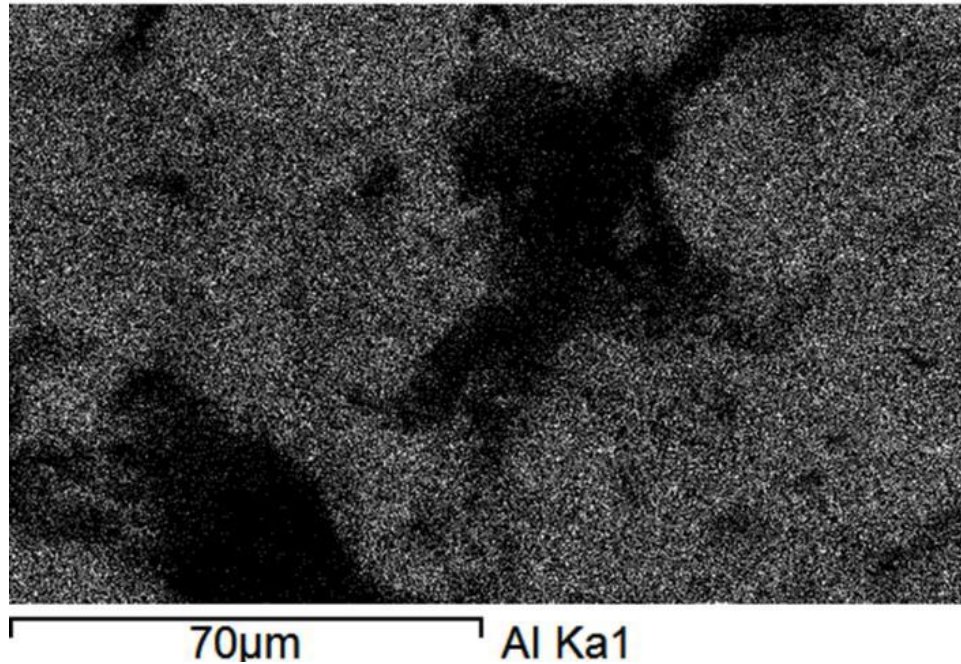


(c) EDS for the whole area on the tensile fracture surface



(d) EDS mapping result for Carbon

Figure 5.2 SEM and EDS analysis of the 6061-based 1.0 wt.% SiC nanocomposites (continued)



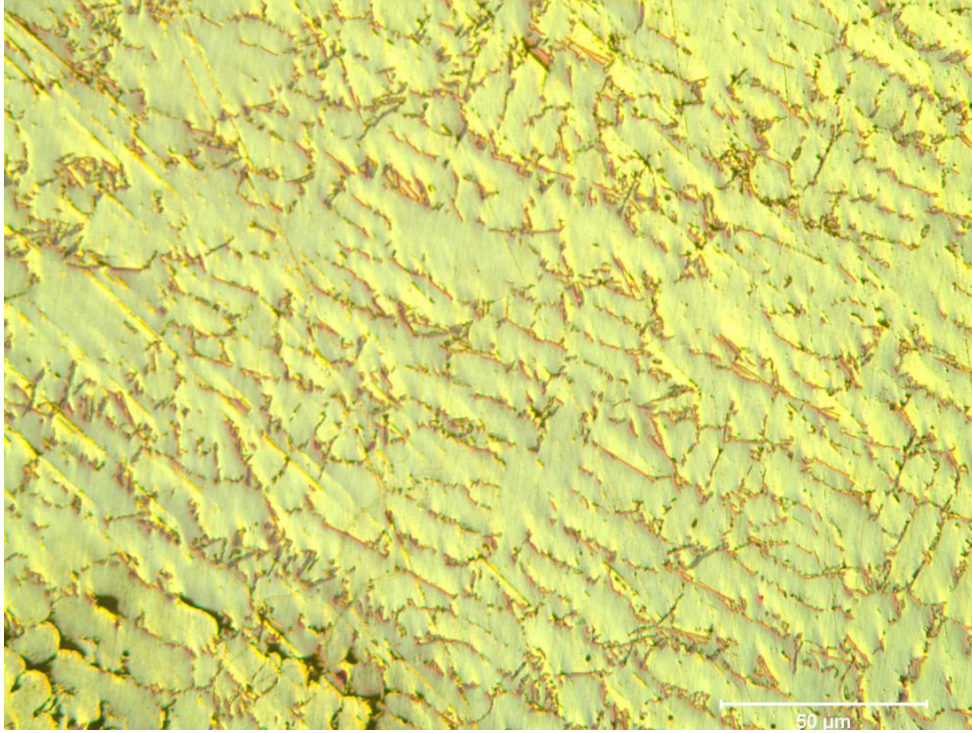
(e) EDS mapping result for Aluminum

Figure 5.2 SEM and EDS analysis of the 6061-based 1.0 wt.% SiC nanocomposites (continued)

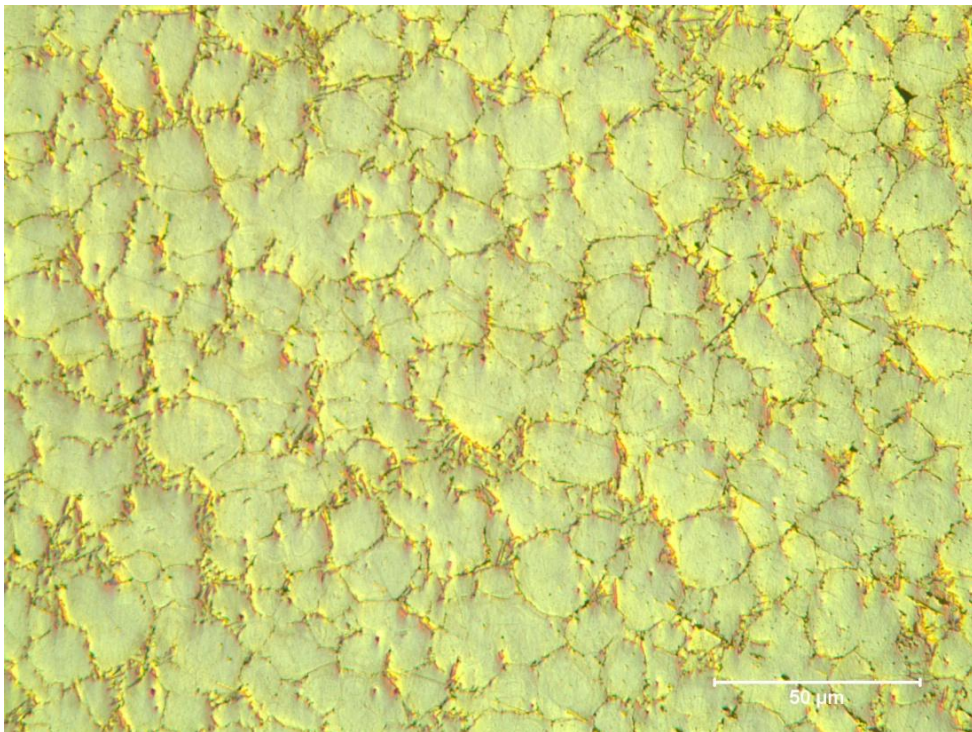
It can be seen from Figure 5.2(d) that the SiC nanoparticles are dispersed reasonably well into the 6061 matrix. However, some insignificant agglomeration can be observed as well.

5.3 Microscopy Analysis of A356-based Nanocomposites Treated during Solidification

Figure 5.3 shows the microstructures of non-UST and UST+1.0 wt.% SiC treated A356 samples. It is obvious that the samples without UST treatment and without SiC reinforcement have coarser microstructures. It can also be observed that the Si eutectic structure (black area) is more modified in the UST + SiC treated samples.



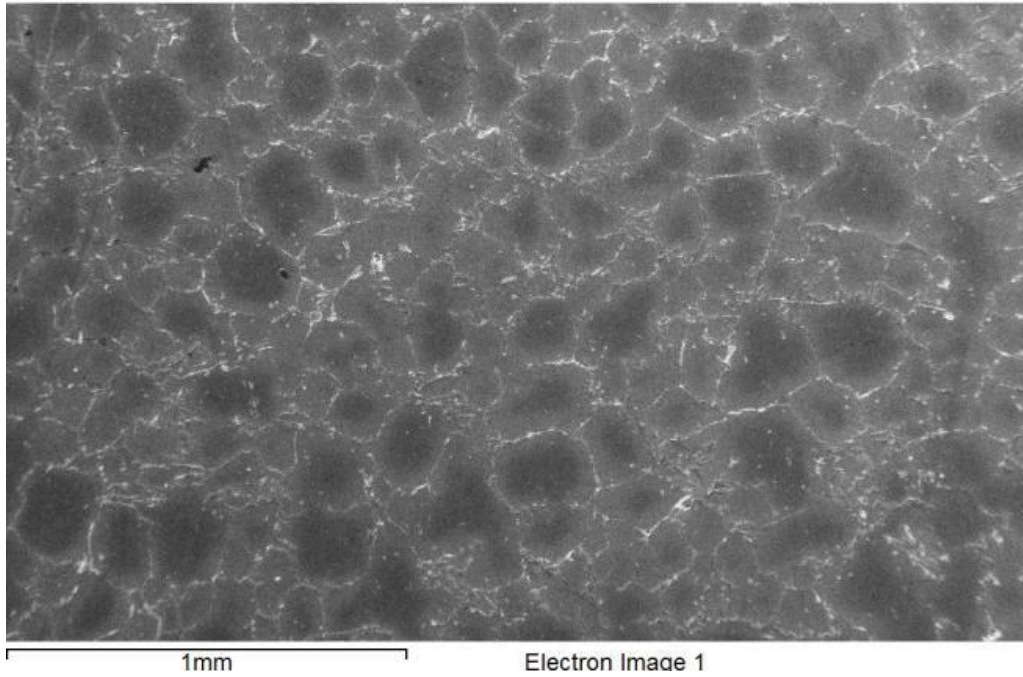
(a) Non-UST treated A356 samples



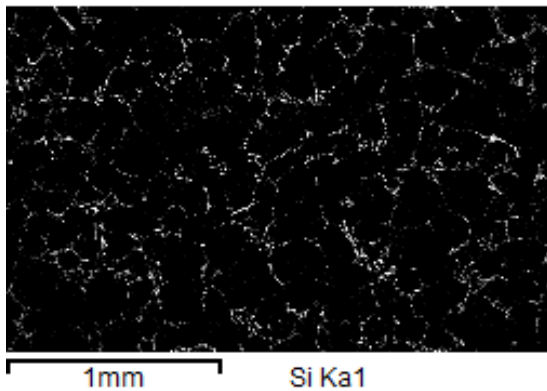
(b) UST+1.0 wt.% A356 samples

Figure 5.3 Microstructures of non-UST and UST+SiC treated A356 samples [15]

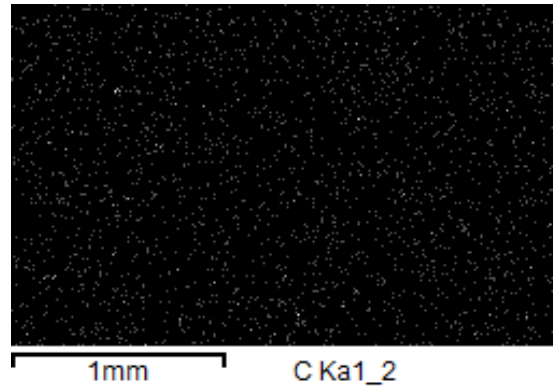
Figure 5.4 shows the SEM results at X50 magnification for UST+1% SiC treated A356 samples. It can be seen that the SiC nanoparticles are dispersed reasonably well into the A356 matrix. It also confirms the optical microscope results that grain structure is refined to achieve globular morphology.



(a) SEM pictures



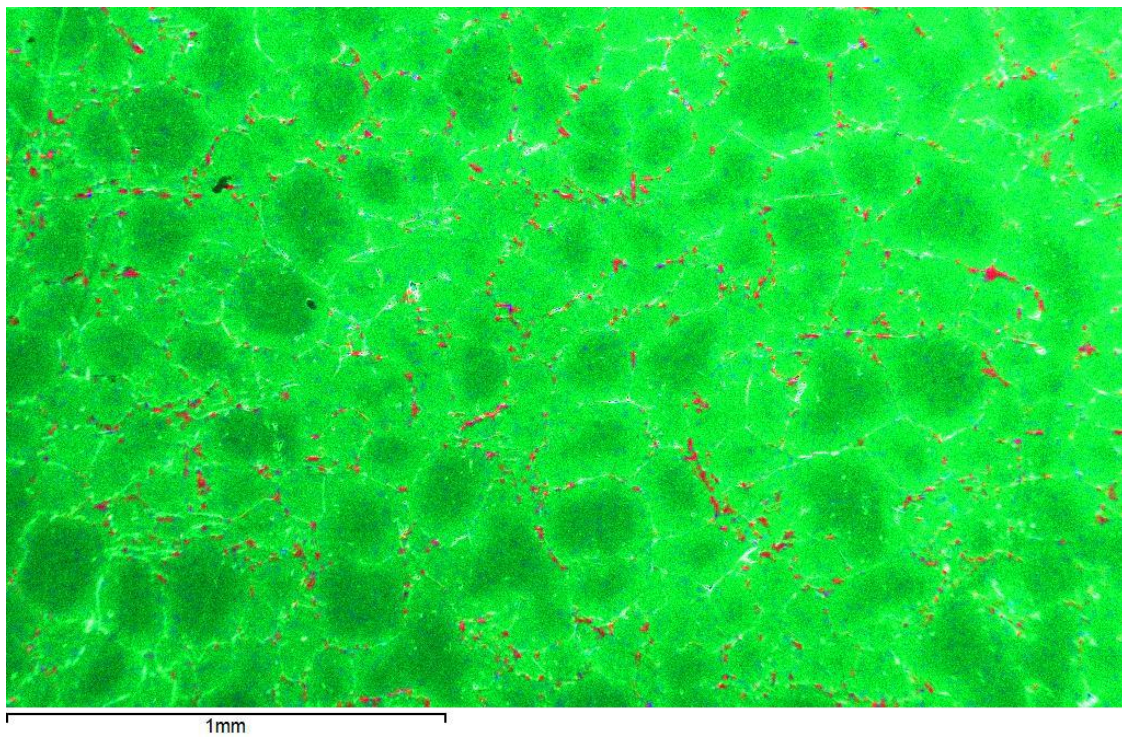
(b) EDS mapping result for Si element



(c) EDS mapping result for C element

Figure 5.4 SEM results at X50 magnification for UST+1% SiC treated A356 samples [15]

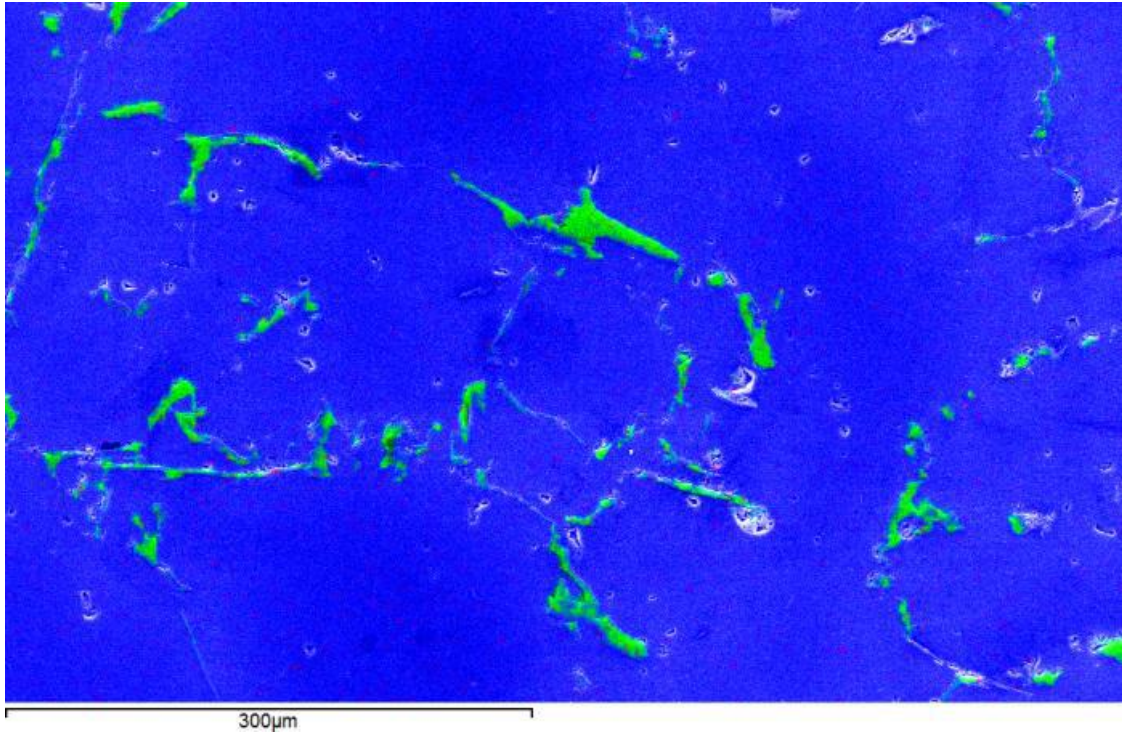
Figure 5.5 shows the EDS mapping results at different magnifications for UST+1% SiC treated A356 samples. Similar conclusion can be made that the SiC nanoparticles are dispersed reasonably well into the A356 matrix. It can also be seen that C element tends to gather around the grain boundary area where the Si eutectic phase is located. This confirms the literature result [124] about the interfaces between the SiC particles and the alloy matrix. It also reveals that the SiC particles appear to act as substrates for the nucleation of the Si phase.



(a) Al (in green), Si (in red) and C (in blue) elements at X50 magnification

Figure 5.5 EDS mapping results at different magnifications for UST+1% SiC treated samples

[125]



(b) Al (in blue), Si (in green) and C (in red) elements at X200 magnification

Figure 5.5 EDS mapping results at different magnifications for UST+1% SiC treated samples

(continued)

CHAPTER 6 – CONCLUSIONS AND FUTURE WORK

6.1 Conclusions

A comprehensive magneto-hydro-dynamics (MHD) model built with ANSYS Fluent and ANSYS Maxwell is adapted to investigate the dispersion of SiC nanoparticles into a 6061 matrix with different injection positions, flow magnitudes and gravity directions under ultrasonic stirring and unidirectional solidification processing conditions.

Dense discrete phase model (DDPM) accounting for viscous drag force, buoyancy force, gravitational force, virtual mass force, Saffman's lift force and interfacial force, associated with a particle engulfment and pushing (PEP) model is developed using Fluent UDF.

3D molecular dynamics simulations of the interatomic interactions between a SiC nanoparticle and the liquid/solid aluminum interface using hybrid potentials (EAM, Morse and Tersoff potentials) are fulfilled in LAMMPS. UA High-Performance Computing Cluster (HPCC) is employed in order to meet the requirement for large-scale computing.

The simulation results reveal the following:

- 1) The fluid flow is much stronger at the center of the furnace than that near the wall.
- 2) The fluid flow after 3.0s is almost the same as that after 1.0s because both of them are fully developed with a strong flow condition and one-way coupling.
- 3) The nanoparticles are following the fluid flow.
- 4) The nanoparticles are well dispersed after 3.0 sec into the molten alloy with a strong flow.
- 5) Relatively fewer nanoparticles stay at the center where the fluid flow is stronger, which indicates that the nanoparticles are taken away by the strong flow.

- 6) The injection position does not affect the final distribution of the nanoparticles, as long as the fully developed fluid flow is strong enough to disperse the nanoparticles throughout the furnace.
- 7) If the gravity direction is opposite to the direction of the stronger flow at the center of the furnace, it will retard the development of the flow and result in a different flow pattern for non-fully developed flow.
- 8) Fully developed fluid flow with an opposite gravity direction is almost the same as before, because the gravitational force is relatively weak compared to the drag force, if the flow is very strong.
- 9) The final distribution of nanoparticles with an opposite gravity direction looks similar as before, and the general trend is basically the same.
- 10) Fully developed flow pattern with a weaker flow is almost the same as before, except that the magnitude is much smaller.
- 11) If the fluid flow is not strong enough, the final distributions of nanoparticles are different with different injection positions.
- 12) When solidification starts, the fluid flow is damped in the mushy zone.
- 13) Some agglomerations in the solid can be observed because the nanoparticles approaching the solid/liquid interface are engulfed.
- 14) The gravity will play an important role during the solidification process when the flow is damped.
- 15) Induction stirring modifies the fluid flow to some extent, making it more uniform.
- 16) Induction stirring will play a major role on the fluid flow if the flow is weak.

- 17) The fluid flow and nanoparticle distributions during solidification don't change too much compared with the results without EMS when the fluid flow is strong.
- 18) The flat liquid/solid interface approaching the SiC nanoparticle will be changed that a trough will form around the particle.
- 19) It is confirmed that the SiC nanoparticle will be engulfed by the solidification front instead of being pushed based on the movement of the particle against the liquid/solid interface.
- 20) The displacement of the SiC nanoparticle will be even greater with a bigger particle because the duration of the interaction between the nanoparticle and solid/liquid interface is longer.

6061-based and A356-based nanocomposites reinforced with 1.0 wt.% SiC nanoparticles are fabricated, and SEM and EDS analyses are conducted to investigate the nanodispersion. The experimental results reveal the following:

- 1) The nanoparticles are dispersed reasonably well in the metal matrix, but some insignificant agglomeration still occurs.
- 2) The A356 samples without UST treatment nor SiC reinforced have coarser microstructures.
- 3) In the A356 alloy matrix, SiC nanoparticles tend to gather around grain boundary area which is mostly the Si eutectic phase.
- 4) The SiC nanoparticles may act as substrates for the nucleation of the Si phase.

6.2 Main Contributions of This Study

- 1) A detailed literature review was performed, which revealed the effects of ultrasonic technology on the molten metal and solidification processing, strengthening mechanisms for metal-matrix-nano-composites, and advanced numerical modeling of induction stirring and

particle engulfment and pushing, as well as molecular dynamics simulation of solidification processes.

- 2) A comprehensive magneto-hydro-dynamics (MHD) model was built with ANSYS Fluent and ANSYS Maxwell to investigate the dispersion of SiC nanoparticles into a 6061 matrix.
- 3) A particle engulfment and pushing model was developed to deal with ceramic nanoparticles approaching the liquid/solid interface in solidifying metallic alloys.
- 4) The influences of injection position, gravity, electromagnetic stirring and intensity of ultrasonic stirring on the dispersion of nanoparticles during molten metal and solidification processing were investigated.
- 5) The complex interactions between a SiC nanoparticle and the Al liquid/solid interface were analyzed with a 3D molecular dynamics model using LAMMPS on the High Performance Computing Cluster (HPCC) at the University of Alabama.
- 6) The assumption that ultrafine particles will be engulfed by the solidification front instead of being pushed was proved through MD simulation.
- 7) Two sets of Al-based nanocomposites were fabricated, and microscopy analyses were conducted for these samples, which confirmed that the nanoparticles were dispersed reasonably well in the metal matrix.

6.3 Recommendations for Future Work

- 1) Further improve the particle engulfment and pushing model based on the data obtained from molecular dynamics simulation.
- 2) Fully couple the nanodispersion CFD model with the ultrasonic cavitation model.
- 3) Investigate the effects of the size and mass fraction of nanoparticles.

- 4) Improve the particle engulfment and pushing model to account for dendritic structures of the alloy during solidification.
- 5) Study the effects of undercooling, solidification velocity, particle size, and particle composition on the mechanism of engulfment and pushing by molecular dynamics simulation.
- 6) Develop a numerical strengthening model to account for all the possible strengthening mechanisms.
- 7) Conduct the scanning transmission electron microscopy (STEM) analysis of the as-cast 6061/A356 nanocomposites to better understand the effects of the ultrasonic cavitation processing on the dispersion of the nanoparticles and the interaction between the metal matrix and the nanoparticles.
- 8) Investigate the influence of ultrasonic cavitation and acoustic streaming on the microstructure evolution of alloys under both high and low superheat conditions.

REFERENCES

- [1] J.W. Kaczmar, K. Pietrzak, W. Włosiński. The production and application of metal matrix composite materials, *Journal of Materials Processing Technology* 106 (2000) 58-67.
- [2] K. Ďurišínová, J. Ďurišin, M. Orolínová, M. Ďurišin. Effect of particle additions on microstructure evolution of aluminium matrix composite, *Journal of Alloys and Compounds* 525 (2012) 137-142.
- [3] W.C. Harrigan Jr. Commercial processing of metal matrix composites, *Materials Science and Engineering: A* 244 (1998) 75-79.
- [4] D. Zhang, L. Nastac. Numerical modeling of the dispersion of ceramic nanoparticles during ultrasonic processing of aluminum-based nanocomposites, *Journal of Materials Research and Technology* 3 (2014) 296-302.
- [5] Y. Yang, J. Lan, X. Li. Study on bulk aluminum matrix nano-composite fabricated by ultrasonic dispersion of nano-sized SiC particles in molten aluminum alloy, *Materials Science and Engineering: A* 380 (2004) 378-383.
- [6] G. Cao, H. Konishi, X. Li. Mechanical properties and microstructure of SiC-reinforced Mg-(2,4)Al-1Si nanocomposites fabricated by ultrasonic cavitation based solidification processing, *Materials Science and Engineering: A* 486 (2008) 357-362.
- [7] J. Shin, H. Choi, M. Cho, D. Bae. Effect of the interface layer on the mechanical behavior of TiO₂ nanoparticle reinforced aluminum matrix composites, *Journal of Composite Materials* 48 (2014) 99-106.
- [8] B. Dikici, M. Gavali, F. Bedir. Synthesis of in situ TiC nanoparticles in liquid aluminum: the effect of sintering temperature, *Journal of Composite Materials* (2011) 895-900.
- [9] A.A. El-Daly, M. Abdelhameed, M. Hashish, W.M. Daoush. Fabrication of silicon carbide reinforced aluminum matrix nanocomposites and characterization of its mechanical properties using non-destructive technique, *Materials Science and Engineering: A* 559 (2013) 384-393.
- [10] X. Jiang, M. Galano, F. Audebert. Extrusion textures in Al, 6061 alloy and 6061/SiCp nanocomposites, *Materials Characterization* 88 (2014) 111-118.
- [11] J.H. Shin, D.H. Bae. Effect of the TiO₂ nanoparticle size on the decomposition behaviors in aluminum matrix composites, *Materials Chemistry and Physics* 143 (2014) 1423-1430.

- [12] C. Borgohain, K. Acharyya, S. Sarma, K. Senapati, K.C. Sarma, P. Phukan. A new aluminum-based metal matrix composite reinforced with cobalt ferrite magnetic nanoparticle, *J Mater Sci* 48 (2013) 162-171.
- [13] F.K. Sautter. Electrodeposition of Dispersion - Hardened Nickel - Al₂O₃ Alloys, *Journal of The Electrochemical Society* 110 (1963) 557-560.
- [14] D. Zhang, L. Nastac. Numerical Modeling of the Dispersion of Ceramic Nanoparticles during Ultrasonic Processing of A356 - Based Nanocomposites. *Advances in the Science and Engineering of Casting Solidification: An MPMD Symposium Honoring Doru Michael Stefanescu*: Wiley Online Library, 2015. p.37-47.
- [15] S. Jia, D. Zhang, Y. Xuan, L. Nastac. An experimental and modeling investigation of aluminum-based alloys and nanocomposites processed by ultrasonic cavitation processing, *Applied Acoustics* 103 (2016) 226-231.
- [16] D. Zhang, L. Nastac. Advanced Numerical Modeling of the Dispersion of Ceramic Nanoparticles during Ultrasonic Cavitation Processing and Solidification of 6061-based Nanocomposites. *IOP Conference Series: Materials Science and Engineering*, vol. 84: IOP Publishing, 2015. p.012020.
- [17] M. Mach, P. Karban, I. Doležel, D. Trutwin. Stirring of Liquid Steel in Crucible Induction Furnace. *International Scientific Colloquium. Riga*. p.203-208.
- [18] R. Schwarze, F. Obermeier. Modelling of unsteady electromagnetically driven recirculating melt flows, *Modelling and simulation in materials science and engineering* 12 (2004) 985.
- [19] S. Naher, D. Brabazon, L. Looney. Computational and experimental analysis of particulate distribution during Al-SiC MMC fabrication, *Composites Part A: Applied Science and Manufacturing* 38 (2007) 719-729.
- [20] D. Stefanescu, B. Dhindaw, S. Kacar, A. Moitra. Behavior of ceramic particles at the solid-liquid metal interface in metal matrix composites, *Metallurgical Transactions A* 19 (1988) 2847-2855.
- [21] U.G. Wegst, M. Schecter, A.E. Donius, P.M. Hunger. Biomaterials by freeze casting, *Philosophical Transactions of the Royal Society of London A: Mathematical, Physical and Engineering Sciences* 368 (2010) 2099-2121.
- [22] S. Plimpton. Fast parallel algorithms for short-range molecular dynamics, *Journal of computational physics* 117 (1995) 1-19. <http://lammps.sandia.gov>.
- [23] L. Nastac. Mathematical Modeling of the Solidification Structure Evolution in the Presence of Ultrasonic Stirring, *Metall and Materi Trans B* 42 (2011) 1297-1305.

- [24] X. Li, Y. Yang, D. Weiss. Theoretical and experimental study on ultrasonic dispersion of nanoparticles for strengthening cast Aluminum Alloy A356, *Metallurgical Science and Technology* 26 (2013).
- [25] J.B. Ferguson, B. Schultz, P. Rohatgi, C.-S. Kim. Impact of Brownian motion on the particle settling in molten metals, *Met. Mater. Int.* 20 (2014) 747-755.
- [26] J.B. Ferguson, B.F. Schultz, P.K. Rohatgi, C.S. Kim. Brownian Motion Effects on the Particle Settling and Its Application to Solidification Front in Metal Matrix Composites. *Light Metals 2014*. John Wiley & Sons, Inc., 2014. pp. 1383-1388.
- [27] K. Meena, A. Manna, S. Banwait. An Analysis of Mechanical Properties of the Developed Al/SiC-MMC's, *American Journal of Mechanical Engineering* 1 (2013) 14-19.
- [28] J. Yan, Z. Xu, L. Shi, X. Ma, S. Yang. Ultrasonic assisted fabrication of particle reinforced bonds joining aluminum metal matrix composites, *Materials & Design* 32 (2011) 343-347.
- [29] X. Jian, H. Xu, T.T. Meek, Q. Han. Effect of power ultrasound on solidification of aluminum A356 alloy, *Materials Letters* 59 (2005) 190-193.
- [30] G.I. Eskin. Effect of ultrasonic (cavitation) treatment of the melt on the microstructure evolution during solidification of aluminum alloy ingots, *Zeitschrift für Metallkunde* 93 (2002) 502-507.
- [31] H. Xu, X. Jian, T.T. Meek, Q. Han. Degassing of Molten Aluminum A356 Alloy Using Ultrasonic Vibration, *Materials Letters* 58 (2004) 3669–3673.
- [32] Y. Han, K. Li, J. Wang, D. Shu, B. and Sun. Influence of high-intensity ultrasound on grain refining performance of Al-5Ti-1B master alloy on aluminium, *Materials Science and Engineering A* 405 (2005) 306-312.
- [33] W. Khalifa, Y. Tsunekawa, M. Okumiya. Effect of ultrasonic melt treatment on microstructure of A356 aluminium cast alloys, *Int. J. Cast. Metals Res.* 21 (2008) 129-134.
- [34] T.T. Meek, X. Jian, H. Xu, Q. Han. *Ultrasonic processing of materials*. vol. ORNL/TM-2005/125. Washington DC, USA: US Department of Energy, 2006.
- [35] B.E.a.N. Noltingk, E.A. Cavitation produced by ultrasonics., *Proc. Phys. Soc., London* 63B, (1950) 674--685.
- [36] A. Prosperetti. Bubble phenomena in sound fields: part one and part two., *Ultrasonics* 22 (1984) 69--77 and 115--124.
- [37] C.E. Brennen. *Cavitation and Bubble Dynamics*, Oxford University Press, 1995.
- [38] G.I. Eskin. *Ultrasonic Treatment of Light Alloy Melts*, Gordon & Breach, Amsterdam, 1998.

- [39] V.O. Abramov, O.V. Abramov, F. Sommer, D. Orlov. Properties of Al-Pb base alloys applying electromagnetic forces and ultrasonic vibration during casting, *Materials Letters* 23 (1995) 17-20.
- [40] V. Abramov, O. Abramov, V. Bulgakov, F. Sommer. Solidification of aluminium alloys under ultrasonic irradiation using water-cooled resonator, *Materials Letters* 37 (1998) 27-34.
- [41] G. I. Eskin. Broad prospects for commercial application of the ultrasonic (cavitation) melt treatment of light alloys,, *Ultrasonics Sonochemistry* 8 (2001) 319–325.
- [42] G.I. Eskin. *Ultrasonics Sonochemistry*, 1 (1994) S59.
- [43] G.I. Eskin. *Ultrasonics Sonochemistry*, 8 (2001) S319.
- [44] T.T. Meek, Han, Q., *Ultrasonic Processing of Materials.*, U.S. Department of Energy, USA, (accessed 9.01.10.) (2006). *Ultrasonic Processing of Materials*.
- [45] G.I. Eskin. Principles of Ultrasonic Treatment: Application for Light Alloys Melts, *Advanced Performance Materials* 4 (1997) 223-232.
- [46] S.L. Hem. The Effect of Ultrasonic Vibrations on Crystallization Processes, *Ultrasonics* 5 (1967) 202-207.
- [47] E.A.a.N. Neppiras, B.E. Cavitation produced by ultrasonics: theoretical conditions for the onset of cavitation., *Proc. Phys. Soc., London* 64B (1951) 1032--1038.
- [48] G.I. Eskin. Influence of cavitation treatment of melts on the processes of nucleation and growth of crystals during solidification of ingots and castings from light alloys, *Ultrasonics Sonochemistry* 1 (1994) S59-S56.
- [49] J. Lee, Kentish, S., Matula, T.J. and Ashokkumar, M. Effect of surfactants on inertial cavitation activity in a pulsed acoustic field, *Journal of Physical Chemistry B* 109 (2005) 16860-16865.
- [50] O.V. Abramov. *Ultrasound in Liquid and Solid Metals*, CRC Press, Boca Raton, 1994.
- [51] L. Zhang. *ultrasonic processing of aluminum alloys*, Delft University of Technology, 2013.
- [52] G.I. Eskin, D.G. Eskin. Effects of ultrasonic (cavitation) melt processing on the structure refinement and property improvement of cast and worked aluminium alloys, *Materials Science Forum* 396-402 (2002) 77-82.
- [53] T.V. Atamanenko, D.G. Eskin, L. Katgerman. Influence of ultrasonic melt treatment on structure formation in aluminium alloys with high amount of transition metals, 2009.
- [54] K.S. Suslick, Y. Didenko, M.M. Fang, T. Hyeon, K.J. Kolbeck, W.B. McNamara, M.M. Mdeleleni, M. Wong. Acoustic cavitation and its chemical consequences, *Philosophical*

Transactions of the Royal Society of London. Series A: Mathematical, Physical and Engineering Sciences 357 (1999) 335-353.

[55] D. M. Herlach, K. Eckler, A. Karma, M. Schwarz. Grain Refinement Through Fragmentation of Dendrites in Undercooled Melts, *Materials Science and Engineering A* 304-306 (2001) 20-25.

[56] H. Yasuda, N. Nakatsuka, T. Nagira, A. Sugiyama, M. Yoshiya, K. Uesugi, K. Umetani. X-ray imaging study on grain refinement due to dendrite fragmentation, *Proc. 6th Electromagnetic Processing of Materials* (2009) 257-260.

[57] M. Li, G. Yang, Y. Zhou. Direct observation of fragments of primary dendrite from undercooled Fe-Co alloys, *Journal of Crystal Growth* 204 (1999) 413-417.

[58] H. Yasuda, Y. Yamamoto, N. Nakatsuka, T. Nagira, M. Yoshiya, A. Sugiyama, I. Ohnaka, K. Umetani, K. Uesugi. In Situ Observation of Nucleation, Fragmentation and Microstructure Evolution In Sn-Bi And Al-Cu Alloys, *International Journal of Cast Metals Research* 21 (2008) 125-128.

[59] D. Ruvalcaba, R.H. Mathiesen, D.G. Eskin, L. Arnberg, L. Katgerman. In Situ Observation of Dendritic Fragmentation Due to Local Solute-Enrichment during Directional Solidification of an Aluminum Alloy, *Acta Materialia* 55 (2007) 4287-4292.

[60] M. Gupta, L. Lu, M.O. Lai, K.H. Lee. Microstructure and mechanical properties of elemental and reinforced magnesium synthesized using a fluxless liquid-phase process, *Materials Research Bulletin* 34 (1999) 1201-1214.

[61] S. Seshan, M. Jayamathy, S.V. Kailas, T.S. Srivatsan. The tensile behavior of two magnesium alloys reinforced with silicon carbide particulates, *Materials Science and Engineering A* 363 (2003) 345-351.

[62] Z. Zhang, D. Chen. Contribution of Orowan strengthening effect in particulate-reinforced metal matrix nanocomposites, *Materials Science and Engineering: A* 483 (2008) 148-152.

[63] A. Sanaty-Zadeh. Comparison between current models for the strength of particulate-reinforced metal matrix nanocomposites with emphasis on consideration of Hall-Petch effect, *Materials Science and Engineering: A* 531 (2012) 112-118.

[64] P. Luo, D. McDonald, W. Xu, S. Palanisamy, M. Dargusch, K. Xia. A modified Hall-Petch relationship in ultrafine-grained titanium recycled from chips by equal channel angular pressing, *Scripta Materialia* 66 (2012) 785-788.

[65] V. Nardone, K. Prewo. On the strength of discontinuous silicon carbide reinforced aluminum composites, *Scripta Metallurgica* 20 (1986) 43-48.

[66] J. Szekely, K. Nakanishi. Stirring and its effects on aluminum deoxidation in the ASEA-SKF furnace: Part II. Mathematical representation of the turbulent flow field and of tracer dispersion, *MTB* 6 (1975) 245-256.

- [67] N. El-Kaddah, J. Szekely, G. Carlsson. Fluid flow and mass transfer in an inductively stirred four-ton melt of molten steel: A comparison of measurements and predictions, *MTB 15* (1984) 633-640.
- [68] W.-S. Kim, J.-K. Yoon, O.-K. Eun, N.-C. Whang. A Numerical Prediction of Electromagnetically Driven Flow in ASES-SKF Ladle Refining by Straight Induction Stirrer. *IISC. The Sixth International Iron and Steel Congress.*, vol. 4, 1990. p.354-361.
- [69] M. Pal. Modeling of induction stirred ladles. Doctoral dissertation. Stockholm, Sweden: Royal Institute of Technology, 2012.
- [70] J. Alexis, P.G. Jönsson, L. Jonsson. A model of an induction-stirred ladle accounting for slag and surface deformation, *ISIJ international* 39 (1999) 772-778.
- [71] J. Alexis, P. Jönsson, L. Jonsson. Heating and electromagnetic stirring in a ladle furnace—a simulation model, *ISIJ international* 40 (2000) 1098-1104.
- [72] E. Baake, A. Umbrashko, B. Nacke, A. Jakovics. Simulation of turbulent metal flows, *GAMM - Mitteilungen* 30 (2007) 133-148.
- [73] A. Jakovics, S. Pavlovs, M. Kirpo, E. Baake. Long-term LES study of turbulent heat and mass exchange in induction channel furnaces with various channel design. *Proc. of International PAMIR Conference on Fundamental and Applied MHD*, 2011. p.5-9.
- [74] G. Poole, N. El-Kaddah. An Improved Model for the Flow in an Electromagnetically Stirred Melt during Solidification, *Metall and Materi Trans B* 44 (2013) 1531-1540.
- [75] G. Poole, M. Heyen, L. Nastac, N. El-Kaddah. Numerical Modeling of Macrosegregation in Binary Alloys Solidifying in the Presence of Electromagnetic Stirring, *Metall and Materi Trans B* 45 (2014) 1834-1841.
- [76] D.R. Uhlmann, B. Chalmers, K. Jackson. Interaction Between Particles and a Solid - Liquid Interface, *Journal of Applied Physics* 35 (1964) 2986-2993.
- [77] A. Chernov, D. Temkin, A. Mel'nikova. Theory of the capture of solid inclusions during the growth of crystals from the melt, *Sov. Phys. Crystallogr* 21 (1976) 369-373.
- [78] A. Chernov, D. Temkin, A. Mel'nikova. The influence of the thermal conductivity of a macroparticle on its capture by a crystal growing from a melt, *Sov. Phys. Crystallogr* 22 (1977) 656-658.
- [79] Y.M. Youssef, R.J. Dashwood, P.D. Lee. Effect of clustering on particle pushing and solidification behaviour in TiB₂ reinforced aluminium PMMCs, *Composites Part A: Applied Science and Manufacturing* 36 (2005) 747-763.
- [80] S.N. Omenyi, A.W. Neumann. Thermodynamic aspects of particle engulfment by solidifying melts, *Journal of Applied Physics* 47 (1976) 3956-3962.

- [81] D. Shangguan, S. Ahuja, D.M. Stefanescu. An analytical model for the interaction between an insoluble particle and an advancing solid/liquid interface, *Metallurgical Transactions A* 23 (1992) 669-680.
- [82] D.M. Stefanescu, F.R. Juretzko, A. Catalina, B.K. Dhindaw, S. Sen, P.A. Curreli. Particle engulfment and pushing by solidifying interfaces: Part II. Microgravity experiments and theoretical analysis, *Metall and Mat Trans A* 29 (1998) 1697-1706.
- [83] D. Stefanescu, A. Moitra, A.S. Kacar, B. Dhindaw. The influence of buoyant forces and volume fraction of particles on the particle pushing/entrapment transition during directional solidification of Al/SiC and Al/graphite composites, *Metallurgical Transactions A* 21 (1990) 231-239.
- [84] L. Hadji, A.M.J. Davis. The influence of insoluble spherical particles on the stability of a planar solidifying interface, *Journal of Crystal Growth* 191 (1998) 889-896.
- [85] L. Hadji. Morphological instability induced by the interaction of a particle with a solid-liquid interface, *Eur. Phys. J. B* 37 (2004) 85-89.
- [86] B.J. Alder, T.E. Wainwright. Studies in Molecular Dynamics. I. General Method, *The Journal of chemical physics* 31 (1959) 459-466.
- [87] M.S. Daw, M.I. Baskes. Embedded-atom method: Derivation and application to impurities, surfaces, and other defects in metals, *Physical Review B* 29 (1984) 6443-6453.
- [88] A. Oluwajobi, X. Chen. The effect of interatomic potentials on the molecular dynamics simulation of nanometric machining, *International Journal of Automation and Computing* 8 (2011) 326-332.
- [89] H. Yang, Y. Lü, M. Chen, Z. Guo. A molecular dynamics study on melting point and specific heat of Ni3Al alloy, *Science in China Series G: Physics, Mechanics and Astronomy* 50 (2007) 407-413.
- [90] J. Tersoff. Modeling solid-state chemistry: Interatomic potentials for multicomponent systems, *Physical Review B* 39 (1989) 5566-5568.
- [91] J. Tersoff. Carbon defects and defect reactions in silicon, *Physical Review Letters* 64 (1990) 1757-1760.
- [92] M. Tang, S. Yip. Atomistic simulation of thermomechanical properties of β -SiC, *Physical Review B* 52 (1995) 15150-15159.
- [93] X. Luo, G. Qian, W. Fei, E. Wang, C. Chen. Systematic study of β -SiC surface structures by molecular-dynamics simulations, *Physical Review B* 57 (1998) 9234-9240.
- [94] W. Yan, T. Gao, X. Guo, Y. Qin, Q. Xie. Structural Properties of Liquid SiC during Rapid Solidification, *The Scientific World Journal* 2013 (2013).

- [95] H. Zhao, N. Chen. An inverse adhesion problem for extracting interfacial pair potentials for the Al (0 0 1)/3C–SiC (0 0 1) interface, *Inverse Problems* 24 (2008) 035019.
- [96] X. Luo, G. Qian, E. Wang, C. Chen. Molecular-dynamics simulation of Al/SiC interface structures, *Physical Review B* 59 (1999) 10125-10131.
- [97] C.R. Dandekar, Y.C. Shin. Molecular dynamics based cohesive zone law for describing Al–SiC interface mechanics, *Composites Part A: Applied Science and Manufacturing* 42 (2011) 355-363.
- [98] P.M. Morse. Diatomic molecules according to the wave mechanics. II. Vibrational levels, *Physical Review* 34 (1929) 57-64.
- [99] J. Hoyt, M. Asta, A. Karma. Atomistic simulation methods for computing the kinetic coefficient in solid-liquid systems, *Interface Science* 10 (2002) 181-189.
- [100] J. Broughton, G. Gilmer, K. Jackson. Crystallization rates of a Lennard-Jones liquid, *Physical Review Letters* 49 (1982) 1496-1500.
- [101] E. Burke, J. Broughton, G. Gilmer. Crystallization of fcc (111) and (100) crystal - melt interfaces: A comparison by molecular dynamics for the Lennard - Jones system, *The Journal of chemical physics* 89 (1988) 1030-1041.
- [102] F. Celestini, J.-M. Debierre. Nonequilibrium molecular dynamics simulation of rapid directional solidification, *Physical Review B* 62 (2000) 14006-14011.
- [103] J. Hoyt, B. Sadigh, M. Asta, S. Foiles. Kinetic phase field parameters for the Cu–Ni system derived from atomistic computations, *Acta materialia* 47 (1999) 3181-3187.
- [104] M.S. Daw, M.I. Baskes. Semiempirical, quantum mechanical calculation of hydrogen embrittlement in metals, *Physical review letters* 50 (1983) 1285-1288.
- [105] M.S. Daw, S.M. Foiles, M.I. Baskes. The embedded-atom method: a review of theory and applications, *Materials Science Reports* 9 (1993) 251-310.
- [106] W. Briels, H. Tepper. Crystal growth of the Lennard-Jones (100) surface by means of equilibrium and nonequilibrium molecular dynamics, *Physical review letters* 79 (1997) 5074-5077.
- [107] C. Tymczak, J.R. Ray. Asymmetric crystallization and melting kinetics in sodium: a molecular-dynamics study, *Physical review letters* 64 (1990) 1278-2181.
- [108] L. Nastac. Numerical Modeling of Fluid Flow and Solidification Characteristics of Ultrasonically Processed A356 Alloys, *ISIJ International* 54 (2014) 1830-1835.
- [109] S. Spitans, A. Jakovics, E. Baake, B. Nacke. Numerical Modeling of Free Surface Dynamics of Melt in an Alternate Electromagnetic Field: Part I. Implementation and Verification of Model, *Metall and Materi Trans B* 44 (2013) 593-605.

- [110] M. Pal, S. Kholmatov, P. Jönsson. Numerical simulation of induction stirred ladle. Proceedings of COMSOL Conference, 2006.
- [111] F.U.s. Guide. Fluent 6.3: User's Guide Manual Fluent Inc. and Ansys's Fluent. 2006.
- [112] C. Pfeiler, B. Thomas, M. Wu, A. Ludwig, A. Kharicha. Solidification and particle entrapment during continuous casting of steel, *Steel Res. Int* 79 (2008) 599-607.
- [113] C. Wen, Y. Yu. Mechanics of fluidization. *Chem. Eng. Prog. Symp. Ser.*, vol. 62, 2014. p.100.
- [114] P. Saffman. The lift on a small sphere in a slow shear flow, *Journal of fluid mechanics* 22 (1965) 385-400.
- [115] B. Chalmers. Melting and freezing, *Trans. Aime* 200 (1954) 519.
- [116] Y. Mishin, D. Farkas, M.J. Mehl, D.A. Papaconstantopoulos. Interatomic potentials for monoatomic metals from experimental data and *ab initio* calculations, *Physical Review B* 59 (1999) 3393-3407.
- [117] J. Winey, A. Kubota, Y. Gupta. A thermodynamic approach to determine accurate potentials for molecular dynamics simulations: thermoelastic response of aluminum, *Modelling and Simulation in Materials Science and Engineering* 17 (2009) 055004.
- [118] H. Zhao, N. Chen, Y. Long. Interfacial potentials for Al/SiC(111), *Journal of Physics: Condensed Matter* 21 (2009) 225002.
- [119] X. Liu, S. Jia, L. Nastac. Ultrasonic cavitation-assisted molten metal processing of A356-Nanocomposites. *Proc. of the Advanced Casting Technologies Symposium, MS&T 2012, 2013.* p.7-11.
- [120] S. Jia, D. Zhang, L. Nastac. Experimental and numerical analysis of the 6061-based nanocomposites fabricated via ultrasonic processing, *Journal of Materials Engineering and Performance* 24 (2015) 2225-2233.
- [121] C.L. Kelchner, S. Plimpton, J. Hamilton. Dislocation nucleation and defect structure during surface indentation, *Physical Review B* 58 (1998) 11085-11088.
- [122] A. Stukowski. Structure identification methods for atomistic simulations of crystalline materials, *Modelling and Simulation in Materials Science and Engineering* 20 (2012) 045021.
- [123] J. Liu, H. Dong. Molecular dynamics calculation of thermodynamic properties of iron solidification. *IOP Conference Series: Materials Science and Engineering*, vol. 33: IOP Publishing, 2012. p.012113.
- [124] W. Zhou, Z. Xu. Casting of SiC reinforced metal matrix composites, *Journal of Materials Processing Technology* 63 (1997) 358-363.

[125] S. Jia. Experimental and theoretical analyses on the ultrasonic cavitation processing of Al-based alloys and nanocomposites. Doctoral dissertation: The University of Alabama TUSCALOOSA, 2015.

APPENDIX I – TERSOFF POTENTIAL VALUES FOR SiC

```

# Si and C mixture, parameterized for Tersoff potential
# this file is from Rutuparna.Narulkar @ okstate.edu
# values are from Phys Rev B, 39, 5566-5568 (1989)

# Tersoff parameters for various elements and mixtures
# multiple entries can be added to this file, LAMMPS reads the ones it needs
# these entries are in LAMMPS "metal" units:
# A,B = eV; lambda1,lambda2,lambda3 = 1/Angstroms; R,D = Angstroms
# other quantities are unitless

# format of a single entry (one or more lines):
# element 1, element 2, element 3,
# m, gamma, lambda3, c, d, costheta0, n,
# beta, lambda2, B, R, D, lambda1, A

C C C 3.0 1.0 0.0 38049 4.3484 -.57058 .72751
0.00000015724 2.2119 346.7 1.95 0.15 3.4879 1393.6

Si Si Si 3.0 1.0 0.0 100390 16.217 -.59825 .78734
0.0000011 1.73222 471.18 2.85 0.15 2.4799 1830.8

Si Si C 3.0 1.0 0.0 100390 16.217 -.59825 .78734
0.0000011 1.73222 471.18 2.36 0.15 2.4799 1830.8

Si C C 3.0 1.0 0.0 100390 16.217 -.59825 .787340
0.0000011 1.97205 395.126 2.36 0.15 2.9839 1597.3111

C Si Si 3.0 1.0 0.0 38049 4.3484 -.57058 .72751
0.00000015724 1.97205 395.126 2.36 0.15 2.9839 1597.3111

C Si C 3.0 1.0 0.0 38049 4.3484 -.57058 .72751
0.00000015724 2.2119 346.7 1.95 0.15 3.4879 1393.6

C C Si 3.0 1.0 0.0 38049 4.3484 -.57058 .72751
0.00000015724 2.2119 346.7 2.36 0.15 3.4879 1393.6

Si C Si 3.0 1.0 0.0 100390 16.217 -.59825 .78734
0.0000011 1.73222 471.18 2.85 0.15 2.4799 1830.8

```